PROPERTIES OF TWO-DIMENSIONAL MATERIALS GROWN ON METAL SUBSTRATES

A Dissertation
Presented to
The Academic Faculty

By

Chi-Ruei Pan

In Partial Fulfillment
of the Requirements for the Degree
Doctor of Philosophy in the
School of Physics

Georgia Institute of Technology

May 2019

PROPERTIES OF TWO-DIMENSIONAL MATERIALS GROWN ON METAL SUBSTRATES

Approved by:

Dr. Mei-Yin Chou, Advisor
School of Physics
Georgia Institute of Technology

Dr. Uzi Landman
School of Physics
Georgia Institute of Technology

Dr. Phillip N. First
School of Physics
Georgia Institute of Technology

Dr. Martin Mourigal
School of Physics
Georgia Institute of Technology

Dr. Seung Soon Jang
School of Materials Science and Engineering
Georgia Institute of Technology

Date Approved: March 21, 2019

In our description of nature the purpose is not to disclose the real essence of the phenomena but only to track down, as far as possible, relations between the manifold aspects of our experience.

—Niels Bohr

ACKNOWLEDGEMENTS

First, I would like to thank my advisor Dr. Mei-Yin Chou for sharing her professional knowledge, experience in career life, and guiding me toward the completion of this work. Throughout, I also appreciate her tolerance and patience for allowing me to try different possibilities. Her dedication to the scientific community also encourages me whenever I fall into a low ebb. Furthermore, I am grateful for the arrangements she made for me to cooperate with Dr. Chih-Kang Shih's group in the Department of Physics at UT Austin, which leads to a major highlight of my graduate research work. Along the way, I have received considerable help from many others. Dr. Keenan Zhou and Dr. Wen-Ying Ruan were the original members of the group at Georgia Tech who welcomed me when I first joined the group and introduced me to the historic school, the great campus, and even the big city, including every aspect of life. Besides, I thank the people from Academia Sinica when I first came here, including Dr. Chih-Piao Chuu, Dr. Tao He, Dr. Sheng-Fang Lin, Justin Hou, Po-Tung Fang, and Kuan-Hung Liu. They offered me the fundamental skills and knowledge of performing first-principles calculations, operating high-performing computers, implementing useful codes and conducting material research. I appreciate their guidance, encouragement and approachability in those early years of my graduate career. I also thank Jing Wang, who have joined our research group over the years for her help and friendship.

My collaborators contributed a great deal of input and critical ideas towards this work for which I am also very thankful. At UT Austin, I thank Dr. Qiang Chang for conducting the experiments on the growth of *h*-BN on transition metal substrates and carrying out a wealth of essential measurements. I also thank Woojoo Lee for the project about the quantum well states in bimetallic Pb/Ag thin films. I am also grateful to Dr. Ching-Ming Wei and Dr. Cheng-Rong Hsing for their fruitful discussion and instrumental suggestions about the set up of initial structures and the computational details. At Georgia Tech, I thank

Dr. Phillip First for sharing his expert and extensive knowledge in advanced condensed matter physics and inspiring ideas for further theoretical exploration.

This work heavily takes the advantage of computer simulations relying on high-performance computing. Most of the computational resources were provided by Academia Sinica and I am immensely indebted to Ching-Tao Lee for doing a wonderful job, which guarantees the smooth operation of those computing clusters as well as being prompt and patient to support me when I encounter any issues regarding to either software or hardware. Most importantly, I am grateful for the friendship over the years that I have been able to share with people from both Georgia Tech and Academia Sinica. At Georgia Tech, I thank Qiu Yu, Khai Nguyen, Raj Gohil, Yu-Hui Lin, Stephen Spitz, Matthew Conrad, Chien-Yuan Chang, Doppler Louis, Xiang Liu, Shi-Ron Chang, Meng-Hsin Tung, Patricia Yang, Jia-Li Liu and Yeu-Wei Harn. At Academia Sinica, I thank Dr. Cheng-Chau Chiu, Dr. Cangtao Yin, Dr. Han-Hsin Chiang, Dr. Yang-Hao Chan, Ho-Chun Lin, Chia-Wei Hsing, Hua-Ciao Lyu, Tzu-Chi Hsieh, Hao-Hsu, Benjamin K Chang, Kuan-Sen Lin, Hsiao-Han Chuang, Jheng-Wei Li, Jhih-Yu Syu, Wei-Shen Tee, Tzu-Chen Liu, and Li-Feng Yan. In particular, Annie Lin has been helping me a lot in organizing and dealing with various local administrative matters during my visits to Taiwan.

Finally, I thank my parents Chun-Ying Pan and Su-Chen Chang and my sister Peng-Chun Pan who have always encouraged me to become a doctor. Their spiritual support and understanding of my choices are always motivating me to move forward.

TABLE OF CONTENTS

LIST OF TABLES

LIST OF FIGURES

SUMMARY

Miniaturization and thinning of electronic devices necessitate the innovation of new technologies to discover alternative materials and designs. This effort depends critically on the advanced knowledge of materials and the development of theoretical models and computational power. In this work, we perform first-principles calculations based on density functional theory to evaluate the properties of three types of interfaces, including semiconductor–metal, insulator–metal and metal–metal. To be specific, we focus on an interesting reconstruction, the $\sqrt{3} \times \sqrt{3}$ phase, emerging on Si thin films grown on Ag(111), moiré patterns formed by a single-layer Hexagonal Boron Nitride (*h*-BN) and the transition metal substrates, Ru(0001) and Cu(111), as well as a stacked combination of Pb and Ag metallic thin films, which make them of interest in the areas of emergent two-dimensional materials.

Silicene is theoretically predicted to have similar electronic benefits to those of graphene. In addition, the stronger spin-orbit coupling of Si can induce a finite band gap, which may be detectable at room temperature, and the quantum spin Hall effect may be realized in this system. Moreover, compatibility with existing electronic technology may be advantageous. Still, challenges remain to enhance silicene stability and select appropriate substrates for the synthesis of silicene with regular symmetry. When Si is deposited on a Ag(111) substrate, while monolayer Si can produce a 3×3 phase, multilayer Si region and few-layer Si region can can have different reconstructions. We utilize honeycomb chain trimer (HCT) model to explain the multilayer region and show how interaction between top-layer Si and top-layer Ag can lead to a surface band with nearly linear dispersion. We also demonstrate that the emergence of the HCT reconstruction on the few-layer Si region can make the first layer of Si restores the regular buckling structure. With a coverage of 2.5 monolayer (ML), a nearly linear dispersion can also be observed in the few-layer Si thin film.

Heterostructures open new avenues for electrical tuning and the realization of quantum

size effects. *h*-BN on transition metals have recently been demonstrated to have large-scale moiré patterns by virtue of unique strong hybridization between N p_z states with the metal d_{z^2} states. Using first-principles calculations, we report a corrugated *h*-BN layer grown on the substrates. The wavy structure with some parts of the *h*-BN layer moving closer to the substrate enables us to explain the local work function modulation. Furthermore, we conduct calculations of projected density of states to figure out the orbital hybridization and the spatial modulation of the band profile observed by scanning tunneling spectroscopy.

Quantum confinement effects emerge when epitaxial growth can be precisely controlled. Because of the sensitivity of the quantum well states to film thickness, researchers can use this abrupt variation to monitor the growth of a thin film. Of fundamental scientific interest, the observation of quantum well states can be used to study the unique behavior of the quasi-two dimensional electron gas. We use first-principles calculation to investigate the band dispersions, the charge density distributions, and the constant-energy contours. Along with the band unfolding technique, we track down the essential quantum well states and compare their change from a pure metallic film to a bimetallic film.

CHAPTER 1
INTRODUCTION

Over the last half of the 20th century, the advancement in the manipulation of semiconducting materials has engendered rapid progress of electronic technology, improving people's lifestyle. For instance, both high-performance computing and high-speed communication are based on mass-produced semiconductors. With this rapid development, Moore's Law—the number of transistors in the integrated circuits doubles about every 2 years—has held for more than 50 years. However, transistor scaling has almost reached its physical limits, and thus, new relevant technologies are being researched. The related research fields include quantum computation, silicon photonics, and topological insulators—a recent discovery. Success in each of these highly advanced fields critically depends on the discovery or engineering of new materials with favorable combinations of properties to increase performance. One of the most popular materials is the family of two-dimensional (2D) materials. Usually, a single-layer crystalline material that is either one atom thick or a few atoms thick is called a 2D material. These 2D materials can demonstrate unique behaviors not observed in corresponding three-dimensional (3D) bulk materials. The most famous example is Dirac cones at the vertices of the graphene's Brillouin zone (BZ). In addition to graphene, 2D materials have increasingly been synthesized; some of these have already been applied in the industry. Moreover, with the improvement in experimental techniques, including scanning tunneling microscopy (STM) and scanning tunneling spectroscopy (STS), highly resolved measurements have become available; these techniques enable easy observation of the unique behaviors of 2D materials, facilitating the progress of nanoscience. In this work, we studied 2D materials grown on metallic substrates, with a focus on the electronic properties of interfaces formed by stacking different 2D materials. These interfaces include semiconductor–metal, insulator–metal, and metal–metal

heterostructures. In particular, for all three categories, we examined the thin Si films on Ag(111), modulated electronic properties of single-layer hexagonal boron nitride (denoted as *h*-BN) grown on Ru(0001) and Cu(111) substrates, and quantum well states (QWSs) in Pb–Ag thin films.

1.1 Si thin films on Ag(111)

Single-layer Si, called silicene, has become another rising star following graphene. Because they both have similar crystal structures and electronic configurations, silicene may possess many of the unique properties of graphene. Moreover, in contrast to a non-detectable band gap induced by the spin-orbit coupling of carbon (C), a stronger spin-orbit coupling of Si can induce a larger band gap, potentially detectable at room temperature. A $\sqrt{3} \times \sqrt{3}$ phase was recently noted in single-layer Si on a Ag(111) substrate through STM; thus, the existence of Dirac cones in this phase is highly debatable. Although some studies have reported linear dispersion from measurements of the quasiparticle interference pattern in real-space 2D mapping, others have demonstrated that the dispersion is in a parabola form. To resolve this issue, we first demonstrated that a single-layer Si can form a 3×3 superstructure on Ag(111) with an irregular buckling pattern due to Si–Ag interaction. The strong hybridization between Si p_z and Ag states leads to the removal of Dirac cones at the Fermi level. Herein, we then propose possible models for creating multilayer Si on Ag(111), containing adsorbed Ag atoms on top of the surface. The obtained STM images and energy dispersion for our models are in good agreement with experimental observations.

1.2 Single-layer *h*-BN on Ru(111) and Cu(111)

Lattice mismatch between the adsorbed 2D layer and the underlying substrate can cause large-scale periodic patterns, called moiré patterns. When two planar or surface materials with slightly different periodicities are stacked together, the minute differences can be grad-

ually accumulated and magnified. Although moiré patterns are a widely noted phenomenon during 2D heterostructure growth, the microscopic topography and the effect on electronic properties are not completely understood. Here, we discuss the moiré patterns formed by *h*-BN with transition metal substrates, Ru(0001) and Cu(111), by constructing supercell (SC) models that commensurate with both *h*-BN and the metal. Our relaxation calculations indicated that in the regions of "hole" in the moiré patterns, N atoms are situated approximately on top of underlying metal atoms. We also performed calculations on the projected density of states (PDOS), demonstrating strong hybridization between N p_z and metal d_{z^2} orbitals. The strong hybridization causes the hole regions to move closer to the substrate, thus inducing stronger charge transfer and lower local work function.

1.3 Pb/Ag bimetallic thin films

In contrast to materials with a band gap, metallic thin films can serve as a platform to study the QWS. With the availability of high-quality thin films, clear observation of QWSs was reported, followed by various unique properties, which are based on gradual variation in thicknesses; most of this variation can be explained by the thickness dependency of QWSs. Numerous theoretical approaches have been adopted to study QWSs in a metallic and metal–substrate thin films. However, studies may not have used the reasonable strain level in the heterostructure and thus the resulting QWS may not have been correct. Here, we again used our SC model, which enables a slight twist angle between Pb(111) and Ag(111) to compensate for the lattice mismatch. Next, we used the band unfolding technique to obtain the essential QWSs in the bimetallic system. We confirmed that the electronic coherence in the entire film is achievable by connecting QWSs in each metallic part with its own commensurate wavelength.

1.4 Thesis outline

Chapter 2 outlines the main theoretical and computational methods used in this work; these methods include the first-principles calculations within density functional theory (DFT) and formulations of the STM–theory, and the band unfolding technique. Next, Chapter 3 details our investigation of the electronic structures of Si on Ag(111). The surface reconstruction with the presence of adsorbed Si atoms on top and the transformation from 2D to 3D Si structures for few-layer Si grown on Ag(111) are reported. Moreover, our investigation of how tip-sample bias can change the calculated STM images is reported. In addition, we compare the binding energies for recently proposed models and further confirm the stability of our proposed models. Chapter 4 discusses details of our SC models for BN on metallic substrates. Next, the electronic structures of these heterostructures based on PDOS are analyzed. The hybridization between BN and metallic substrates as well as the modulation of the band structure are then clarified. We also calculate the electrostatic potential in the vacuum region, with which we can obtain the variation of the local work function. Finally, Chapter 5 reports our investigation of the bimetallic Pb–Ag thin film through band unfolding calculation, in which we compare the results with the unfolding path according to Pb and Ag lattices and the results for rotationally aligned with those for twisted Pb–Ag thin films. Moreover, the charge density distribution is demonstrated to confirm the electronic coherence within the entire bimetallic thin film.

CHAPTER 2

THEORETICAL AND COMPUTATIONAL BACKGROUNDS

2.1 Density functional theory

The Many-body Hamiltonian for the system containing electrons and nuclei is written as

$$H = -\sum_i \frac{1}{2}\nabla_i^2 - \sum_I \frac{1}{2M_I}\nabla_I^2 + \sum_i \sum_{j>i} \frac{1}{|\mathbf{r}_i - \mathbf{r}_j|} + \sum_I \sum_{J>I} \frac{Z_I Z_J}{|\mathbf{r}_I - \mathbf{r}_J|} + \sum_{i,I} \frac{Z_I}{|\mathbf{r}_i - \mathbf{R}_I|}\,, \tag{2.1}$$

in which the Hartree atomic units ($\hbar$=m_e=e=$\frac{1}{4\pi\epsilon_0}$=1) are used. Lower-case subscripts label electronic quantities while upper-case subscripts label nuclear quantities. Z and M denote the proton number and the mass of the nuclei, respectively. The first two terms describe the kinetic energies of electrons and nuclei. The last three terms are the classical electron–electron, nuclei–nuclei, and electron–nuclei Coulomb interactions.

Taking into account the fact that nuclei are much more massive than electrons, we can treat the nuclei motion to be static with respect to the electron motion and decouple their degrees of freedom. Therefore, the Born-Oppenheimer approximation writes a many-body wavefunction as a product of the nuclear and electronic wavefunctions. As a result, the second term in Equation 2.1 for the kinetic energy of nuclei is neglected and the fourth term for the nuclei–nuclei potential is constant. In addition, electrons are able to react almost instantaneously to any changes in arrangement of nuclei. Accordingly, it is also customary to treat the Coulomb interaction with the nuclei as part of the external potential. The normalized many-body wave function Ψ governed by the many-body Hamiltonian

satisfies the time-independent Schrödinger equation

$$H\Psi(\mathbf{r}_1, \mathbf{r}_2, ..., \mathbf{r}_N) = E\Psi(\mathbf{r}_1, \mathbf{r}_2, ..., \mathbf{r}_N). \tag{2.2}$$

As long as the wavefunction is known, all the ground-state properties are determined. Unfortunately, it is intractable to solve the 3N-coordinate problem arising in the many-body Schrödinger equation, where N is the total number of electrons in a system. Density functional theory (DFT) offers a way out of this predicament.

DFT proposed by Hohenberg and Kohn [1] and the Kohn-Sham implementation [2] have become one of the most powerful tools for the ground-state properties of electronic systems. It offers a reasonable computational cost and acceptable accuracy. The Hohenberg-Kohn theorem asserts that the ground-state electronic density of a system determines its ground-state properties. In this case, the total ground-state energy of a many-electron system is a functional of the electronic density, a function of one 3-coordinate position vector instead of 3N variables. Within the framework of Kohn-Sham density functional theory (KS-DFT) [2], the complicated interacting system is replaced by another system governed by non-interacting one-particle equations in which many-body effects are included in the exchange-correlation functional. However, the exact exchange-correlation functional is yet unknown and needs to be approximated. Based on the Thomas-Fermi-Dirac method [3, 4], the local spin density approximation (LSDA) leads to results comparable to the Hartree-Fock approximation. For non-uniform electron gas, the gradient of density is taken into account in the generalized gradient approximation (GGA) [5, 6, 7]. These semi-local exchange-correlation functionals remain popular for large systems because of the computational efficiency and the reasonable accuracy.

2.1.1 Hohenberg-Kohn theorem

Two remarkable statements related to the ground state of a system in an external potential were made by Hohenberg and Kohn in 1964 [1], which lay the foundations of modern DFT. To introduce the theorem, let us consider an N-electron system with the ground-state wavefunction $|\Psi_0\rangle$ and density $\rho_0(\mathbf{r})$ under the external potential $V_{\text{ext}}(\mathbf{r})$. The first theorem states that the external potential $V_{\text{ext}}(\mathbf{r})$ is uniquely determined by the corresponding ground-state electronic charge density $\rho_0(\mathbf{r})$, to within an additive constant. To prove this, assume that another different external potential $V'_{\text{ext}}(\mathbf{r})$ with ground-state $|\Psi'_0\rangle$ produces the same electronic charge density $\rho_0(\mathbf{r})$. The ground-state energies are then evaluated by $E_0 = \langle\Psi_0|\hat{H}|\Psi_0\rangle$ and $E'_0 = \langle\Psi'_0|\hat{H}'|\Psi'_0\rangle$ where $\hat{H} = \hat{F} + \hat{V}_{\text{ext}}$ and $\hat{H}' = \hat{F} + \hat{V}'_{\text{ext}}$ in which $\hat{F}$ is the operator composed of the first and third term of Equation 2.1. Now if we evaluate the expectation value of $\hat{H}$ with respect to $|\Psi'_0\rangle$, we find the inequality

$$\begin{aligned} E_0 = \langle\Psi_0|\hat{H}|\Psi_0\rangle < \langle\Psi'_0|\hat{H}|\Psi'_0\rangle &= \langle\Psi'_0|\hat{H}'|\Psi'_0\rangle + \langle\Psi'_0|\left(\hat{H} - \hat{H}'\right)|\Psi'_0\rangle \\ &= E'_0 + \int d\mathbf{r}\rho_0(\mathbf{r})\left[V_{\text{ext}}(\mathbf{r}) - V'_{\text{ext}}(\mathbf{r})\right], \end{aligned} \tag{2.3}$$

since V_{ext} and V'_{ext} are external potentials that do not depend on the ground-state wavefunction itself. In a similar way, evaluating the expectation value of $\hat{H}'$ with respect to $|\Psi_0\rangle$, we obtain another inequality

$$\begin{aligned} E'_0 = \langle\Psi'_0|\hat{H}'|\Psi'_0\rangle < \langle\Psi_0|\hat{H}'|\Psi_0\rangle &= \langle\Psi_0|\hat{H}|\Psi_0\rangle - \langle\Psi_0|\left(\hat{H} - \hat{H}'\right)|\Psi_0\rangle \\ &= E_0 - \int d\mathbf{r}\rho_0(\mathbf{r})\left[V_{\text{ext}}(\mathbf{r}) - V'_{\text{ext}}(\mathbf{r})\right]. \end{aligned} \tag{2.4}$$

Adding Equation 2.3 to Equation 2.4 gives rise to the obvious contradiction

$$E_0 + E'_0 < E'_0 + E_0\,. \tag{2.5}$$

Consequently, the original assumption that there exist two different external potentials that can generate the same ground-state electronic charge density is wrong. That is, one ground-state density corresponds to one external potential, which implies that a system's ground-state density uniquely determines the Hamiltonian describing the system. This also suggests that all the ground-state properties derived from the Hamiltonian are also the functionals of the ground-state density.

The first Hohenberg-Kohn theorem uniquely links the ground state densities to the external potentials in the many-electron system. From the first Hohenberg-Kohn theorem, again, $\rho(\mathbf{r})$ determines $V_{\text{ext}}(\mathbf{r})$ and thus determines $\hat{H}$ and Ψ. It is inferred that the expectation value of $\hat{F}$ is also a functional of $\rho(\mathbf{r})$.

$$F_{\text{HK}}[\rho(\mathbf{r})] = \langle \Psi | \hat{F} | \Psi \rangle \,. \tag{2.6}$$

However, it provides neither the analytic form of the universal functional nor the practical ways to obtain the ground state electron densities. The second Hohenberg-Kohn theorem concerns this issue. According to the variational principle, the expectation value of ground-state wavefunction, $|\Psi_0\rangle$, will always be lower than the expectation value calculated by using any other wavefunction $|\Psi\rangle$.

$$\langle \Psi_0 | \hat{F} | \Psi_0 \rangle + \langle \Psi_0 | V_{\text{ext}} | \Psi_0 \rangle < \langle \Psi | \hat{F} | \Psi \rangle + \langle \Psi | V_{\text{ext}} | \Psi \rangle \tag{2.7}$$

Equation 2.6 transforms the equation above into

$$F_{\text{HK}}[\rho_0(\mathbf{r})] + \int d\mathbf{r} \rho_0(\mathbf{r}) V_{\text{ext}} < F_{\text{HK}}[\rho(\mathbf{r})] + \int d\mathbf{r} \rho(\mathbf{r}) V_{\text{ext}}. \tag{2.8}$$

To go one more step further, v-representable densities are introduced that they arise from some external potential $v[\rho(\mathbf{r})]$. Based on this, a v-representable energy functional, $E_v[\rho(\mathbf{r})]$, can be defined in which the external potential, V_{ext}, corresponding to $\rho_0(\mathbf{r})$, is independent

of $\rho(\mathbf{r})$ and we will arrive the second Hohenberg-Kohn theorem:

$$E_v[\rho_0(\mathbf{r})] < E_v[\rho(\mathbf{r})]\,. \tag{2.9}$$

In summary, the ground state energy of the system can be obtained variationally with respect to $\rho(\mathbf{r})$. The density that minimizes the total energy is the exact ground-state density. Once we have the ground-state charge density, $\rho_0(\mathbf{r})$, we can simply substitute it into the energy functional to find the ground-state energy E_0.

2.1.2 The Kohn-Sham approach

One year after the Hohenberg-Kohn theorems were published, Kohn and Sham proposed [2] an approach that makes DFT feasible. The Kohn-Sham approach maps the original interacting many-body problem onto a non-interacting fictitious system such that its ground-state density is the same as that of the original one. Since the particles are non-interacting in the fictitious system, this leads to an one-particle equation, which is called the Kohn-Sham equation. To derive the Kohn-Sham equation, we perform the variation of the energy functional under the constrain that the total number of electrons is N. Introducing a Lagrange multiplier μ to the constraint, we write the variational problem for the Hohenberg-Kohn density-functional as

$$\delta\left[F[\rho] + \int \mathrm{d}\mathbf{r}\; V_{\text{ext}}(\mathbf{r})\rho(\mathbf{r}) - \mu\left(\int \mathrm{d}\mathbf{r}\;\rho(\mathbf{r}) - \mathbf{N}\right)\right] = 0\,. \tag{2.10}$$

Kohn and Sham divided $F[\rho]$ into three parts:

$$F[\rho] = T_{\mathrm{s}}[\rho] + \frac{1}{2}\int \mathrm{d}\mathbf{r}\mathrm{d}\mathbf{r}'\frac{\rho(\mathbf{r})\rho(\mathbf{r}')}{|\mathbf{r}-\mathbf{r}'|} + E_{\mathrm{xc}}[\rho]\,, \tag{2.11}$$

in which $T_{\mathrm{s}}[\rho]$ is the kinetic energy of the non-interacting system with density $\rho(\mathbf{r})$, the second term is the classical Coulomb energy, and $E_{\mathrm{xc}}[\rho]$ is the exchange-correlation energy

that also includes the difference between the kinetic energies of the interacting and non-interacting systems. The purpose of this separation is that the first two terms can be dealt with analytically, and the last term is a small fraction of the total energy that needs to be approximated. Substituting Equation 2.11 into Equation 2.10, one obtains

$$\frac{\delta T_{\mathrm{s}}[\rho(\mathbf{r})]}{\delta\rho(\mathbf{r})} + V_{\mathrm{KS}}(\mathbf{r}) = \mu\,, \tag{2.12}$$

in which the Kohn-Sham potential $V_{\mathrm{KS}}(\mathbf{r})$ is given by

$$V_{\mathrm{KS}}(\mathbf{r}) = \int \mathrm{d}\mathbf{r}' \frac{\rho(\mathbf{r}')}{|\mathbf{r}-\mathbf{r}'|} + V_{\mathrm{xc}}(\mathbf{r}) + V_{\mathrm{ext}}(\mathbf{r})\,. \tag{2.13}$$

The first term is conventionally called the Hartree energy and the exchange-correlation potential $V_{\mathrm{xc}}(\mathbf{r})$ is

$$V_{\mathrm{xc}}(\mathbf{r}) = \frac{\delta E_{\mathrm{xc}}[\rho(\mathbf{r})]}{\delta\rho(\mathbf{r})}\,. \tag{2.14}$$

2.2 Pseudopotentials

A pseudopotential is intended to replace the complicated interaction between the tightly-bound core electrons and the nucleus with an effective potential. In the all electron method, the valence electron wavefunctions need to oscillate in the core region in order to be orthogonal to the core electron wavefunctions. This requires a huge number of plane waves in the expansion, which seriously increase the computational cost. In the pseudopotential method, the valence electrons are described by pseudo-wavefunctions with significantly fewer nodes, which significantly reduces the number of plane waves. A good pseudopotential should be able to be generated from a simple atomic environment and be transferable to more complex systems such as molecules and solids. First-principles pseudopotentials are derived from atomic reference states, requiring that the pseudo- and all-electron valence

eigenstates have the same amplitude, and thus the density, outside a chosen cut-off radius, regarded as the core radius. Norm-conserving, ultrasoft, and projector-augmented-wave pseudopotentials are three important kinds of pseudopotentials which we will elaborate upon in this section.

2.2.1 Norm-conserving pseudopotential

The norm-conserving pseudopotential is a popular type of the pseudopotential originally developed by Hamann, Schlüter and Chiang [8], which takes the following form:

$$\hat{V}_{\mathrm{ps}}(r) = \sum_{\mathrm{l}} \sum_{\mathrm{m}} |Y_{\mathrm{lm}}\rangle V_{\mathrm{lm}}(r) \langle Y_{\mathrm{lm}}| \,. \tag{2.15}$$

Norm-conserving pseudopotentials have five fundamental characteristics listed as follows:

1. Pseudo-wavefunctions $|\Psi_{\mathrm{PS}}\rangle$ and all-electron wavefunctions $|\Psi_{\mathrm{AE}}\rangle$ agree beyond the core radius r_c.

2. The norm-conserving pseudopotential must equals to the atomic Coulomb potential for $r > r_c$.

3. The charge densities of the pseudo-valence and all-electron wavefunctions coincide when integrated within the range $0 < r < r_c$:

$$\int_0^{r_c} d\mathbf{r} |\psi_{\mathrm{PS}}(\mathbf{r})|^2 = \int_0^{r_c} d\mathbf{r} |\psi_{\mathrm{AE}}(\mathbf{r})|^2 \,. \tag{2.16}$$

4. Logarithmic derivatives of the pseudo-valence and all-electron wavefunctions agree at r_c since the wavefunction and its radial derivative are continuous at r_c. In other words, we consider the dimensionless quantity

$$r \frac{d}{dr} ln\psi = r \frac{\psi'}{\psi} \tag{2.17}$$

to be continuous across the boundary $r = r_c$ for both pseudo-valence and all-electron wavefunctions.

5. The first energy derivative of the logarithmic derivatives of the pseudo-valence and all-electron wavefunctions agree at r_c. It is this property that the norm-conserving pseudopotential is transferable between various simple and complex environments, as required for a good pseudopotential.

2.2.2 Ultrasoft pseudopotential

Ultrasoft pseudopotentials relax the norm-conserving constraint to reduce the necessary basis size further at the expense of introducing a generalized eigenvalue problem. This improves the smoothness (or "softness") of the pseudo-wavefunctions. The valence electron wavefunctions are also split into a smooth part $\tilde{\psi}$ and an auxiliary part which varies rapidly within the core region. The smooth parts are orthogonalized according to

$$\langle \tilde{\psi}_{\mathrm{i}} | S | \tilde{\psi}_{\mathrm{j}} \rangle = \delta_{\mathrm{ij}} \,, \tag{2.18}$$

where

$$S = 1 + \sum_{\mathrm{ij}} \Delta q_{\mathrm{ij}} |\beta_{\mathrm{i}}\rangle \langle \beta_{\mathrm{j}}| \,, \tag{2.19}$$

which is known as the overlap operator that only differs from unity inside the core region. In the equation above,

$$\beta_s = \sum_{s'} B^{-1}_{s,s'} \chi_{s'} \,, \tag{2.20}$$

where $B_{s,s'} = \langle \psi_s | \chi_{s'} \rangle$, and $\chi_s \equiv \left\{ \epsilon_s - \left[-\frac{1}{2}\nabla^2 + V_{\text{local}}(r) \right] \right\} \psi_s(\mathbf{r})$.

$$\Delta q_{\text{ij}} = \int_0^{r_c} d\mathbf{r} [\phi_{\text{i}}^*(\mathbf{r}) \phi_{\text{j}}(\mathbf{r}) - \tilde{\phi}_{\text{i}}^*(\mathbf{r}) \, , \tilde{\phi}_{\text{j}}(\mathbf{r})] \tag{2.21}$$

which represents the charge difference between the current choice of $\tilde{\psi}$ and the norm-conserving ψ, where $\phi = r\psi$.

2.2.3 Projector-augmented-waves pseudopotential

Another well-known pseudopotential is the projector augmented wave (PAW) pseudopotential [9, 10, 11]. As in the case of the ultrasoft pseudopotentials, PAW valence-electron wavefunctions are split into a smooth part and a localized part. The smooth part of the wavefunction, which we refer to as $|\tilde{\psi}\rangle$ is related to the full all-electron wavefunction by the transformation,

$$|\psi\rangle = T|\tilde{\psi}\rangle \, , \tag{2.22}$$

where T is known as the transformation operator. It is desired that T be unity only outside a sphere centered around a nucleus such that $|\psi\rangle$ and $|\tilde{\psi}\rangle$ agree outside the sphere. Therefore, we may write

$$T = 1 + \sum_{\text{i}} \tau_{\text{i}} \, , \tag{2.23}$$

where τ_{i}'s are non-zero only within the sphere around a nucleus. This region is known as the augmentation region, within which we may expand the smooth wavefunction as

$$|\tilde{\psi}\rangle = \sum_{\text{i}} c_{\text{i}} |\tilde{\psi}_{\text{i}}\rangle. \tag{2.24}$$

For a linear transformation operator T, the expansion coefficients, c_{i}'s, correspond to projections within the augmented spherical region

$$c_{\mathrm{i}} = \langle \tilde{p}_{\mathrm{i}} | \tilde{\psi} \rangle, \tag{2.25}$$

where $\tilde{p}_{\mathrm{i}}$'s are the required set of projection operators $\tilde{p}$ with the property

$$\langle \tilde{p}_{\mathrm{i}} | \tilde{\psi}_{\mathrm{j}} \rangle = \delta_{\mathrm{ij}}. \tag{2.26}$$

Since the full all-electron wavefunction may be written as

$$|\psi\rangle = |\tilde{\psi}\rangle + \sum_{\mathrm{i}} c_{\mathrm{i}} \left(|\psi_{\mathrm{i}}\rangle - |\tilde{\psi}_{\mathrm{i}}\rangle \right), \tag{2.27}$$

we see that

$$T = 1 + \sum_{\mathrm{i}} \left(|\psi_{\mathrm{i}}\rangle - |\tilde{\psi}_{\mathrm{i}}\rangle \right) \langle \tilde{p}_{\mathrm{i}}|. \tag{2.28}$$

2.3 Exchange-correlation functionals

2.3.1 Local density approximation

The local density approximation (LDA) ignores the dependence of V_{xc} on the nonlocal density. The spin-unpolarized version of LDA functional is written as

$$E_{\mathrm{xc}}^{\mathrm{LDA}} = \int \rho(\mathbf{r}) \epsilon_{\mathrm{xc}}(\rho) d\mathbf{r}\,, \tag{2.29}$$

where $\rho(\mathbf{r})$ is the local electronic charge density and ϵ_{xc} is the exchange-correlation energy per particle of a homogeneous system of density ρ. The exchange term takes a simple analytic form for the homogeneous electron gas (HEG), while no general expressions for the exact correlation term are known. The exchange energy at zero polarization is straightfor-

ward to calculate and the result is

$$\epsilon_x(\rho) = -\frac{3}{4}\left(\frac{3\rho}{\pi}\right)^{\frac{1}{3}} . \tag{2.30}$$

A popular approximation for the correlation energy ϵ_c is based on Monte Carlo calculations by Ceperley and Alder [12]. Other well-known approximations have been developed by Perdew and Zunger (PZ) [13] as well as Vosko, Wilkes and Nusiar (VWN) [14].

2.3.2 Generalized gradient approximation

A second widely-used approximation for $E_{\rm xc}[\rho]$ is the generalized gradient approximation (GGA) [5, 6, 7]. The modern GGA functional form for the exchange-correlation energy is given as

$$E_{\rm xc}^{\rm GGA} = \int f(\rho_\uparrow, \rho_\downarrow, \nabla\rho_\uparrow, \nabla\rho_\downarrow) d\mathbf{r} \,, \tag{2.31}$$

which attempts to account for non-homogeneity in a real system by including information about the charge density gradient. f is a universal function of the spin-up and spin-down densities and their gradients. There exist several versions of GGA, all of which are parametrized somewhat differently. The Perdew-Burke-Ernzerhof (PBE) [15] GGA is one of those constructed to satisfy the constraints and limits, including the normalization condition, $\int d\mathbf{r}' \rho_{\rm xc}(\mathbf{r}, \mathbf{r}') = -1$, and the scaling condition, $n_\gamma(\mathbf{r}) = \gamma^3 n(\gamma\mathbf{r})$. There are other GGAs not constructed this way, but obtained by brute-force fitting to a large data set. The great strength of the GGA lies in the dramatic improvement it gives over the LDA in calculating such properties as bond dissociation energies which the LDA may overestimate by as much as 100%. The GGA also gives a great improvement over the LDA for bulk moduli of solids. With modern GGA exchange-correlation potentials, atomic and molecular quantities can now be calculated with chemical accuracy.

2.4 Theory of scanning tunneling microscopy

Scanning tunneling microscopy (STM) is invented by Gerd Binning and Heinrich Roher in 1981 [16, 17]. This instrument consists of a sharp metallic tip which is positioned at a small distance, usually a few angstroms, away from the substrate surface. In this case, the wavefunction of the tip and the substrate can overlap. Therefore, a tunneling current occurs between this small spatial gap. By detecting the current in the complete circuit, one can observe the local electronic properties on the surface and thus infer the atomic configurations. After the birth of STM, it developed quickly and allowed researchers to see the nanostructures with high resolution, which paves the way for the funtionalization of nanostructures for diverse applications.

To interpret the observed STM images, one has to figure out the theoretical models of the transport mechanisms. There are various theories of STM, which, generally speaking, are divided into two categories: perturbative methods and non-perturbative methods. Here we will focus on the former containing the Bardeen's approach [18] and the Tersoff-Hamann approximation [19, 20].

2.4.1 The Bardeen's approach

The Bardeen's approach, also known as the transfer Hamiltonian method, was proposed in 1961 first to explain the tunneling behavior in the thin oxide barrier sandwiched between superconducting electrodes and was later extended by Tersoff and Hamann, which will be discussed in the next subsection. The approach is based on the following assumptions:

1. The electron tunneling is treated as a one-electron process.

2. The interaction of the tip with the substrate is ignored.

3. Elastic tunneling is assumed.

Consider the tunneling process as a transport problem that the tunneling current flows

between the two electrodes, substrate and tip, and is denoted as S and T. In the beginning, two electrodes are far away from each other. The total system can be separated into distinct sub-systems with known Hamiltonians. Therefore, the unperturbed wavefunction satisfies the Schödinger equation of the isolated electrode,

$$i\hbar\frac{\partial\Psi^j(z,t)}{\partial t} = \left(-\frac{\hbar^2}{2m}\frac{\partial^2}{\partial z^2} + U_j(z)\right)\Psi^j(z,t)\,, \tag{2.32}$$

where U_j is the potential of the electrode $j(= S \text{ or } T)$. Once the distance between the two electrodes is reduced, the unperturbed wavefunctions of two electrodes will overlap and be affected by the total potential, $U_S(z) + U_T(z)$. The wavefunction of the tip–sample system is governed by the Schödinger equation containing the total potential.

$$i\hbar\frac{\partial\Psi(z,t)}{\partial t} = \left(-\frac{\hbar^2}{2m}\frac{\partial^2}{\partial z^2} + U_S(z) + U_T(z)\right)\Psi(z,t)\,. \tag{2.33}$$

Here the index j has been removed since the first assumption of Bardeen's approach has been used. Next, U_T is treated as a perturbation which is turned on adiabatically, which, mathematically, can be described via a time-dependent potential:

$$U_T(t) = \exp(\eta t/\hbar)U_T, \text{ and } \eta > 0\,. \tag{2.34}$$

By using the Fermi's Golden Rule, one obtains the probability per unit time that describes an electron in the state ψ_μ^S at time $t = -\infty$ jumping to a state ψ_ν^T as

$$P_{\mu\nu} = \frac{2\pi}{\hbar}\delta(E_\mu^S - E_\nu^T)|M_{\mu\nu}|^2\,, \tag{2.35}$$

where $M_{\mu\nu} \equiv \left\langle\psi_\nu^T\right| U_T \left|\psi_\mu^S\right\rangle$. If we consider the multiple states in the tip and substrate, the Fermi-Dirac distribution will be taken into account. One can write the tunneling current

from the substrate to the tip and the tip to the substrate as

$$I_{S\to T} = \frac{4\pi e}{\hbar}\sum_{\mu\nu} f\left(E_\mu^S\right)\left[1-f\left(E_\nu^T\right)\right]|M_{\mu\nu}|^2\,\delta\left(E_\nu^T - E_\mu^S - eV\right) \text{ and} \tag{2.36}$$
$$I_{T\to S} = \frac{4\pi e}{\hbar}\sum_{\mu\nu} f\left(E_\nu^T\right)\left[1-f\left(E_\mu^S\right)\right]|M_{\mu\nu}|^2\,\delta\left(E_\nu^T - E_\mu^S - eV\right)\ ,$$

where V is the tip–sample bias and a factor of 2 takes into account of the spin. The net current, $I = I_{S\to T} - I_{T\to S}$, is then

$$I = \frac{4\pi e}{\hbar}\sum_{\mu\nu}\left[f\left(E_\mu^S\right) - f\left(E_\nu^T\right)\right]|M_{\mu\nu}|^2\,\delta(E_\nu^T - E_\mu^S - eV)\,. \tag{2.37}$$

Substitute $\sum_\mu$ by $\int \rho^S(E)dE$ and $\sum_\nu$ by $\int \rho^T(E)dE$ with a change of variables, the formula of the net current is

$$I = \frac{4\pi e}{\hbar}\int_{-\infty}^{\infty} d\epsilon\left[f\left(E_F - eV + \epsilon\right) - f\left(E_F + \epsilon\right)\right]\rho^S\left(E_F - eV + \epsilon\right)\rho^T\left(E_F + \epsilon\right)|M|^2\ . \tag{2.38}$$

At low temperature, the Fermi distribution is nearly a step function and the current can be simplified to

$$I = \frac{4\pi e}{\hbar}\int_0^{eV} d\epsilon\rho^S\left(E_F - eV + \epsilon\right)\rho^T\left(E_F + \epsilon\right)|M|^2\ . \tag{2.39}$$

Assuming that the tip-sample bias is small enough, the differential conductance, which is related to the scanning tunneling spectroscopy(STS), is expressed as

$$\frac{dI}{dV} = \frac{4\pi e^2}{\hbar}\rho^S\left(E_F - eV\right)\rho^T\left(E_F\right)|M|^2 \propto \rho^S\left(E_F - eV\right)\ . \tag{2.40}$$

2.4.2 The Bardeen's tunneling matrix element

Based on the following two assumptions that the sample potential U_S is zero in the tip region and the electron scattering is elastic, $E_\nu^T = E_\mu^S + eV$, the matrix element $M_{\mu\nu}$ can be derived by using Eq. 2.32. The calculation of the matrix element is shown below.

$$\begin{aligned}
M_{\mu\nu} &= \left\langle \psi_\nu^T \right| U_T \left| \psi_\mu^S \right\rangle = \int d^3r \psi_\nu^{T*} U_T \psi_\mu^S \\
&= \int d^3r \psi_\mu^S \left(E_\nu^T + \frac{\hbar^2}{2m}\frac{\partial^2}{\partial z^2} \right) \psi_\nu^{T*} = \int d^3r \left(\psi_\nu^{T*} E_\mu^S \psi_\mu^S + \psi_\mu^S \frac{\hbar^2}{2m}\frac{\partial^2}{\partial z^2}\psi_\nu^{T*} \right) \\
&= -\frac{\hbar^2}{2m} \int d^3r \left(\psi_\nu^{T*}\frac{\partial^2\psi_\mu^S}{\partial z^2} - \psi_\mu^S \frac{\partial^2 \psi_\nu^{T*}}{\partial z^2} \right) = -\frac{\hbar^2}{2m} \int d^3r \frac{\partial}{\partial z} \left[\psi_\nu^{T*}\frac{\partial\psi_\mu^S}{\partial z} - \psi_\mu^S \frac{\partial \psi_\nu^{T*}}{\partial z} \right] \\
&= -\frac{\hbar^2}{2m} \int dxdy \left[\psi_\nu^{T*}\frac{\partial\psi_\mu^S}{\partial z} - \psi_\mu^S \frac{\partial \psi_\nu^{T*}}{\partial z} \right],
\end{aligned}$$

where the last integration is done on the separation from the surface.

2.4.3 The Tersoff-Hamann model

In the previous section, we have shown the connection of the tip states with the image mechanism of the STM through ρ^T. However, those states usually remain unknown in the realistic experiment. The Tersoff-Hamann model is aimed to solve this problem by dealing with the tip states separately, which simulated the tip as a geometrical point. Consequently, the STM image is related to the properties of the surface alone.

In the vacuum region, there is no contribution of the potential from both the substrate and the tip, so the wavefunction here satisfy the following equation:

$$\nabla^2 \psi = \kappa^2 \psi \,, \tag{2.41}$$

where $\kappa = \frac{\sqrt{2m\Phi}}{\hbar}$ and Φ is the work function. The Green's function for the Schrödinger

equation satisfies the following equation,

$$\left[\nabla^2 - \kappa^2\right] G(\mathbf{r} - \mathbf{r_0}) = -\delta(\mathbf{r} - \mathbf{r_0})\,. \tag{2.42}$$

Assuming that the tip is just a single atom which has predominantly s-orbital states, the tip wavefunction can be written as

$$\psi^T(\mathbf{r}) = \frac{4\pi C}{\kappa} G(\mathbf{r} - \mathbf{r_0})\,. \tag{2.43}$$

Insert the tip wavefunction into the expression of $M_{\mu\nu}$.

$$\begin{aligned} M_{\mu\nu} &= \frac{2\pi C\hbar^2}{\kappa m} \int d\mathbf{S} \left[G(\mathbf{r} - \mathbf{r_0})\nabla\psi_\mu^S - \psi_\mu^S \nabla G(\mathbf{r} - \mathbf{r_0})\right] \\ &= \frac{2\pi C\hbar^2}{\kappa m} \int d^3r \left[G(\mathbf{r} - \mathbf{r_0})\nabla^2\psi_\mu^S - \psi_\mu^S \nabla^2 G(\mathbf{r} - \mathbf{r_0})\right] \\ &= \frac{2\pi C\hbar^2}{\kappa m} \int d^3r \{G(\mathbf{r} - \mathbf{r_0})\kappa^2\psi_\mu^S - \psi_\mu^S \left[\kappa^2 G(\mathbf{r} - \mathbf{r_0}) - \delta(\mathbf{r} - \mathbf{r_0})\right]\} \\ &= \frac{2\pi C\hbar^2}{\kappa m} \int d^3r \psi_\mu^S(\mathbf{r_0})\delta(\mathbf{r} - \mathbf{r_0}) \\ &= \frac{2\pi C\hbar^2}{\kappa m} \psi_\mu^S(\mathbf{r_0})\,. \end{aligned} \tag{2.44}$$

Therefore, one obtain the expression of the matrix element that can be substituted into Equation 2.39 such that the local density of the sample at the position r_0 can be calculated.

2.5 The technique of band unfolding

The Bravais lattice has translational symmetry, for which one can define a translational vector $\mathbf{T} = n_1\mathbf{a_1} + n_2\mathbf{a_2} + n_3\mathbf{a_3}$, where $\mathbf{a_1}$, $\mathbf{a_2}$, $\mathbf{a_3}$ are lattice vectors in real space, and n_1, n_2, n_3 are integers such that all properties remain unchanged under translations by any vector $\mathbf{T}$. The most important translational invariant properties would be the Hamiltonian. Considering the Hamiltonian as a function of position vector $H(\mathbf{r})$, it must obey $H(\mathbf{r}) = H(\mathbf{r} + \mathbf{T})$ in the Bravais lattice. According to the Bloch's theorem: the eigenfunc-

tions of a translational invariant Hamiltonian can be written as $\psi(\mathbf{r}) = \exp(\mathrm{i}\mathbf{k}\mathbf{r})u(\mathbf{r})$, where $u(\mathbf{r})$ is a periodic function with the same periodicity as that of the crystal, $u(\mathbf{r}) = u(\mathbf{r}+\mathbf{T})$, and $\mathbf{k}$ is the crystal momentum defined in the first Brillouin zone. Bloch's theorem lays the foundation of the concept of electronic band structures. It is useful to write the Bloch wavefunction with subscripts as $\psi_{n\mathbf{k}}$, where n is the discrete band index that denotes the different eigenstates with the same $\mathbf{k}$. The electronic band structures can theoretically predict various crystal properties, and also be directly compared to the angle resolved photoemission spectroscopy (ARPES).

However, in the cases when the original translational symmetry is broken, such as doped materials, defected crystals or surface reconstruction, we are forced to use supercells (SC) that are built from multiple stacking primitive cells (PC). The size of the reciprocal-space Brillouin zone are inverse to that of its corresponding real-space unit cell, which makes it even more difficult to extract information from the band structure since the bands are folded into a relatively small szone and become flat and crowded if we plot them along the high symmetry paths. In order to compare with ARPES results, one has to unfold the supercell band structure back into the corresponding primitive-cell one.

Theoretically, the folding of the bands introduces additional couplings, $V_{kj,k'j'}$, between the originally uncoupled Kohn-Sham orbitals $|kj\rangle$ and $|k'j'\rangle$ in the primitive Brillouine zone (PBZ), where k and j label the crystal momentum and band index, respectively. This coupling forces us to label those states with a supercell crystal momentum $\mathbf{K}$ as the new quantum number in the supercell Brillouin zone(SBZ).[In the following, upper-(lower-)case symbols are for the super (primitive) cell.]

In contrast to folding, the purpose of unfolding is to associate each of the eigenstates in SBZ to a particular primitive eigenvectors $\mathbf{k_0}$. To determine how close SC Bloch waves are to PC ones, we can calculate an overlap matrix element between the supercell eigenvector, $|\mathbf{K}m\rangle$, and the eigenvectors of each possible unfolded wavevector, $|\mathbf{k}_0 n\rangle$, where m and n are the indices of their respective eigenvector. Furthermore, Popescu *et al.* [21] has shown

that the overlap matrix element is independent of the eigenvectors of the PBZ that one usually does not have access to.

The following shows a derivation of the spectral weight in a plane-wave basis:

$$\begin{aligned} P_{\mathbf{K}m}(\mathbf{k}_0) &= \sum_n | < \mathbf{K}m|\mathbf{k}_0 n > |^2 \\ &= \sum_n < \mathbf{K}m|\mathbf{k}_0 n >< \mathbf{k}_0 n|\mathbf{K}m > \ . \end{aligned} \tag{2.45}$$

This quantity measures the amount of a fixed Bloch character $\mathbf{k_0}$ preserved in the SC eigenstate, $|\mathbf{K}m\rangle$. The periodic part of the PC state and the SC state can be expanded in the Fourier series, and the states can be written as

$$\begin{aligned} |\mathbf{K}m\rangle &= \left[\sum_{\mathbf{G}} C_{\mathbf{K}m}(\mathbf{G}) \exp(i\mathbf{K}\cdot\mathbf{r})\right] \text{ and} \\ |\mathbf{k_0}n\rangle &= \left[\sum_{\mathbf{g}} B_{\mathbf{k_0}n}(\mathbf{g}) \exp(i\mathbf{g}\cdot\mathbf{r})\right] . \end{aligned} \tag{2.46}$$

Now we use the condition that $|\mathbf{k_0}n\rangle$ form a complete orthonormal set:

$$\begin{aligned} \delta_{nn'} &= \langle \mathbf{k_0}n|\mathbf{k_0}n'\rangle \\ &= \sum_{\mathbf{g},\mathbf{g}'} B^*_{\mathbf{k_0}n}(\mathbf{g}) B_{\mathbf{k_0}n'}(\mathbf{g}') \int d^3r \exp(i(\mathbf{g}-\mathbf{g}')\cdot\mathbf{r}) \\ &= \sum_{\mathbf{g}} B^*_{\mathbf{k_0}n}(\mathbf{g}) B_{\mathbf{k_0}n'}(\mathbf{g}) \, . \end{aligned} \tag{2.47}$$

From the formula above, one can easily obtain another equivalent condition:

$$\delta_{gg'} = \sum_n B^*_{\mathbf{k_0}n}(\mathbf{g}) B_{\mathbf{k_0}n}(\mathbf{g}') \, . \tag{2.48}$$

We can use Equation 2.46 to get

$$\langle \mathbf{k_0}n|\mathbf{K}m\rangle = \sum_g \sum_G B^*_{\mathbf{k_0}n}(\mathbf{g}) C_{\mathbf{K}m}(\mathbf{G}) \int d^3r \exp(i(\mathbf{G}+\mathbf{K}-\mathbf{g}-\mathbf{k_0})\cdot\mathbf{r})) \tag{2.49}$$

$$= \sum_g B^*_{\mathbf{k_0}n}(\mathbf{g}) C_{\mathbf{K}m}(\mathbf{g}+\mathbf{k_0}-\mathbf{K})\,, \text{ and}$$

$$\langle \mathbf{K}m|\mathbf{k_0}n\rangle = \sum_g B_{\mathbf{k_0}n}(\mathbf{g}) C^*_{\mathbf{K}m}(\mathbf{g}+\mathbf{k_0}-\mathbf{K})\,.$$

Multiplying the two quantities above and applying the condition of Equation 2.48, one obtains

$$P_{\mathbf{K}m}(\mathbf{k_0}) = \sum_{\mathbf{g},\mathbf{g}'} C_{\mathbf{K}m}(\mathbf{g}+\mathbf{k_0}-\mathbf{K}) C^*_{\mathbf{K}m}(\mathbf{g}'+\mathbf{k_0}-\mathbf{K})\delta_{\mathbf{g},\mathbf{g}'} \tag{2.50}$$

$$= \sum_{\mathbf{g}} |C_{\mathbf{K}m}(\mathbf{g}+\mathbf{k_0}-\mathbf{K})|^2\,,$$

which only depends on the expansion coefficients from SC calculations. This simply indicates that to do the unfolding, look for coefficients with wave vectors satisfying $\mathbf{K}+\mathbf{G} = \mathbf{k}+\mathbf{g}$, that is, $\mathbf{G} = \mathbf{k}+\mathbf{g}-\mathbf{K}$. Finally, the spectral function (unfolded band structure) is

$$A(\mathbf{k};\epsilon) \equiv \sum_m P_{m\mathbf{K}}\delta(\epsilon - \epsilon_m(\mathbf{K}))\,. \tag{2.51}$$

CHAPTER 3

SILICON THIN FILMS ON SILVER (111)

The use of 2D materials has been popular since the successful fabrication of single-layer graphite, namely graphene, in 2004 [27]. These 2D materials show extraordinary behaviors, not observed in the corresponding 3D bulk materials. The observation of Dirac cones at the vertices of graphene's BZ is the most famous example. Since recognizing the unique properties of graphene, numerous studies have focused on searching for new 2D materials other than graphene. Several 2D materials have been successfully synthesized; some of them already have industrial applications. This chapter reports our investigation of a novel 2D material composed of Si, which is categorized under the same group as C in the periodic table. Si forms silicene, which has a honeycomb lattice similar to that of graphene, but demonstrates small buckling. First-principles calculations have indicated that freestanding silicene is thermally stable in the form of a low-buckled honeycomb lattice with mixed sp^3–sp^2 bonding [28, 29, 30]. Because of its symmetry, the energy dispersion of freestanding silicene exhibits a linear feature near the Fermi level at the vertices of the hexagonal BZ. In addition, Si has a larger spin-orbit coupling than C; thus, silicene is a potential candidate for detecting the quantum spin Hall effect [31, 32]. Because no 2D structure of Si has ever been found in nature and its compatibility with existing electronic technology may be advantageous, the aforementioned prediction has stimulated tremendous interest in growing Si in the laboratory. Some studies have reported the evidence of epitaxial silicene sheet formation on the Ag substrate [33, 34, 35], whereas others have reported its successful growth on $ZrB_2(0001)$ [36] and Ir(111) [37].

Unlike graphite, Si does not have a planar structure, with a weak layer–layer interaction. Thus, mechanical exfoliation cannot be used to produce single-layer Si. Epitaxial growth of silicene on a substrate is a possible solution. Many research groups have at-

tempted to grow a 2D Si layer on Ag(111) in the last few years. Through carefully tuning of the substrate temperatures and deposition rates, researchers can observe various phases of 2D Si layers on Ag(111) [38, 39, 40]. Under a certain temperature window (460–470 K) and a Si coverage lower than one monolayer (ML) [33], an unique flower-like pattern can be observed through STM, which can be described by a 3×3 Si SC lattice matched with a 4×4 SC of Ag(111). This 3×3 phase has been thoroughly examined, and its atomic structure has been identified as a honeycomb silicene lattice with a distinct buckling pattern (Figure 3.1(a)). This distorting structure caused by its significant interaction with the Ag substrate can break the regular buckling symmetry of freestanding silicene along with the preferred linear dispersion of 2D massless Dirac electrons, which is illustrated in the projected band structure on Si p_z orbitals (Figure 3.2). Note that the $\bar{K}$ point of a 1×1 unit cell of silicene is folded to $\bar{\Gamma}$ point of a 3×3 SC of silicene (again, commensurate to 4×4 Ag(111)). No linear dispersion is found at the $\bar{\Gamma}$ point around the Fermi level. The only dispersion close to a crossing lies at approximately -0.6 eV at the $\bar{\Gamma}$ point, but the interaction with the Ag states causes a small splitting for these states. This evidence can explain the absence of the Landau-level sequences in STS [41]. Mahatha *et al.* further used angle-resolved photoemission spectroscopy (ARPES) to prove that no Dirac cones were observed [42].

Numerous studies have reported another $\sqrt{3} \times \sqrt{3}$ phase in experiments with higher growth temperatures. As the temperature of the Ag substrate increases (>500 K) or the Si coverage exceeds one ML, a $\sqrt{3} \times \sqrt{3}$ reconstruction appears on the terrace of the multilayer region [43, 44, 45], whereas the 3×3 phase remains in the single-layer region. These observations imply that the $\sqrt{3} \times \sqrt{3}$ phase directly forms on top of the 3×3 phase. However, reports on the structures and properties of this phase are not in agreement. Although some studies claim that the $\sqrt{3} \times \sqrt{3}$ phase is induced by an irregular protrusion of Si in silicene [46, 47], others assert that this phase comprises bilayer Si [40, 44]. Regarding the electronic properties, Chen *et al.* [48] presented linear dispersion from measurements

of the quasiparticle interference pattern through real-space 2D mapping, whereas Arafune *et al.* [49] demonstrated that this dispersion is parabolic and becomes more linear on moving away from the Fermi level. Moreover, the STM topologies of Ag on Si(111) and Si on Ag(111) show similar $\sqrt{3} \times \sqrt{3}$ symmetries [50].

This chapter reports the first-principles studies on the atomic configurations and the electronic properties of the $\sqrt{3} \times \sqrt{3}$ phase. Moreover, we propose few-layer Si models to explain the Si growth on Ag(111), illustrating the transformation from a 2D 3×3 Si layer to a 3D Si thin film covered with the $\sqrt{3} \times \sqrt{3}$ phase. Because the strong covalent bonds formed between Si layers, we believe that none of the reported Si structures on Ag(111) exhibit the desired feature of 2D massless Dirac electrons.

3.1 Multilayer Si model

The $\sqrt{3} \times \sqrt{3}$ phase forms in the multilayer region, and the heights from layer to layer are integer multiples of approximately 0.31 nm [43], which corresponds to the thickness of one double-layer of the Si bulk in [111] direction. Thus, the multilayer region is probably the Si bulk covered with a $\sqrt{3} \times \sqrt{3}$ reconstruction. Notably, this structure is similar to that of the Si(111)–$\sqrt{3} \times \sqrt{3}$–Ag surface, conventionally referred to as the honeycomb chain trimer (HCT) model [51]. The structure presents as shown in Figure 3.3. A surface cut on Si(111) results in an unstable "missing layer" that leaves three dangling bonds for each Si. With adsorbed Ag atoms, three Si atoms move closer to each other; this saturates two of the dangling bonds. Each Si also binds with one of the nearest Ag. The reconstructed atomic structure (Figure 3.3(a)) demonstrates that the third-layer Si atoms are split into two sublayers with a tiny height difference. For this split third layer, the higher Si is located in the middle of three nearest neighboring Ag atoms laterally, while the lower Si is in the center of the triangle formed by three nearest neighboring top-layer Si atoms. Besides, Figure 3.3(b) shows that the Ag atoms are laterally slightly deviated from the fifth-layer Si atoms and are shifted toward one closest top-layer Si atom, which can saturate the remain-

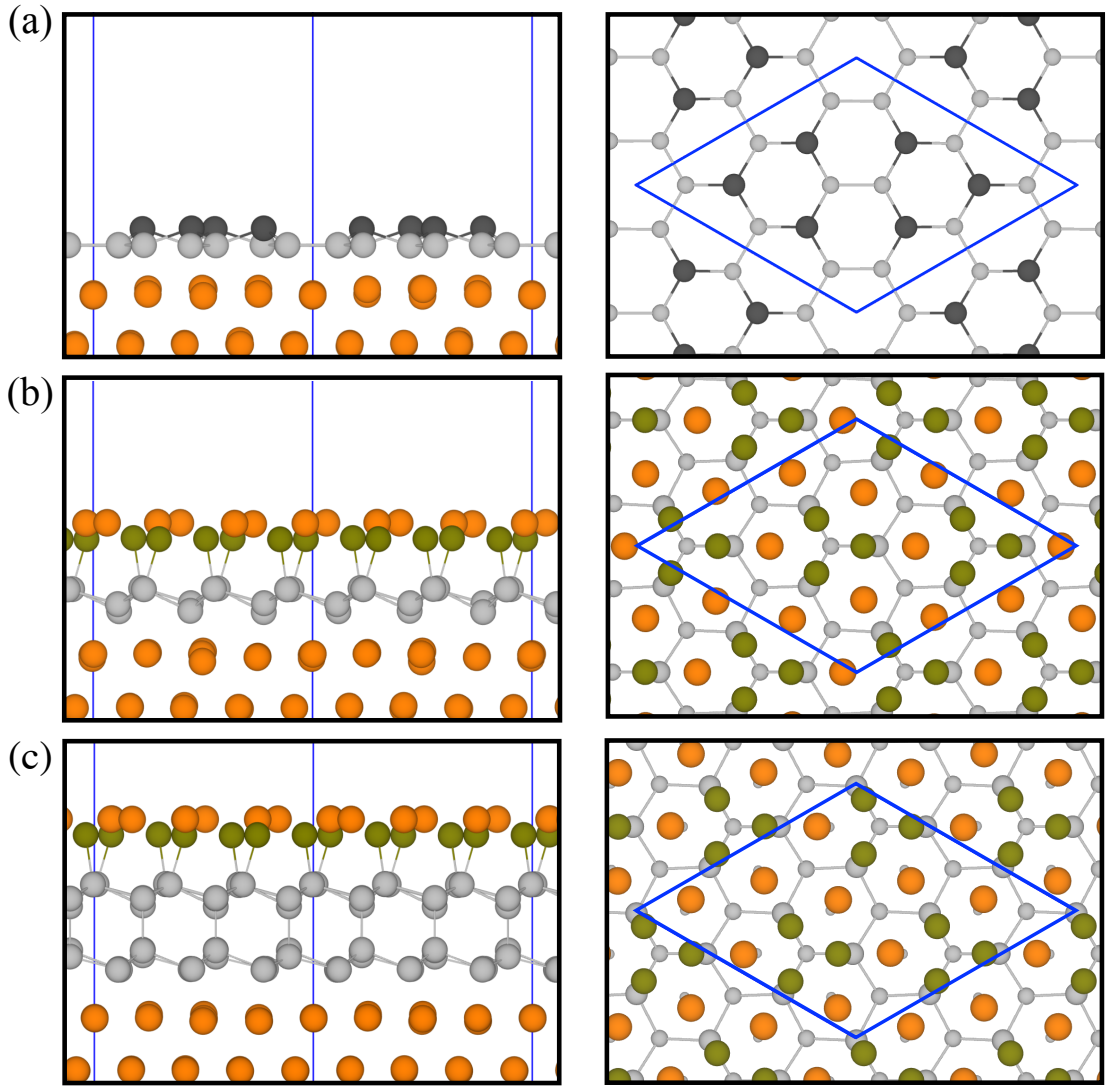

Figure 3.1: Side view (left) and top view (right) of the relaxed atomic structure of (a) 1 ML of Si on Ag(111), also known as the 3×3 phase, (b) the 1.5 ML of Si on Ag(111) model, and (c) the 2.5 ML of Si on Ag(111) model, in which the orange, dark green, and gray spheres correspond to Ag, top-layer Si, and lower-layer Si atoms, respectively. The blue rhombuses show 3×3 unit cells used in the calculation. In (a), the dark gray spheres denote upward buckled Si atoms. For all the top views, the Ag substrates are not shown.

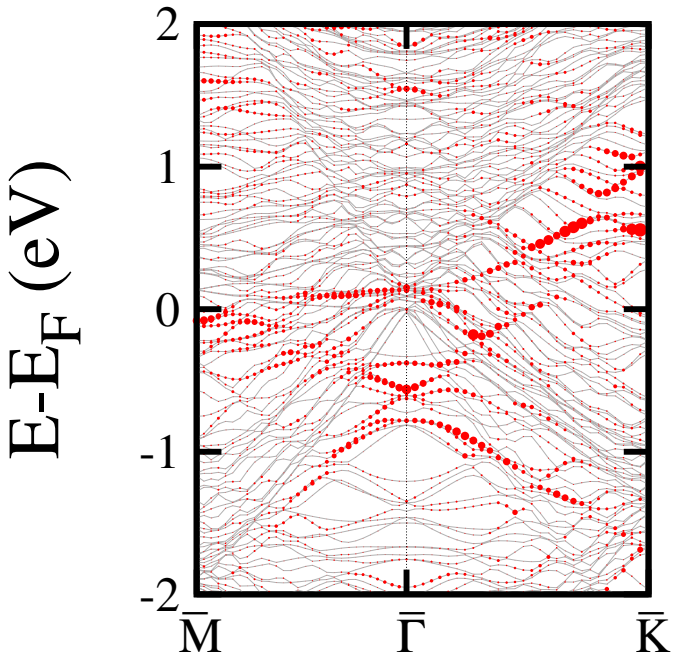

Figure 3.2: The projected band structure of 3×3 Si on 4×4 Ag(111) on p_z orbitals of Si. The radii of the red circles are proportional to the contribution from each state. The Fermi level was set at zero.

ing dangling bond of that Si atom. Connecting those nearest neighboring Ag atoms, one can obtain equilateral triangles with two different orientations touching each other at one of its vertices, forming a chain-like structure. Each set of triangles with one of these two orientations has C_3 symmetry with respect to the perpendicular axis along third-layer Si. Therefore, the name HCT is given to this model [52, 53, 54, 55, 56, 57].

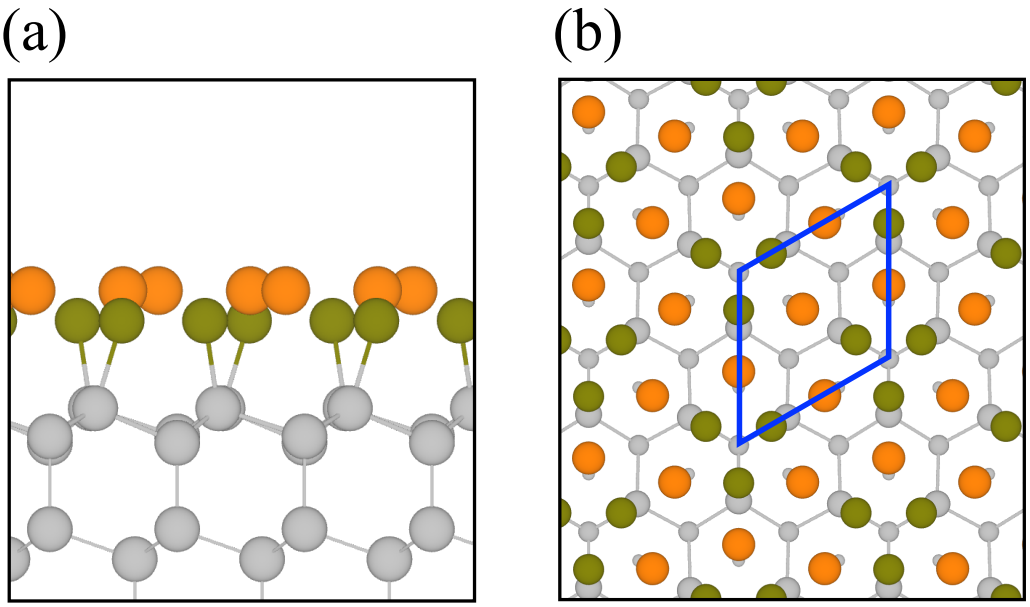

Figure 3.3: (a) Side view and (b) top view of the honeycomb chain trimer model, which serves as the model for the multilayer Si region in which the orange, dark-green, and gray spheres correspond to Ag, top-layer Si, and lower-layer Si atoms, respectively. The lower-layer Si atoms from top to bottom are labelled as the second-, third-, fourth-, and fifth-layer, respectively. The blue rhombus in (b) shows a $\sqrt{3} \times \sqrt{3}$R30° unit cell.

For the electronic band structure in Figure 3.4(a), we found a surface band in the gap of the Si bulk–projected band with a nearly linear dispersion region ranging from 0 to 1 eV in the $\bar{\Gamma}\bar{\mathrm{K}}$ direction with a large group velocity of approximately 0.86×10^6 m/s, consistent with the experimental results derived from the quasiparticle interference pattern for the system of Si on Ag in Ref. [48][$(1.2\pm0.1)\times10^6$ m/s]. Other surface states occurring at $\bar{\mathrm{K}}$ and $\bar{\mathrm{M}}$ just above the top of the valence band are also reported before [58]. The projected band structure in Figure 3.4(b)(c)(d) indicates that the linear dispersion is dominated by the $p_x + p_y$ orbitals of Si, rather than p_z, which is theoretically predicted to be the main wave

character of the linear band around the Fermi level in freestanding silicene. In addition, this surface band is due to the interaction between top-layer Si and top-layer Ag. Furthermore, the large group velocity implies delocalization of states, which can be visualized in the charge density isosurface in Figure 3.5(a) for the empty states in the energy range of 0.0–0.5 eV. In addition, Figure 3.5(a) reveals the presence of the charge and protrusion of the isosurface in the center of the Ag trimers. This can explain the bright dots observed in STM images with a positive sample bias, thus illustrating that these bright dots do not correspond to the atomic positions. By contrast, Figure 3.5(b) demonstrates the occupied states in the energy range of -1.0 to 0.0 eV and visualizes the chemical bonds formed by top-layer Si and top-layer Ag.

3.2 Few-layer Si model

For low coverage of Si on Ag(111), we constructed few-layer Si models to explain the emergence of the $\sqrt{3} \times \sqrt{3}$ phase. Because the $\sqrt{3} \times \sqrt{3}$ phase can coexist with the 3×3 phase [43], we began from the well-studied 3×3 phase and then added additional Si to it. In the 3×3 phase, the strong interaction between Si and the Ag substrate distorts the regular buckling pattern of freestanding silicene, and the buckling distance increases (Figure 3.1(a)). The frame shows that one-third of the Si atoms in the unit cell are upwardly buckled, whereas the other two-thirds are in the lower plane close to the substrate. In Figure 3.1(b), we add nine additional Si atoms in the 3×3 SC on top of the sites of one of its two sublattices. Furthermore, we slightly move the additional Si atoms laterally away from the Si atoms beneath such that their bonds are tilted away from the vertical lines. Moreover, we added adsorbed Ag atoms such that the configuration on the surface similar to that of the HCT model. After relaxation, a $\sqrt{3} \times \sqrt{3}$ phase develops out of the 3×3 phase. Furthermore, the additional 0.5 ML of Si can form covalent bonds with the first ML below and restore the symmetric regular-buckled structure. This situation suggests that the $\sqrt{3} \times \sqrt{3}$ phase is directly grown on top of the 3×3 phase.

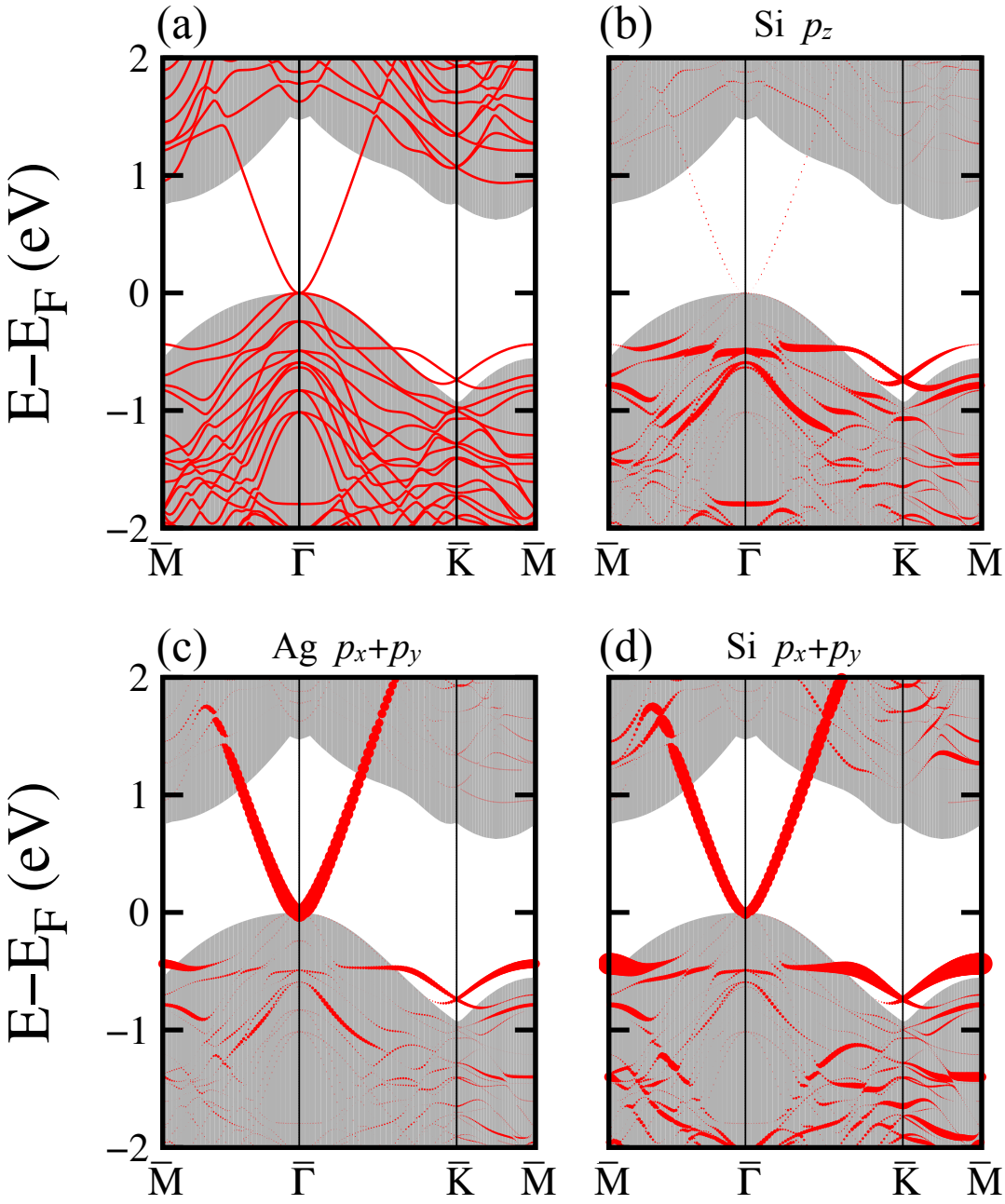

Figure 3.4: (a) The electronic band structure of the HCT model with the Si bulk-projected band is shown by gray region. The projected band structure on (b) p_z orbitals of top-layer Si and $p_x + p_y$ orbitals of (c) top-layer Ag and (d) top-layer Si, in which the radii of the red circles are proportional to the contribution from each state. The valence band maximum (VBM) was set at zero.

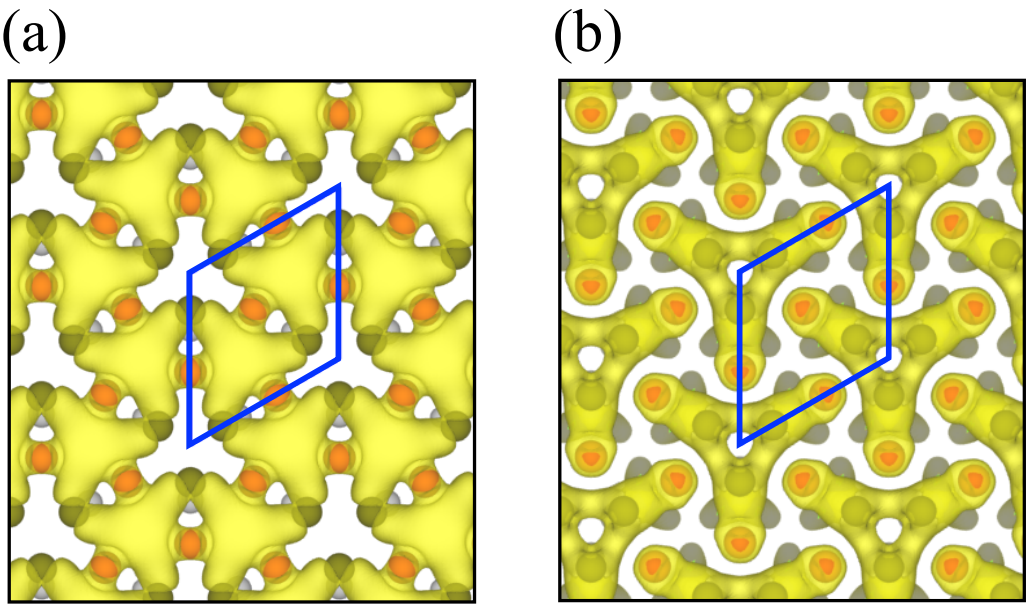

Figure 3.5: (a) The isosurfaces of the charge distribution of the HCT model for (a) the empty states within 0.5 eV above the Fermi level and (b) the occupied states within 1.0 eV below the Fermi level. The isosurface level for (a) is 0.0003, while that for (b) is 0.004 e/a_0^3, where a_0 is the Bohr radius.

To compare our model with the experimental results, we further calculated the electronic band structures. In the projected band structure calculation of the 1.5 ML of Si on Ag(111) model (Figure 3.6(a)), the states above the Fermi level projected to the top-layer Ag and top-layer Si are modulated by the states of the Ag substrate, and the dispersion is distorted and nonlinear. However, by adding another one ML of Si to the previously mentioned model, we established the 2.5 ML of Si on Ag(111) model (Figure 3.1(c)). The surface structure is similar to that of the HCT model. Moreover, its projected band structure (Figure 3.6(b)) demonstrates the emergence of a parabolic dispersion above the Fermi level. Noticeably, past the $\bar{\Gamma}$ point, a nearly linear dispersion similar to that of the surface state of the HCT model arises, as shown by the blue dashed line. Similarly, this linear band results from the interaction between top-layer Ag and top-layer Si.

Our calculated band structures imply that the claimed as-grown silicene is actually a few-layer Si thin film with Ag atoms on top. In addition, a 2.5 ML of Si is required for observing linear dispersion. We verified that the linear dispersion is due to the states

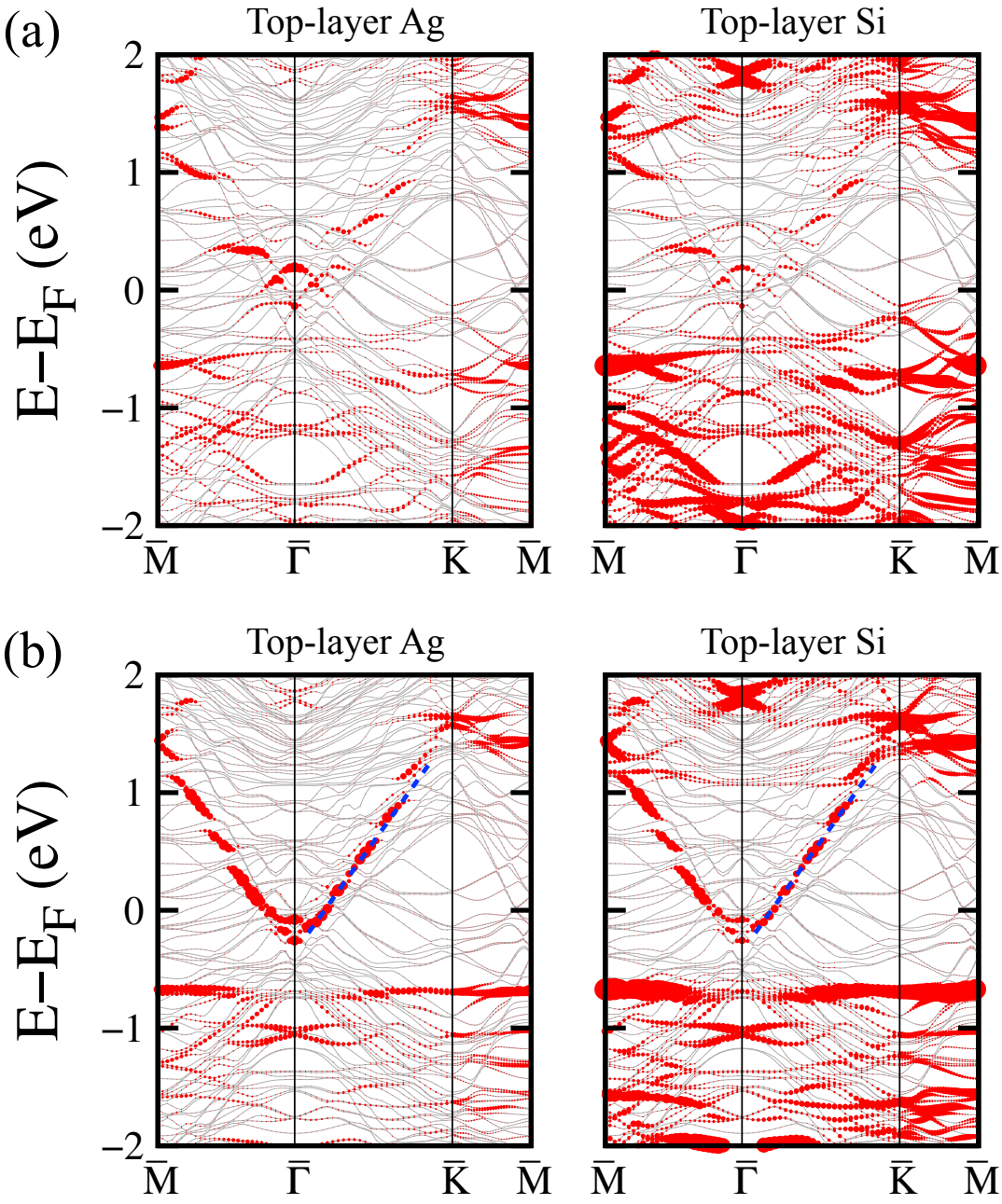

Figure 3.6: The projected band structure on the $p_x + p_y$ orbitals of top-layer Ag (left) and top-layer Si (right) of (a) the 1.5 ML of Si on Ag(111) model and (b) the 2.5 ML of Si on Ag(111) model. The radii of the red circles are proportional to the contribution from each state. The Fermi level was set at zero. The blue dashed lines show the nearly linear dispersion in some parts of the energy bands.

resulting from the Ag–Si interaction. To further explore these unique surface states, we conducted the STM simulation for all three proposed models, whose empty- and filled-state images are summarized in Figure 3.7 and Figure 3.8 for the constant height and current models, respectively. For all three models, the filled states with both lower (2.5 Å) and higher (5.0 Å) tip heights yield similar STM images. For higher-tip-height filled-state images, bright regions are more extended and connected, such that the calculated STM produces similar $\sqrt{3} \times \sqrt{3}$ patterns, as reported previously in Ref. [48]. Moreover, we found that as the 1.5 ML of Si on Ag(111) model transforms to the 2.5 ML of Si on Ag(111) model, the images become more similar to those of the HCT model. In particular, for the empty states, the STM patterns of the 2.5 ML of Si on Ag(111) model are much closer to those of the HCT model. Because the parabolic band starts to emerge in the projected band structure for the 2.5 ML of Si on Ag(111) model, as shown in Figure 3.6(b), we conclude that increasing the number of added Si layers can render the electronic properties similar to those of the original HCT model.

Notably, a $\sqrt{21} \times \sqrt{21}$ superstructure on the $\sqrt{3} \times \sqrt{3}$ phase was reported in Ref. [59] when few-layer Si atoms were present on Ag(111) substrate (Figure 3.9(a)). While the red rhombus shows a $\sqrt{3} \times \sqrt{3}$ unit cell, some hexagons with brighter edges form a $\sqrt{21} \times \sqrt{21}$ superstructure, indicated using black rhombus. Because this structure is prepared with experimental processes similar to those for $\sqrt{3} \times \sqrt{3}$ phase growth, we constructed a similar 1.5 ML of Si on Ag(111) model with a $\sqrt{21} \times \sqrt{21}$ SC comprising a twisted overlayer of 1.5 ML of Si with respect to the underlying Ag(111) lattice. The relaxed atomic configuration, illustrated in Figure 3.9(b), demonstrates that a $\sqrt{3} \times \sqrt{3}$ HCT pattern formed on the surface of this structure. Moreover, the calculated STM image (Figure 3.9(d)) resembles the patterns observed in the experiment (Figure 3.9(a)). This similarity provides concrete theoretical evidence for the presence of the HCT structure on the surface.

Another theoretically proposed model, the honeycomb dumbbell silicene structure, was adopted to explain the formation mechanism of the $\sqrt{3} \times \sqrt{3}$ Si phase on Ag(111) [60],

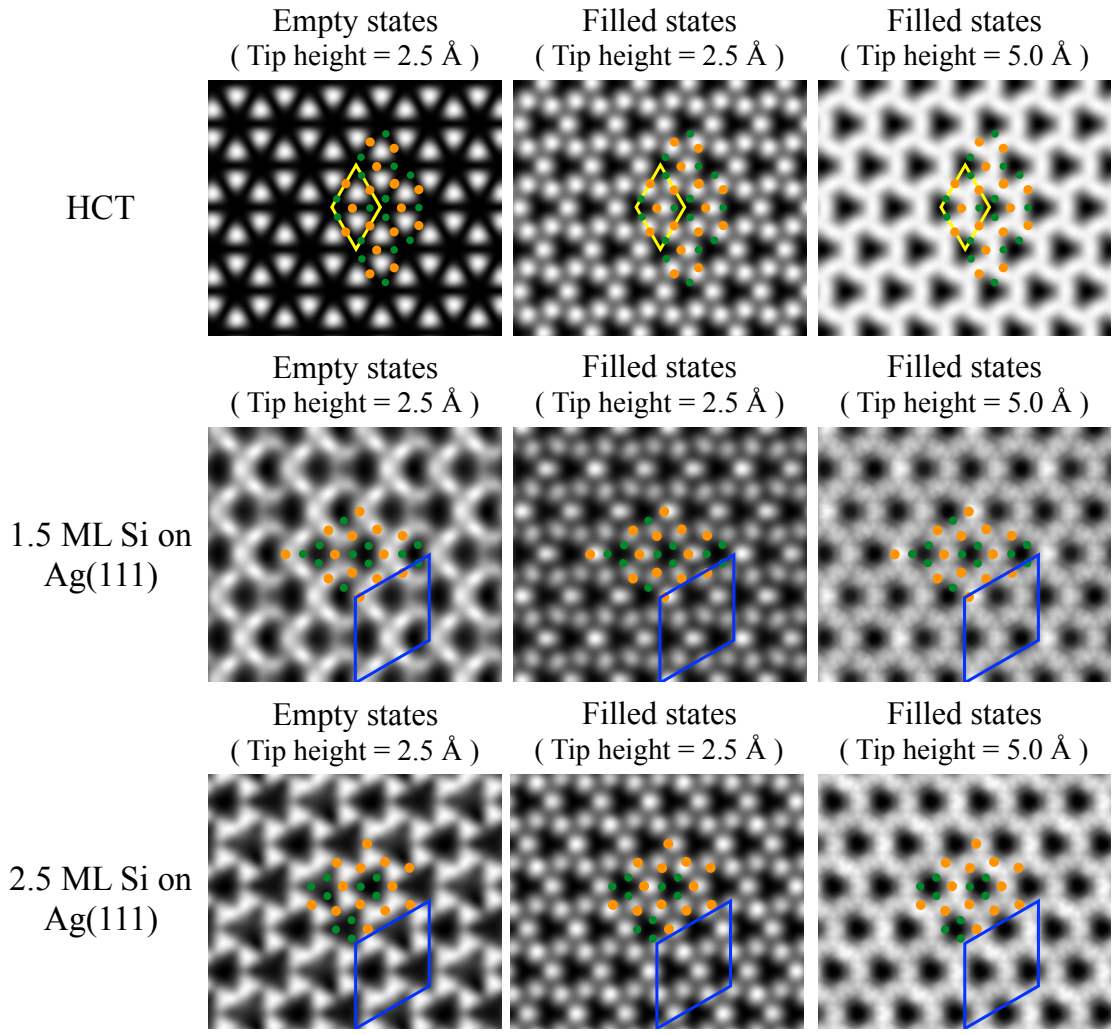

Figure 3.7: Calculated STM images of the HCT model, the 1.5 ML of Si on Ag(111) model, and the 2.5 ML of Si on Ag(111) model with the constant-height mode. The orange and green spheres represent the top-layer Ag and top-layer Si atoms, respectively. The yellow rhombuses show the $\sqrt{3} \times \sqrt{3}$ reconstruction while the blue rhombuses show the 3×3 unit cells. Empty states are calculated from partial charge density in the energy range between E_F to E_F+0.5 eV, while filled states are taken from the energy range between $E_F - 1.0$ to E_F eV.

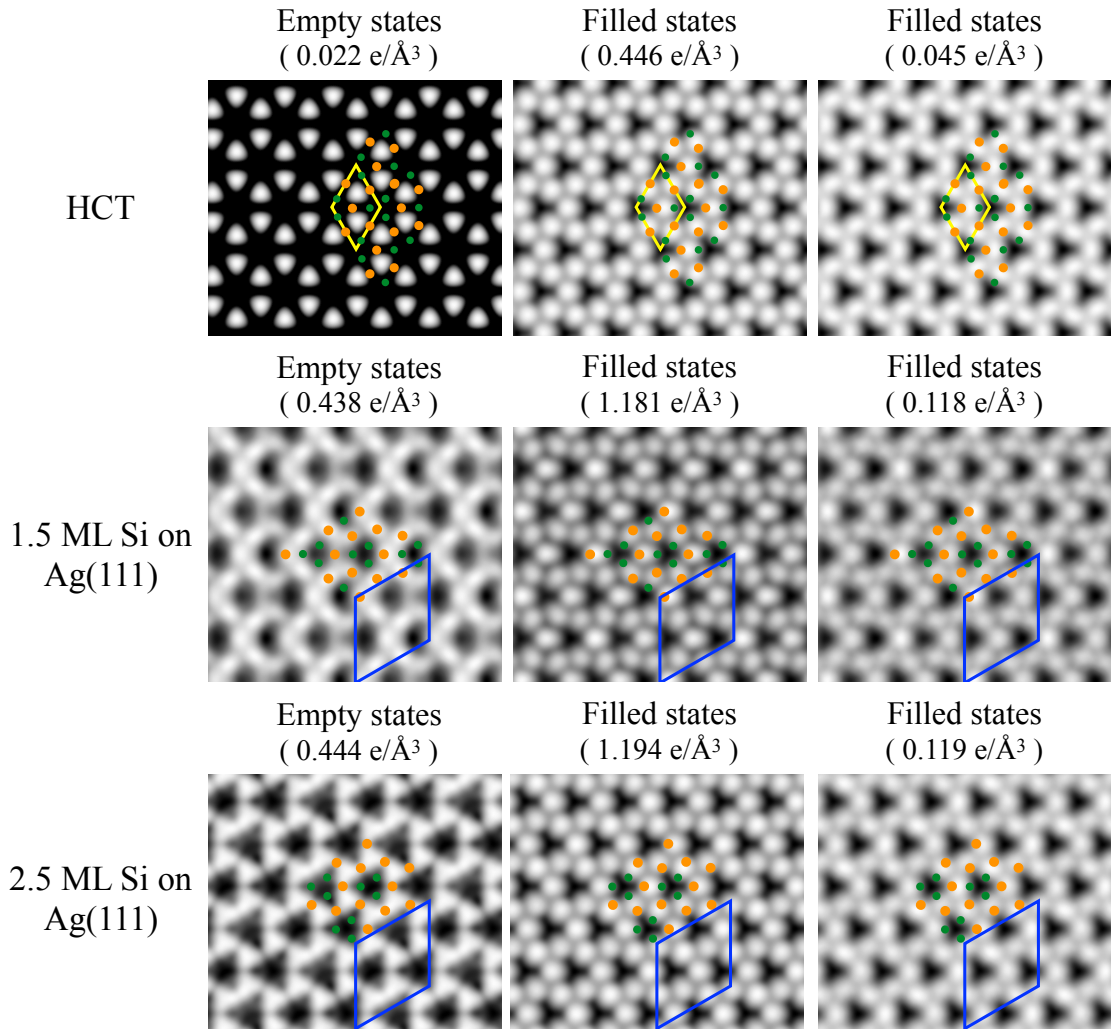

Figure 3.8: Calculated STM images of the HCT model, the 1.5 ML of Si on Ag(111) model, and the 2.5 ML of Si on Ag(111) model with the constant-current mode. The orange and green spheres represent the top-layer Ag and top-layer Si atoms, respectively. The yellow rhombuses show the $\sqrt{3} \times \sqrt{3}$ reconstruction while the blue rhombuses show the 3×3 unit cells. Empty states are calculated from partial charge density in the energy range between E_F to E_F+0.5 eV, while filled states are taken from the energy range between $E_F - 1.0$ to E_F eV.

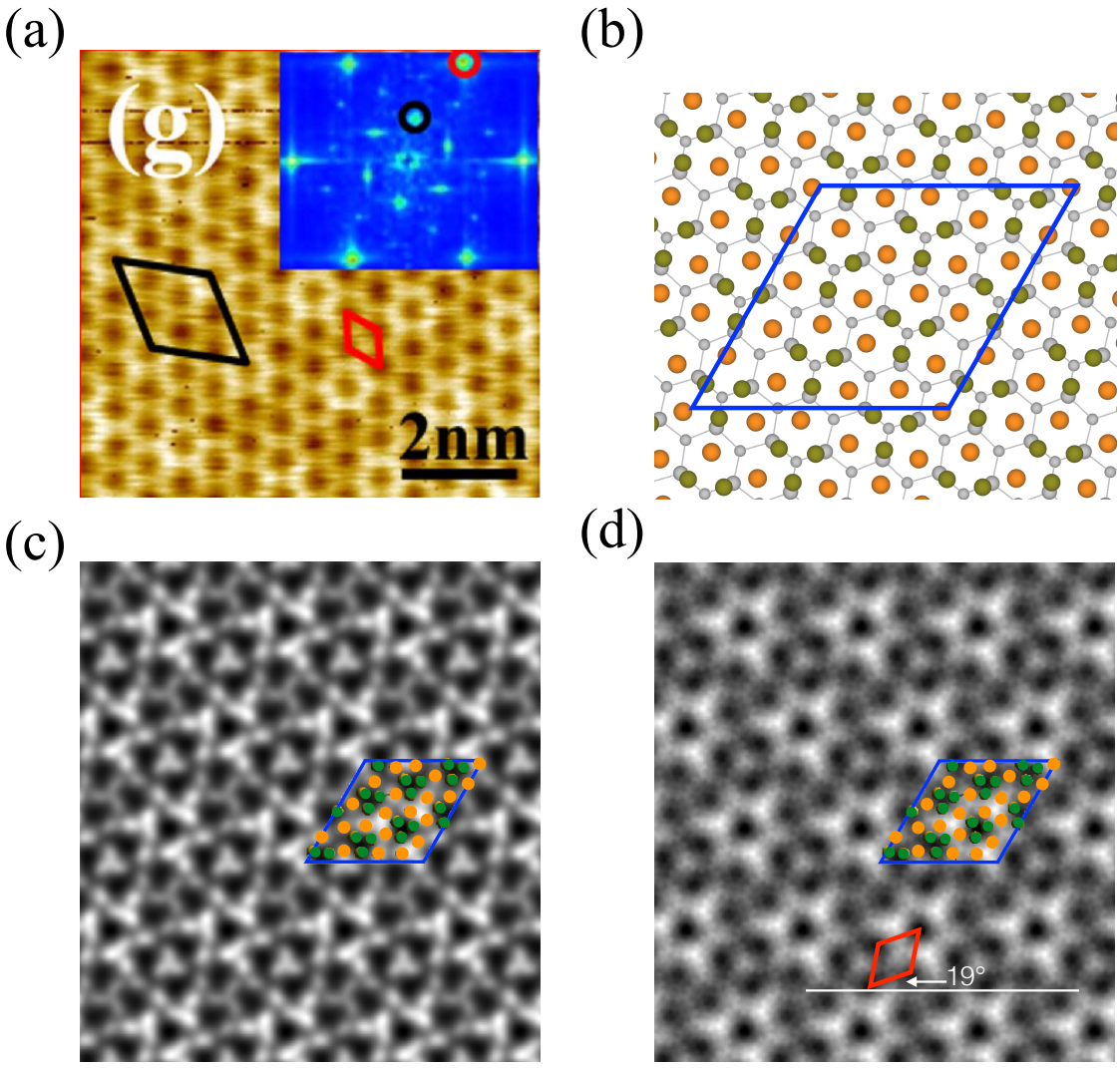

Figure 3.9: The $\sqrt{3} \times \sqrt{3}$ phase with a $\sqrt{21} \times \sqrt{21}$ superstructure. (a) The previously reported STM image taken from Figure 2(g) of Ref. [59], corresponding to a sample bias of $+1.5$V. (b) Top view of the of $\sqrt{21} \times \sqrt{21}$ supercell used in our calculation with the HCT model on the surface. Calculated empty-states STM with tip-height of (c) 2.5 Å and (d) 5 Å. In (b)(c)(d), the orange and green spheres represent top-layer Ag and top-layer Si atoms, respectively, and the blue rhombuses show the $\sqrt{21} \times \sqrt{21}$ supercells. In (d), the red rhombus shows the $\sqrt{3} \times \sqrt{3}$ reconstruction, which is rotated by 19° with respect to the blue one.

in which the additional Si atoms were adsorbed on top of the lower buckled Si atoms. If the coverage of the adsorbed Si atoms is two-thirds of one ML, a $\sqrt{3} \times \sqrt{3}$ honeycomb structure can appear. However, Table 3.1 indicates that the absorption energy per added Si of our 2.5 ML of Si on Ag(111) model is the lowest, implying highest probability of our model forming among all models. Furthermore, the energies of the Si atoms in our models are close to those in Si bulk. According to the calculated results shown above, we believe that the $\sqrt{3} \times \sqrt{3}$ phase on the multilayer region is a Si thin film with the HCT surface grown on the Ag(111) substrate.

Table 3.1: The energetics of proposed models for the $\sqrt{3} \times \sqrt{3}$ phase.

Models	Lattice constant (Å)	Binding energy (eV/ Si atom)	Absorption energy of added Si (eV/added atom)	Energy relative to Si bulk (eV/added atom)
silicene	6.698	-4.788	-4.788	0.64
TDS [61]	6.520	-4.837	-5.127	0.30
HDS [61]	6.388	-4.835	-4.825	0.60
3x3 phase		-5.243	-5.243	0.19
1.5 ML Si on Ag(111)		-5.218	-5.169	0.26
2.5 ML Si on Ag(111)		-5.295	-5.409	0.02

3.3 Computational details

We performed the total-energy calculation with DFT implemented in the VASP. [62, 63] The plane-wave basis-set was adopted and the PAW pseudopotentials were used. The PBE form [15] of the exchange-correlation functional was applied in this calculation. We used the periodic-slab method to model the surface structure with a vacuum region of about 11–15 Å. For the HCT model, the energy cut-off of the plane-wave basis-set is 500 eV with the Monkhorst-Pack k-point mesh of $7\times7\times1$. The substrate has ten layers of Si with the bottom eight layers of Si fixed. The surface layer is composed of one layer Si and one layer Ag. The vacuum region is about 14 Å. For the 1.5 ML of Si on Ag(111) model, the energy

cut-off is 300 eV with the Monkhorst-Pack k-point mesh of $5\times5\times1$. The substrate has six layers of Ag with the bottom two layers fixed. The vacuum region is about 14 Å. For the 2.5 ML of Si on Ag(111) model, the vacuum region changes to about 11 Å.

3.4 Conclusions

In conclusion, band dispersion and STM simulation indicate that the Si(111)–$\sqrt{3}\times\sqrt{3}$–Ag structure serves as the model for the $\sqrt{3}\times\sqrt{3}$ reconstruction in the multilayer Si region. Furthermore, the 3×3 phase transforms into the $\sqrt{3}\times\sqrt{3}$ phase when the Si coverage increases beyond one ML. Moreover, this 2.5 ML of Si on Ag(111) model exhibits a nearly linear surface band above the Fermi level. However, these states result from the interaction between the top-layer Si and top-layer Ag atoms, rather than 2D Dirac electrons in silicene.

CHAPTER 4

ELECTRONIC PROPERTIES OF SINGLE-LAYER HEXAGONAL BORON NITRIDE ON METALLIC SUBSTRATES

As scholars continue to report an increasing number of 2D materials, the potential applications of the heterostructures formed by vertically stacking these materials as layer units have been studied intensely [64, 65, 66, 67]. A unique phenomenon of the heterostructures, frequently observed through STM, is the moiré pattern [68, 69, 70, 71, 72, 73], a large-scale pattern that emerges when two layers with slightly different periodicities superimpose. Although moiré patterns are widely observed during 2D heterostructure fabrication, the related microscopic topographies and their effects on electronic properties are not completely understood. Here, we studied an insulating *h*-BN layer, grown on hexagonal transition metallic surfaces with the focus on that of a hcp metal, Ru(0001), and that of a fcc metal, Cu(111).

h-BN possesses a hexagonal structure similar to that of graphene, except that the two of its sublattices are composed of different species (i.e., B and N atoms), which break the inversion symmetry. In addition, the great variance in electronegativity between B and N atoms leads to a wide band gap of 5–6 eV [74, 75]. The chemical reaction of thermal decomposition of borazine ($B_3N_3H_6$) on high-temperature transition metals was used to synthesize large *h*-BN layer [76, 77, 78, 79, 80]. Moreover, the absence of dangling bonds provides an ideal growth platform for other 2D materials. *h*-BN has recently attracted attention because of its promising role as a substrate material. One of its most appealing features is as follows: the mobility of exfoliated graphene increases by almost an order of magnitude when mechanically transferred onto the *h*-BN substrate [81] compared with that onto SiO_2. This finding also launches a new era for searching multiple vdW heterostructures.

In addition to the unique characteristics of an isolated *h*-BN sheet, tunable physical

properties possibly arise from the moiré pattern induced by lattice mismatch between *h*-BN and the underlying substrate. For instance, the modulated interaction in the *h*-BN–metal interfaces can lead to a periodically corrugated *h*-BN layer. In this chapter, we first study *h*-BN on Ru(0001) and then on Cu(111), both of which display different degrees of *h*-BN–substrate interactions. Experiments indicate that *h*-BN/Ru(0001) heterostructures consistently form moiré patterns with periodicities of approximately 3.2 nm, but the wavelengths of *h*-BN/Cu(111) moiré patterns range from 4 to 14 nm. To gain insight into the formation and effect of moiré patterns, we developed a theoretical model, in which a SC commensurate with both *h*-BN and metal surface is constructed. The SC model reduces the computational cost, but increases the feasibility of studying the electronic properties. We performed first-principles calculations based on DFT and demonstrated that the corrugation of the *h*-BN layer on Ru(0001) is as large as 1.7 Å, but $<$0.3 Å on Cu(111). We have also verified that the hole region of *h*-BN in the heterostructure is composed of N atoms on top of underlying metal atoms. Finally, the PDOS and electrostatic potential values confirm the observed band gap modulation and the local work function variation of the heterostructure. Such systems can be promising template surfaces for molecular assembly.

4.1 *h*-BN on Ru(0001)

Since the discovery of the large-scale nanomesh structure in *h*-BN/Rh(111) heterostructure, the interaction between *h*-BN and transition metal substrates has attracted considerable attention [82]. As a similar transition metal to Rh with a close lattice constant of approximately 2.7 Å, Ru has become another substrate useful for investigating the appearance of distinctive moiré patterns on *h*-BN/Rh(111). A similar nanomesh structure can form on *h*-BN/Ru(0001); this may be because Ru has electronic configurations similar to Rh and they involve similar catalytic reactions in the thermal decomposition of $B_3N_3H_6$ [83]. Although the nanomesh structure has been studied theoretically [84], reinvestigating this nanostructure using first-principles calculations based purely on a plane wave

basis is necessary. In addition, Ref. [85] studied the heterostructure with $MoSe_2$ grown on *h*-BN/Ru(0001) and found a moiré pattern on $MoSe_2$, with the periodicity identical to that on *h*-BN/Ru(0001), which cannot be originated from $MoSe_2$/*h*-BN heterostructure. Moreover, the tunneling spectra demonstrated that the $MoSe_2$ band edge has a spatial modulation of approximately 0.13 eV, quantitatively close to the amplitude of the local work function modulation in *h*-BN. Notably, the work function modulation measured on both $MoSe_2$/*h*-BN/Ru(0001) and *h*-BN/Ru(0001) exhibits almost identical amplitude, demonstrating real-space electrostatic tuning of the band profile.

The rotationally aligned *h*-BN on Ru(111) can be described by a SC of approximately 3.2 nm, corresponding to that of a 13×13 *h*-BN and 12×12 Ru(0001) lattice. To increase the efficiency of the calculations, we constructed smaller SCs with finite rotation angles on *h*-BN with respect to Ru(0001), including 6×6 *h*-BN/$\sqrt{31} \times \sqrt{31}$ Ru(0001)R8.95°, $\sqrt{57} \times \sqrt{57}$ *h*-BN/7×7 Ru(0001)R6.59°, and $\sqrt{67} \times \sqrt{67}$ *h*-BN/$\sqrt{57} \times \sqrt{57}$ Ru(0001)R5.63°; these SCs contain 36, 57, and 67 BN pairs, respectively, and have lengths of approximately 1.5, 1.9, and 2.1 nm, respectively. Notably, these SCs provide the essential collection of different atomic registries between the layers. Meanwhile, the strain levels applied on the layer are reasonable, such that the calculated electronic properties are reliable.

We performed first-principles calculations with DFT as implemented in the VASP [62]. We used the PAW method [9] to treat core electrons, and the PBE [15] form for the exchange-correlation functional with a plane wave energy cutoff of 400 eV. The periodic slabs contain three Ru layers as the substrate and a vacuum region of approximately 13 Å. The bottom Ru layer is fixed, whereas the other two Ru layers and *h*-BN layer are allowed to move during the geometry optimization. The lattice constant of *h*-BN was fixed at a calculated value of 2.52 Å, whereas that of Ru(0001) changes from its calculated value of about 2.72 Å by 0.5%. The optimized atomic configurations of these SCs are presented in Figure 4.1, where the orange, blue, and black circles in the top view of Figure 4.1(c) indicate the regions with B (N) atoms located at fcc (top), top (hcp), and hcp (fcc) positions

with respect to underlying Ru atoms, which are labeled as $B_{fcc}N_{top}$, $B_{top}N_{hcp}$, and $B_{hcp}N_{fcc}$, respectively. The side views of the optimized atomic configuration, shown in right panels of Figure 4.1, indicate that a certain portion of the *h*-BN layer moves closer to the Ru substrate. In the regions indicated by both the blue and black circles, which are called the wire regions, the distances between *h*-BN and the Ru surface layer were approximately 3.7 Å for all the three models. However, in the region indicated by the orange circle, referred to as the hole region, in which N atoms are approximately located above Ru atoms, the average interlayer distance varies from 2.57 Å in Figure 4.1(a) to 2.20 Å in Figure 4.1(c), producing a maximal height difference (corrugation) in *h*-BN layer of approximately 1.05 Å in Figure 4.1(a) to 1.67 Å in Figure 4.1(c), in agreement with calculated results previously obtained with different SCs, basis sets, and exchange-correlation functionals [84, 86]. Moreover, strong bonding occurs in the orange region with charge transfer from *h*-BN to the Ru substrate (Figure 4.2).

The band edge and the local work function modulation of $MoSe_2$ on *h*-BN/Ru(0001) can be observed through STS and field-emission-resonance spectra, respectively [85]. The periodic modulation of the band profile on $MoSe_2$ is associated with the work function modulation induced by the moiré pattern on *h*-BN/Ru(0001). The location-specific STS measurements taken from the hole and wire regions indicated a rigid shift of 0.13 eV for the absolute values of the conduction band (CB) minimum (CBM) and the valence band (VB) maximum (VBM). Meanwhile, the band gap values remain the same for both the hole and wire regions. In addition, the field-emission-resonance spectra, in which the bias of the first peak is considered a good approximation of the work function of the sample, indicate a downward shift of 0.15 eV from the hole to the wire region. Assuming the band edge shift of $MoSe_2$ is purely due to the electrostatic potential originating from the *h*-BN/Ru(0001) heterostructure, we could use our results of *h*-BN/Ru(0001) to explain these modulations of electronic properties observed on $MoSe_2$. In our calculation, we evaluate the local work function by subtracting the Fermi level from the electrostatic potential at 4.9 Å above the

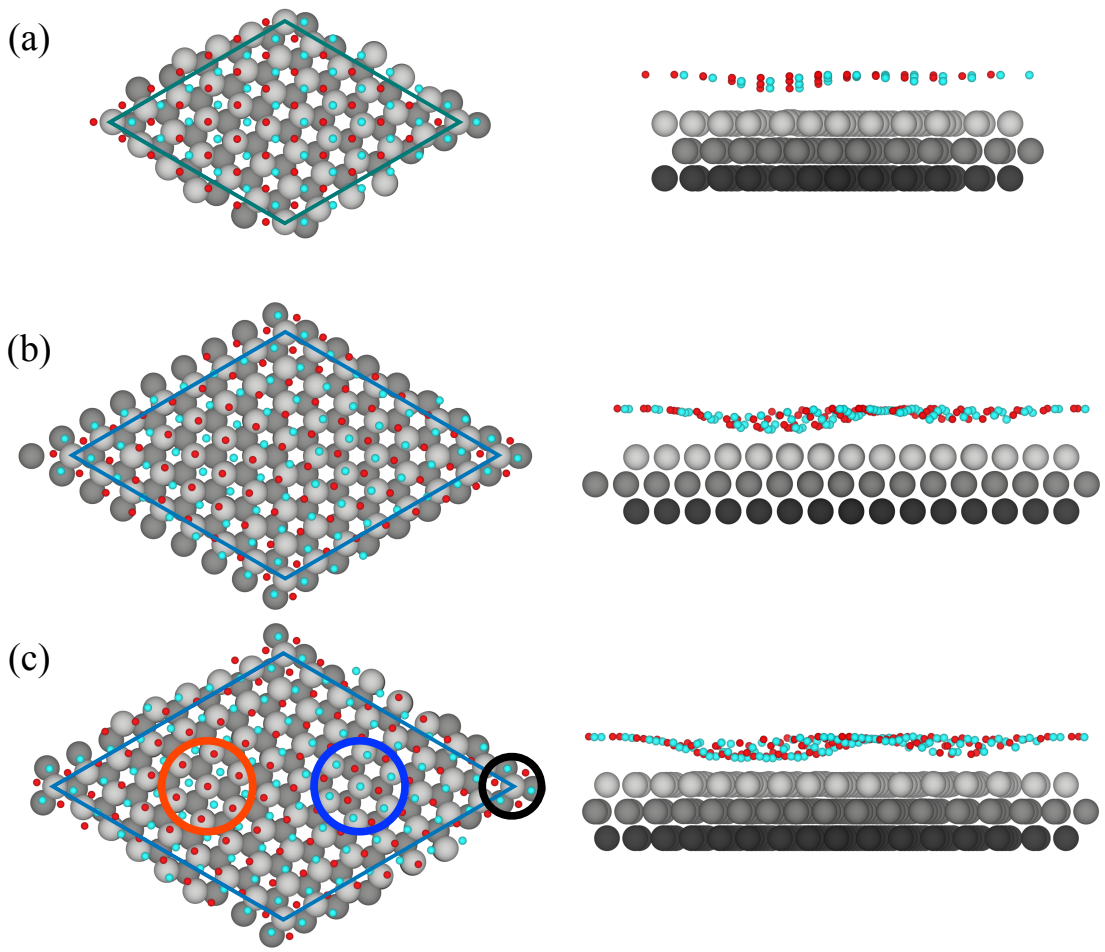

Figure 4.1: Top view (left) and side view (right) of the atomic configurations for *h*-BN grown on Ru(0001) in the supercells containing (a) 6×6 *h*-BN on $\sqrt{31} \times \sqrt{31}$ Ru(0001), (b) $\sqrt{57} \times \sqrt{57}$ *h*-BN on 7×7 Ru(0001), and (c) $\sqrt{67} \times \sqrt{67}$ *h*-BN on $\sqrt{57} \times \sqrt{57}$ Ru(0001). The red, light-blue, and gray spheres represent N, B, and Ru atoms, respectively. The deeper the gray color, the farther the Ru atoms away from the *h*-BN layer. The orange, blue, and black circles in (c) indicate the regions with N atoms at the top, hexagonal close-packed (hcp), and face-centered cubic (fcc) sites with respect to the Ru(0001) substrate, which are labelled as $B_{fcc}N_{top}$, $B_{top}N_{hcp}$, and $B_{hcp}N_{fcc}$, respectively.

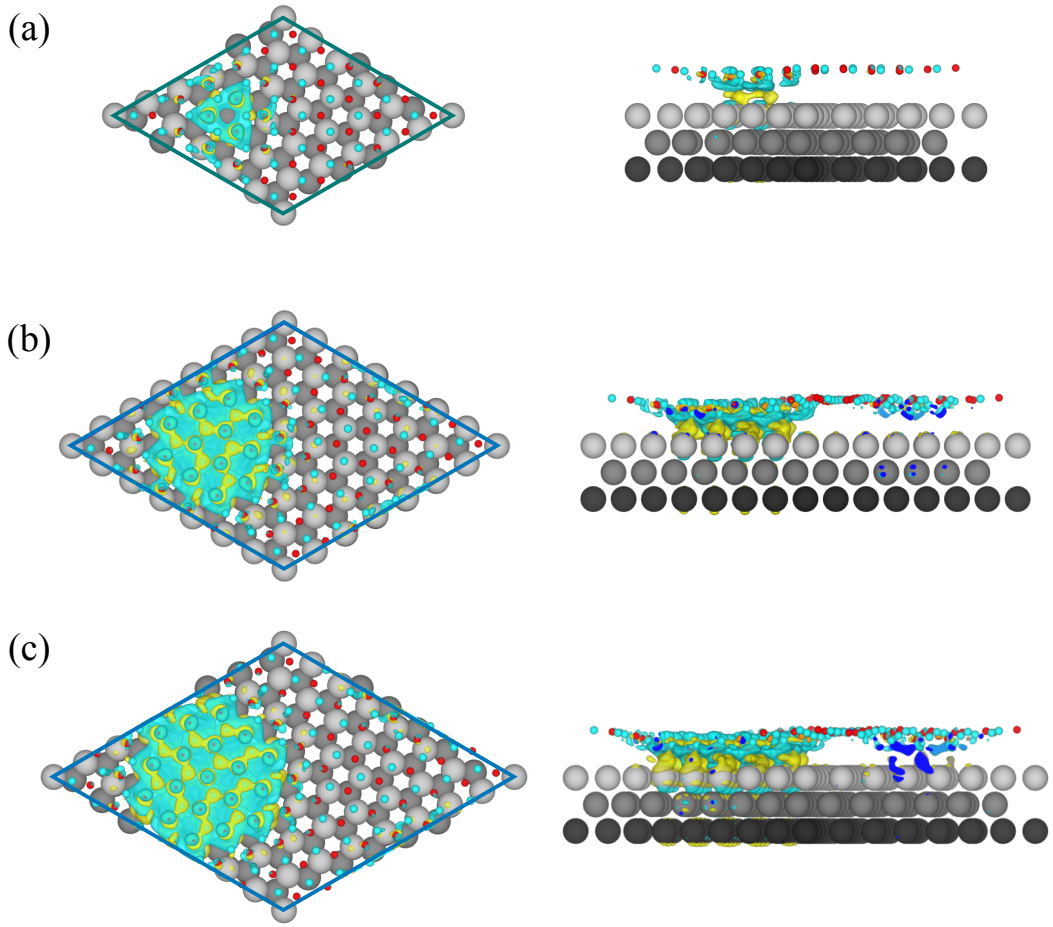

Figure 4.2: Calculated charge density difference ($\Delta\rho$) given by the formula: $\Delta\rho = \rho_{h\text{-BN/Ru}} - \rho_{\text{BN}} - \rho_{\text{Ru}}$, in which $\rho_{h\text{-BN}}$ (ρ_{Ru}) was obtained from fixed and fully relaxed *h*-BN/Ru with Ru (*h*-BN) removed. Configurations shown are (a) 6×6 *h*-BN on $\sqrt{31}\times\sqrt{31}$ Ru(0001), (b) $\sqrt{57}\times\sqrt{57}$ *h*-BN on 7×7 Ru(0001), and (c) $\sqrt{67}\times\sqrt{67}$ *h*-BN on $\sqrt{57}\times\sqrt{57}$ Ru(0001). The charge density differences are induced by the interaction, with the yellow (blue) isosurfaces indicating an increase (decrease) in the charge density with an isosurface level of 0.0015 e/a_0^3, where a_0 is the Bohr radius. Results show that surface dipoles form with the direction pointing out of the surface of the heterostructure.

h-BN layer (average of the vdW layer separations between *h*-BN and $MoSe_2$; Figure 4.3). The results demonstrated that the local work function in the hole region is lower than that in the wire region by 0.10 and 0.15 eV for the models (Figure 4.1(b) and (c), respectively). The modulation increases as the SC becomes larger, which is possibly due to the increase of the charge transfer in the hole region, resulting in a higher degree of potential reduction in the vacuum above. Thus, a larger calculated value of local work function modulation in the rotationally aligned 13×13 *h*-BN/12×12 Ru(0001) heterostructure is expected.

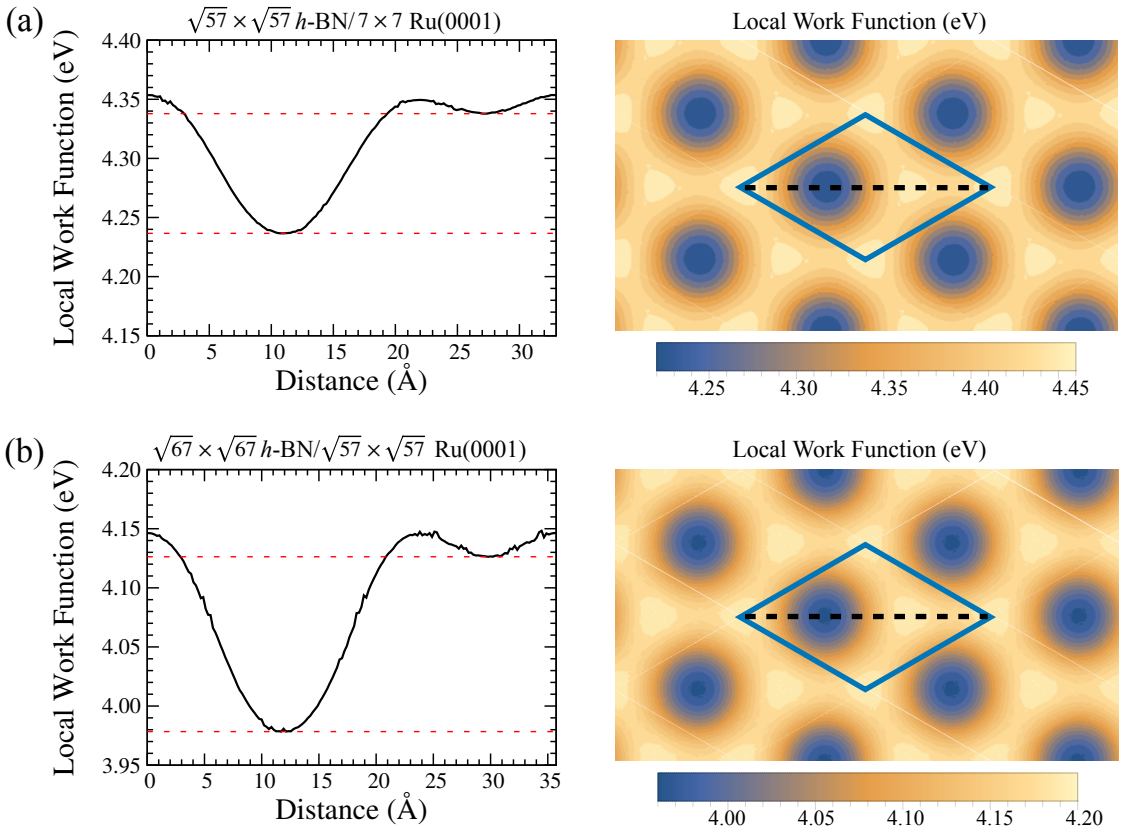

Figure 4.3: Calculated local work function variations by subtracting the Fermi level from the potential surface at the height of 4.9 Å above the *h*-BN layer, which corresponds to the average of the interlayer distances of *h*-BN and $MoSe_2$ for (a) $\sqrt{57} \times \sqrt{57}$ *h*-BN on 7×7 Ru(0001) and (b) $\sqrt{67} \times \sqrt{67}$ *h*-BN on $\sqrt{57} \times \sqrt{57}$ Ru(0001), in which the upper (lower) red dashed line indicates the minimum at the wire (hole) region. The distance is calculated from the left end point of the black dashed lines, labelled in the constant-potential contour map on the right, in which holes arrange in a hexagonal pattern. The supercell is indicated in a aqua blue rhombus.

The PDOS, shown in Figure 4.4, confirms that the significant interaction between *h*-BN and the Ru substrate in the hole region induces states in the *h*-BN gap, producing a remnant metallic characteristic. On comparing Figure 4.5(a) and (c), we noted that these induced states result from the hybridization between N p_z and Ru d_{z^2} in the hole region. By contrast, the other regions of *h*-BN have a wide band gap (>4 eV). This partial metallization can explain the renormalization of the band gap of $MoSe_2$ grown on *h*-BN/Ru(0001) [85] because metallized *h*-BN improves $MoSe_2$ screening, resulting in a smaller quasiparticle band gap of $MoSe_2$ on *h*-BN/Ru(0001), compared with the measured values on graphene or graphite. Moreover, on comparing Figure 4.5(a) and (b), we noted that the induced states for $p_x + p_y$ in the hole region in the energy range of -3 to -2 eV. These induced states can be explained by the hybridization with p_z orbitals, confirming the fact that the *h*-BN layer is no longer flat and concaved upward in the hole region.

In summary, our relaxation calculation shows that the *h*-BN layer grown on a Ru substrate has a regular periodic corrugation, which can also verify that the hole regions of the moiré patterns observed in the *h*-BN/Ru heterostructure are composed of N atoms on top of underlying Ru atoms. The differential charge distribution indicates that electrons in the $B_{fcc}N_{top}$ region transfer from the *h*-BN layer to the substrate, modulating the local work function on the moiré pattern and spatially modifying the band edge on the as-grown $MoSe_2$. Finally, our PDOS results indicated that the hybridization between N p_z and Ru d_{z^2} induces states within the band gap of *h*-BN, rendering *h*-BN metallization.

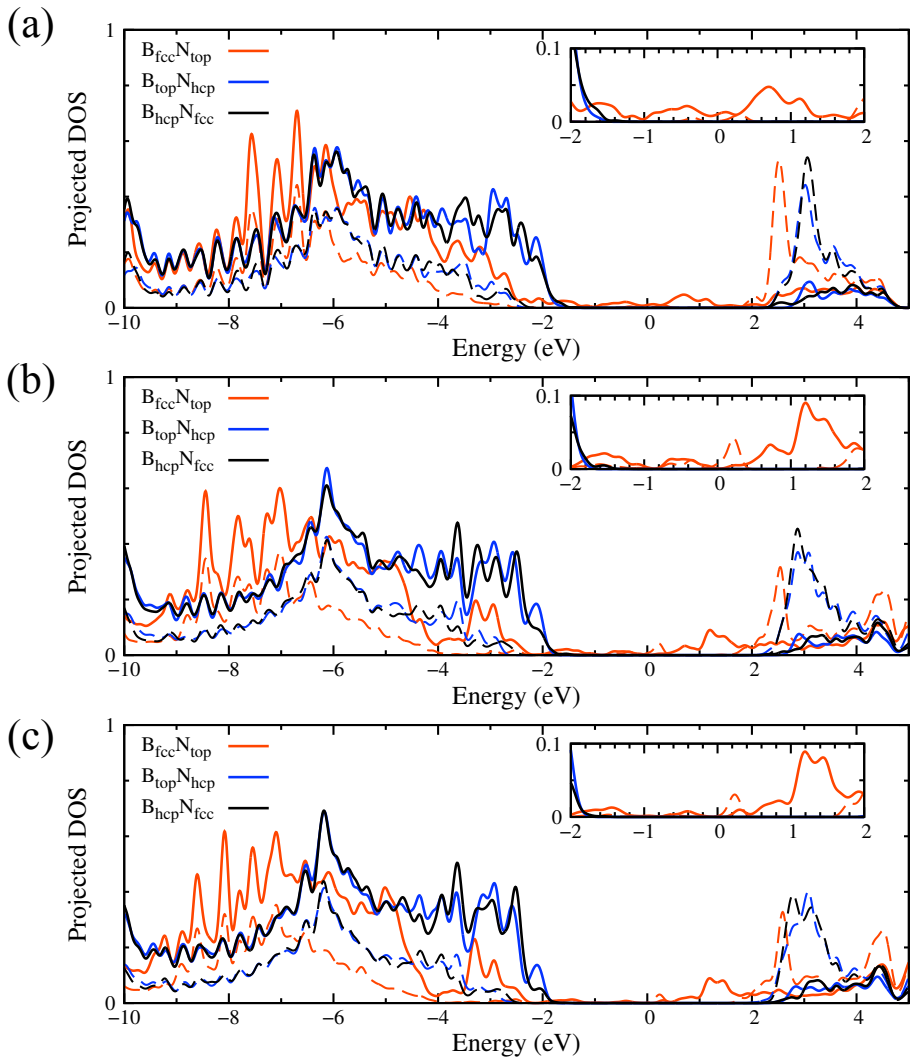

Figure 4.4: Site-projected density of states in the regions of $B_{fcc}N_{top}$, $B_{top}N_{hcp}$, and $B_{hcp}N_{fcc}$, shown in the orange, blue, and black curves for the p orbitals of B (dashed lines) and N (solid lines) atoms in the (a) 6×6 *h*-BN/$\sqrt{31} \times \sqrt{31}$ Ru(0001), (b) $\sqrt{57} \times \sqrt{57}$ *h*-BN/7×7 Ru(0001), and (c) $\sqrt{67} \times \sqrt{67}$ *h*-BN/$\sqrt{57} \times \sqrt{57}$ Ru(0001) structures. The Fermi level is set as the zero energy.

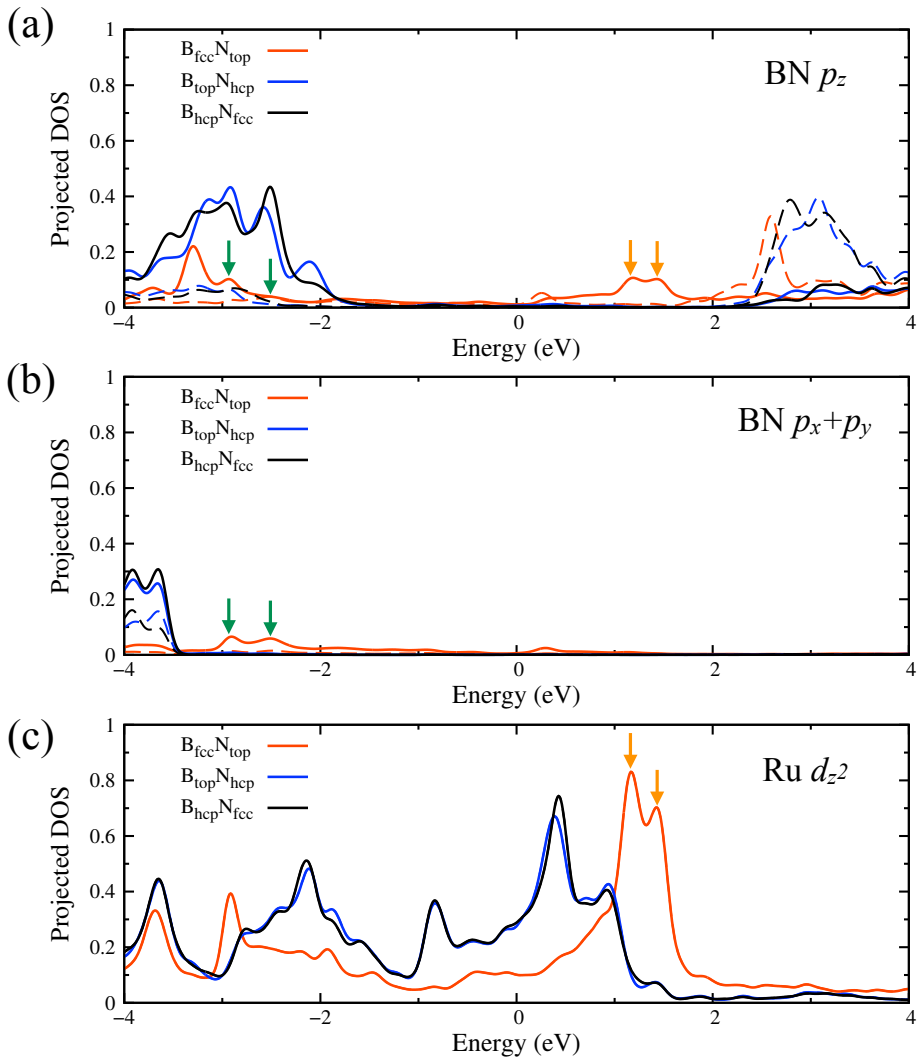

Figure 4.5: Site- and orbital-projected density of states in the regions of $B_{fcc}N_{top}$, $B_{top}N_{hcp}$, and $B_{hcp}N_{fcc}$, shown in the orange, blue, and black curves for the (a) p_z and (b) $p_x + p_y$ orbitals of B (dashed lines) and N (solid lines) atoms and (c) d_{z^2} orbitals of top-layer Ru in the $\sqrt{67} \times \sqrt{67}$ *h*-BN/$\sqrt{57} \times \sqrt{57}$ Ru(0001) structure. Green arrows indicate the induced peaks with the common energy shown in (a) and (b), while orange arrows label the induced peaks with the same energy shown in (a) and (c). The Fermi level is set as the zero energy.

4.2 *h*-BN on Cu(111)

Cu(111) is a commonly used substrate for the growth of *h*-BN because of its low cost and convenient availability. In contrast to a large lattice mismatch between *h*-BN and Ru(0001), Cu(111) demonstrates only 2% lattice mismatch with bulk *h*-BN, with the experimental values of $a_{\mathrm{Cu(111)}}$=2.556 Å [87] and $a_{h\text{-BN}}$=2.504 Å [88]. In addition, Cu foils have good catalytic functions for high-quality fabrication of *h*-BN, facilitates mass production of large-scale *h*-BN films. Furthermore, large-scale growth of *h*-BN facilitates the realization of graphene-based devices. Thus, examining the unique heterostructure of *h*-BN/Cu(111) is important.

Over the last decade, numerous studies on successful growth of *h*-BN on Cu(111) have been published [89, 90, 91, 92]. It has been experimentally verified that although *h*-BN–Ni is chemisorbed, *h*-BN–Cu is more like a physisorbed interface [78], implying weakly coupling between *h*-BN and the Cu(111) substrate. However, as in the case of *h*-BN on Ru, the moiré patterns of *h*-BN/Cu(111) have been detected through STM and STS [89]. Recently, the mean interlayer spacing between *h*-BN and a Cu substrate was unambiguously measured to be 3.38±0.06 Å through X-ray standing waves, whereas *h*-BN layer corrugation can be determined by analyzing the atomic contrast in atomic force field measurements, which shows that the hole region of the moiré pattern is 0.3–0.7 Å closer to the substrate [92]. Ref. [93] demonstrated that the STM image contrast of the moiré pattern on *h*-BN/Cu(111) is dominated by the electronic variation, rather than the structural modulation. Clear moiré patterns emerge at the higher bias voltage (V_b=4 V), in which bright areas are labeled holes and the surrounding dimer regions are labeled wires. The wavelengths of these moiré patterns range from 4 to 14 nm, which reflects the weak *h*–Cu(111) interaction [89]. Moreover, a clear shift in the field-emission-resonance spectra suggests a large spatial modulation of the local work function. This observation again confirms that a large local work function modulation can exist even if the interaction between *h*-BN and

Cu(111) is weak. In addition, *h*-BN grown on Cu(111) remains a large-band-gap insulator, rather than being metallized as that grown on Ru(0001). Based on the band gap modulation of $MoSe_2$/*h*-BN/Ru(0001), here, we raise an unexplored question: can the band gap of *h*-BN exhibit periodic modulation following the moiré patterns? Thus, in line with this, we explored the tunability of the electronic properties of *h*-BN/Cu(111) by studying the local work function and the band gap modulations.

Several theoretical approaches have aided the study of unique heterostructures. The linear augmented plane wave plus local orbital (LAPW+LO) method was used to investigate the forces acting on B and N atoms with the focus on the $B_{fcc}N_{top}$ geometry. Furthermore, the density functional theory implemented in the Gaussian plane wave formalism was performed to study the variation in the electronic properties induced by moiré patterns [89]. However, these localized basis sets may not well describe the characteristics of transition metals, yielding an average *h*-BN–Cu separation of 3.0 Å [94], which is notably smaller than the experimental value of 3.24–3.38 Å. Moreover, the calculated work function values of 3.64–3.77 [89] and 3.64–3.78 eV [94] are much smaller than the experimental values. Therefore, the plane wave expansion of the wave functions seems to be needed for this system.

We performed theoretical calculations by using VASP [62, 63] with the PAW method [9, 10]. The SC consists of $\sqrt{139} \times \sqrt{139}$ *h*-BN on $\sqrt{133} \times \sqrt{133}$ with a twist angle of 4.75° and forms a 2.96-nm moiré pattern. The slab contains three layers of Cu atoms and a vacuum region of approximately 15 Å. We used a plane wave cutoff energy of 400 eV and sampled only the Γ point. The optB86b functional, including vdW correction, was adopted for structural relaxation. The structure was fully relaxed until the force on each atom was $<$0.01 eV/Å.

Because various orientations and periodicities of moiré patterns were observed in this weakly interacting system, we adopted the formula for the relationship between the moiré

pattern wavelengths (λ) and twist angles (ϕ) between the *h*-BN and Cu(111) surface.

$$\lambda = \frac{(1+\delta)a}{\sqrt{2(1+\delta)(1-\cos\phi)+\delta^2}}\,, \tag{4.1}$$

where a is the lattice constant of *h*-BN and δ is the lattice mismatch between *h*-BN and Cu(111). The maximal wavelength arises at twist angle of 0°. By substituting the experimental lattice constants of bulk *h*-BN and Cu(111), we noted that the resulting maximal wavelength of the moiré pattern (12.3 nm) remains smaller than the value reported in Ref. [93]. However, if the lattice constant of *h*-BN is slightly stretched to 2.51 Å, then delta becomes approximately 1.8%, with the largest moiré pattern becoming approximately 13.9 nm—close to the largest moiré wavelength found in the current experiments. This might be due to the differences in the lattice constants of single-layer and bulk *h*-BN. Another possibility is that *h*-BN expands as the temperature decreases. Moiré models, shown in Figure 4.6, is constructed by overlaying two grids with a hexagonal pattern representing the Cu(111) lattice and a honeycomb pattern representing the slightly stretched *h*-BN overlayer. The moiré wavelength and moiré rotation angle as functions of twist angle between *h*-BN and Cu(111) lattices are presented in Figure 4.7. When the twist angle between *h*-BN and Cu(111) decreases from 30° to 0°, the calculated wavelength of the moiré pattern increases from 0.5 to 13.9 nm, among which the largest moiré pattern corresponds to a 56×56 *h*-BN/55×55 Cu(111). To understand the formation and effects of moiré patterns, we developed a theoretical model, in which a SC commensurate with both *h*-BN and a metal surface was constructed.

However, calculating such a large SC by using plane waves is challenging. To verify the weak coupling between *h*-BN and Cu(111) and the number of Cu layers necessary to meet the convergence criterion, we performed calculations on a smaller SC, which is $2\sqrt{7}\times2\sqrt{7}$ *h*-BN/$3\sqrt{3}\times3\sqrt{3}$ Cu(111)R30° with an SC size of approximately 1.3 nm (Figure 4.8(a)). The results demonstrated that although the absolute binding energy of *h*-BN on Cu with the

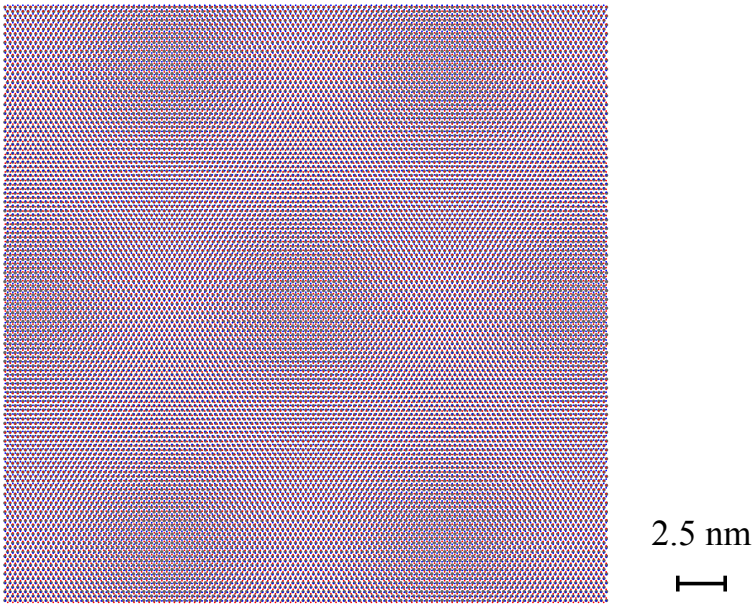

Figure 4.6: The calculated *h*-BN atomic structure of the 13.9-nm moiré pattern with the twist angle of 0° between stretched *h*-BN and Cu(111).

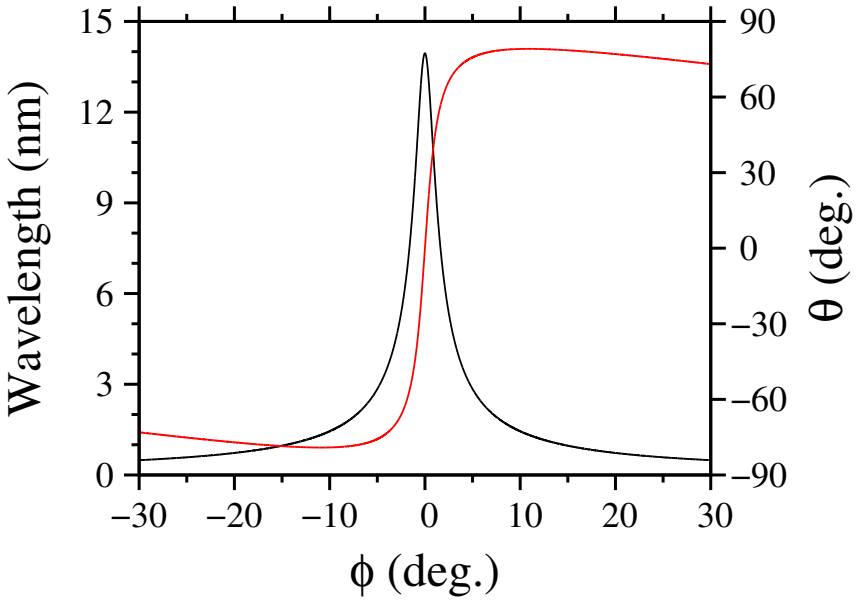

Figure 4.7: Wavelengths (black) and rotations (red) of the moiré patterns as a function of the twist angles between the stretched *h*-BN and Cu(111) lattices.

PBE exchange-correlation functional is only a few millielectronvolt per BN, the value obtained with the vdW Density Functional, optB86b-vdW-DF [24, 25, 26], is about hundreds of millielectronvolt per BN, with being approximately 0.06 eV/BN lower than that obtained with local density approximation. This result is consistent with an improved description of physisorbed behavior with vdW interactions in the vdW-DF. Both the binding energy and interlayer distance imply that *h*-BN and Cu(111) interact weakly, which allows for various arrangements of the *h*-BN layer grown on top of Cu(111) with different orientations and periodicities.

To study the twist angle dependency of the band gap modulation, we performed first-principles calculations on the electronic properties of another possible configuration of the *h*-BN/Cu(111) SC. Shown in Figure 4.8(b) is the SC containing $\sqrt{139} \times \sqrt{139}$ *h*-BN/$\sqrt{133} \times \sqrt{133}$ Cu(111), used to model a 2.96-nm moiré pattern with a twist angle of 4.75°. The results indicated that the average height of the *h*-BN layer above the Cu surface from our SC calculation is 3.21 Å, in agreement with the values of 3.24 Å [95] and 3.38 Å [92] obtained from the X-ray standing wave experiments. From the top view, regions with N atoms on the top, hcp, and fcc sites with respect to the underlying Cu substrate can be identified from left to right along the full diagonal, as indicated by the orange, blue, and black circles, respectively. According to the same convention used in *h*-BN/Ru, these regions are labeled as $B_{fcc}N_{top}$, $B_{top}N_{hcp}$ and $B_{hcp}N_{fcc}$, respectively. From the side view, the relaxed *h*-BN layer is almost but not perfectly flat and has a corrugation with the $B_{fcc}N_{top}$ region lower than the other by approximately 0.3 Å. Our relaxation result confirmed that the $B_{fcc}N_{top}$ region corresponds with the center of the holes, whereas the other two correspond with the wire; the holes and wires are typically referred to as the dark and bright regions in STM images, respectively.

For the electronic properties, the PDOS (Figure 4.9) indicated that the CB edge derives primarily from the p orbitals of B atoms and the VB edge from the p orbitals of N atoms. The CB edge projected to the $B_{fcc}N_{top}$ region, indicated using the orange dashed

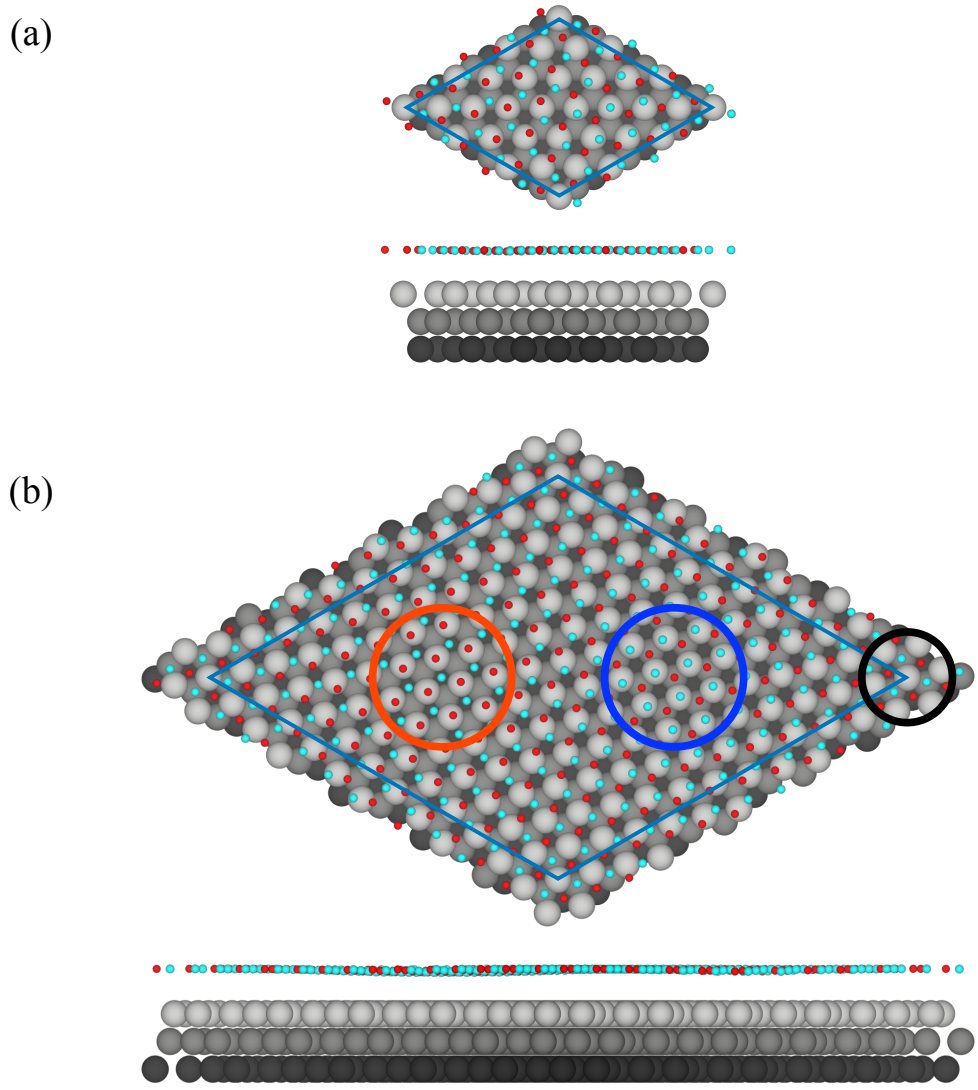

Figure 4.8: Top view and side view of the (a) $2\sqrt{7}\times2\sqrt{7}$ *h*-BN on $3\sqrt{3}\times3\sqrt{3}$ Cu(111) and (b) $\sqrt{139}\times\sqrt{139}$ *h*-BN on $\sqrt{133}\times\sqrt{133}$ Cu(111) structures that we used as theoretical models for the 1.3-nm and 2.96-nm moiré patterns. The red and light blue spheres represent N and B atoms, respectively. The first, second, and third layer of Cu atoms are illustrated by gray spheres with different darkness. High symmetric regions of $B_{fcc}N_{top}$, $B_{top}N_{hcp}$, and $B_{hcp}N_{fcc}$ are marked by orange, blue, and black circles, respectively.

line, shifts downward by approximately 0.4 eV (marked by a vertical orange arrow) for $\sqrt{139} \times \sqrt{139}$ *h*-BN on $\sqrt{133} \times \sqrt{133}$ Cu(111), whereas the CB edge shifts downward by a negligible value of 0.007 eV for $2\sqrt{7}\times2\sqrt{7}$ *h*-BN on $3\sqrt{3}\times3\sqrt{3}$ Cu(111). Simultaneously, at the $B_{fcc}N_{top}$ site, the projected N states demonstrate an additional small peak near the VB edge for both large and small moiré patterns, leading to a higher VB edge than that in $B_{top}N_{hcp}$ and $B_{hcp}N_{fcc}$. This small peak near the VBM in the hole region ($B_{fcc}N_{top}$) may be detected in tunneling measurements through its stronger coupling with the Cu orbitals in this geometry. Thus, the band edges, marked using the two orange arrows, indicate a band gap narrowing in the hole region compared with the other two regions; this agrees well with the experimental results. For the moiré pattern dependency behavior, CB edge shift increases as the moiré becomes larger, whereas the VB edge remains unchanged. This qualitatively explains the trends observed for the band edge shift in the experiment presented in Ref. [93]: (1) the positive correlation between the energy shift of the CB edge with the moiré wavelength, and (2) the constant shift of the VB edge, independent of the moiré wavelength. A possible reason for this independency is the dominating N–Cu interaction. In the wire region where the N atoms are away from the top sites, the hybridization is weak, and no new state is formed near the VB edge. However, in the hole region, N atoms, located directly above Cu atoms, exhibit the strongest orbital interaction with the metal orbitals, forming additional features just above the VB edge and thus inducing a spatial modulation of the VB edge. The calculated spatial modulation of the VB edge is approximately 0.4 eV—consistent with the experimentally measured VB edge modulation (0.2–0.3 eV).

We next discuss the twist angle dependency of the work function modulation within the moiré pattern. Our theoretical results (Figure 4.10) indicated a larger work function modulation in the 2.96-nm moiré pattern than in the 1.3-nm moiré pattern; however, the magnitude of the modulation remains negligible ($<$0.1 eV). This result agrees with the experimental result that only a weak modulation amplitude of 0.06 eV is noted for moiré

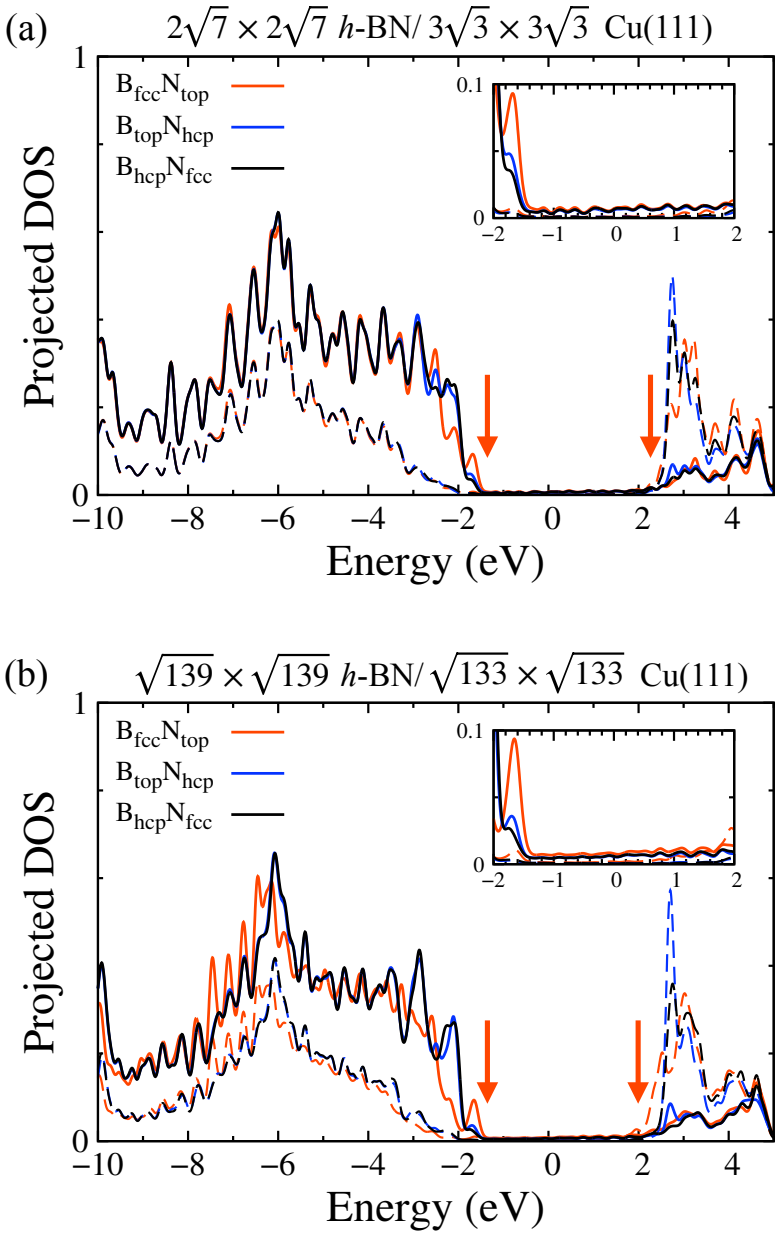

Figure 4.9: Calculated PDOS of (a) $2\sqrt{7}\times2\sqrt{7}$ h-BN on $3\sqrt{3}\times3\sqrt{3}$ Cu(111) and (b) $\sqrt{139} \times \sqrt{139}$ h-BN on $\sqrt{133} \times \sqrt{133}$ Cu(111) structures on the p orbitals of B atoms (dashed lines) and N atoms (solid lines) in $B_{fcc}N_{top}$, $B_{top}N_{hcp}$, and $B_{hcp}N_{fcc}$ regions. The zero energy was set at the Fermi level. While the conduction band edge derives primarily from the p-orbitals of B atoms, the valence band edge derives mostly from the p-orbitals of N atoms. Note, there exist an overall VB down-shift by about 0.4 eV in both (a) and (b). The orange vertical arrows indicate the band edges of the h-BN layer.

pattern with a wavelength of 3.5 nm. However, first-principles calculations by using plane waves on the SC with a moiré pattern wavelength of >3 nm remains technically difficult. To calculate the local work function modulation, a modified approach was adopted by building periodic unit cells representing local structures of the moiré pattern, in which we could perform accurate calculations on the local electronic properties. BZ sampling was performed using a $15\times15\times1$ MonkhorstPack grid for both structural relaxation and static calculations [96]. Electronic optimization was performed with a tolerance of 10^{-5} eV. Differential charge density is defined as $\rho = \rho_{h\text{-BN/Cu}} - \rho_{h\text{-BN}} - \rho_{\text{Cu}}$, where $\rho_{h\text{-BN/Cu}}$, $\rho_{h\text{-BN}}$, and ρ_{Cu} represent the charge density of the *h*-BN/Cu system, single *h*-BN sheet, and Cu substrate, respectively. Because the 1×1 unit cell is created based on the local structure of the moiré pattern with a small strain, it can capture the local electronic properties for different stacking configurations [97]. As indicated, in the hole center, the N atom is located on top of the surface Cu atom, forming a $B_{fcc}N_{top}$ structure (Figure 4.11(a)). Here, the strongest bonding originates from the hybridization of the $3p_z$ orbital of N and $4s$ orbital of Cu. It can form a relatively strong bond and lead to the strongest charge transfer (Figure 4.12). Furthermore, new components induced by the *h*-BN–Cu hybridization can lead to a narrower band gap. By contrast, B and N atoms have various configurations in the wire region. Two possibilities are demonstrated in Figure 4.11(b) with a $B_{top}N_{hcp}$ structure, where N atoms are situated above the Cu hcp sites, and Figure 4.11(c) with a $B_{hcp}N_{fcc}$ structure, where N atoms are located above the Cu fcc sites. In this case, the hybridization is relatively weak, and all the electronic properties of this type of BN structures should be less perturbed by the presence of Cu and be closer to the pristine *h*-BN. As shown in Figure 4.13, the plane-averaged Hartree potential along the vertical direction indicated that the work function in the $B_{fcc}N_{top}$ region is approximately 0.3 eV lower than that in the $B_{top}N_{hcp}$ and $B_{hcp}N_{fcc}$ region. This modified 1×1 unit cell approach is presumably valid for moiré patterns with large periodicities because the local structures can extend to a larger area. Our calculations indicated a local work function difference of approximately 0.3 eV

between the hole and wire regions, in agreement with the values previously obtained using 1×1 unit cells [89, 92]. This 1×1 approach also yields a band gap difference of approximately 0.5 eV between$B_{fcc}N_{top}$ and $B_{hcp}N_{fcc}$ structures. In comparison, the SC and unit cell approaches have their own limitations: the SC is valid in short wavelength ($\leq$3 nm) regimes, whereas the unit cell is applicable for only long wavelength limits. Combining results for both the limits, we concluded that the work function modulation is negligible at short wavelength and it becomes more substantial at long wavelengths—consistent with the experimental observations.

In summary, we systematically investigated the moiré pattern wavelength-dependent work function and band gap modulations in *h*-BN/Cu(111) heterostructures. When the Cu(111) surface is covered with *h*-BN because of the induced dipole layer, the average work function of the system decreases compared with the bare Cu(111) surface. Furthermore, we noted a spatial modulation of the local work function with amplitudes ranging from 0.3 eV for a 14-nm wavelength to a negligible value for a 3.5-nm wavelength, all attributable to the variation in the dipole layer. The strongest hybridization of N $3p_z$ and Cu $4s$ orbitals exist in the region where N atoms are located on top of Cu atoms, whereas the weakest hybridization occurs in the wire region where N atoms are located between Cu atoms. Moreover, the wavelength dependency of the modulation amplitude is due to the local work function being determined by the electrostatic potential from a region in the order of nanometers. In addition, our results indicated that the band gap of the insulating *h*-BN atomic layer exhibits similar modulations. This occurs because the CBM and VBM of the system are mainly contributed by the p_z orbitals of B and N atoms, respectively. Furthermore, the band gap modulation of *h*-BN can be affected by the moiré pattern wavelength. In general, our results provide microscopic understanding of moiré pattern formation and explain the mechanism underlying work function shift in the *h*-BN/Cu(111) heterostructure. The results also confirm the role of the moiré pattern wavelength in tuning the electronic properties. We noted that the tunability of the band gap and local work

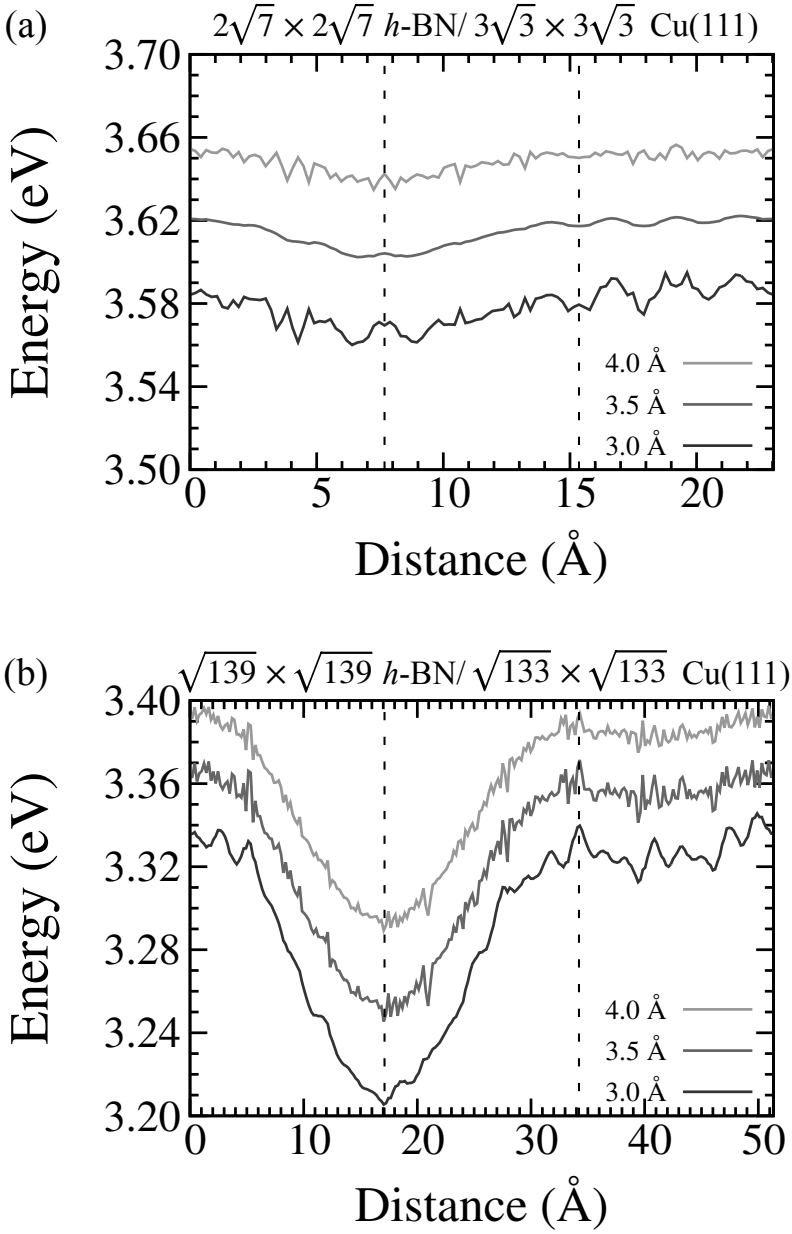

Figure 4.10: Calculated hartree potential along the main diagonal of the supercell of (a) $2\sqrt{7}\times2\sqrt{7}$ h-BN/$3\sqrt{3}\times3\sqrt{3}$ Cu(111) and (b) $\sqrt{139}\times\sqrt{139}$ h-BN/$\sqrt{133}\times\sqrt{133}$ Cu(111) at the height of 3 Å, 3.5 Å, and 4 Å above the h-BN layer. The black dashed lines label the position of one-third and two-thirds length of the diagonal, respectively.

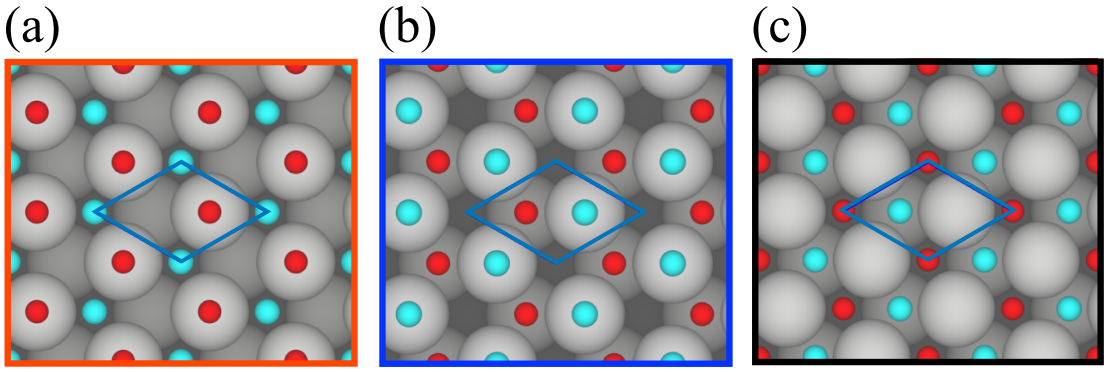

Figure 4.11: Top view of the 1×1 *h*-BN on 1×1 Cu(111) structures for (a) $B_{fcc}N_{top}$, (b) $B_{top}N_{hcp}$, and (c) $B_{hcp}N_{fcc}$ used in the unit cell approach.

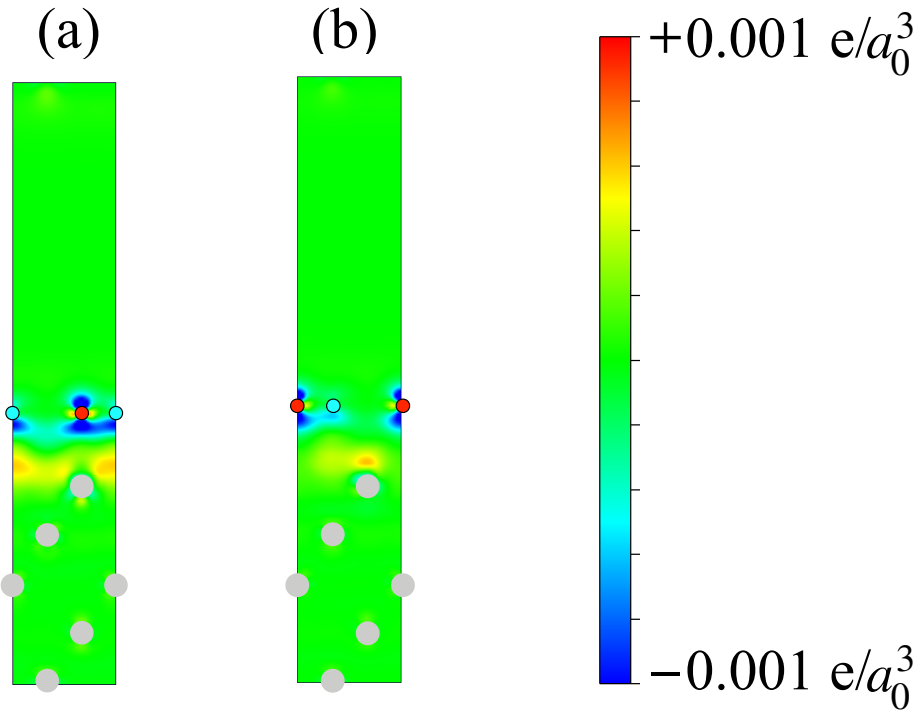

Figure 4.12: Slice of charge transfer between the *h*-BN and Cu(111) from the unit cell model of (a) $B_{fcc}N_{top}$ and (b) $B_{hcp}N_{fcc}$, respectively. The charge transfer unit is e/a_0^3, where a_0 is the Bohr radius. B and N atoms are labeled by light blue and red spheres with black line borders, while Cu atoms are labeled by gray spheres.

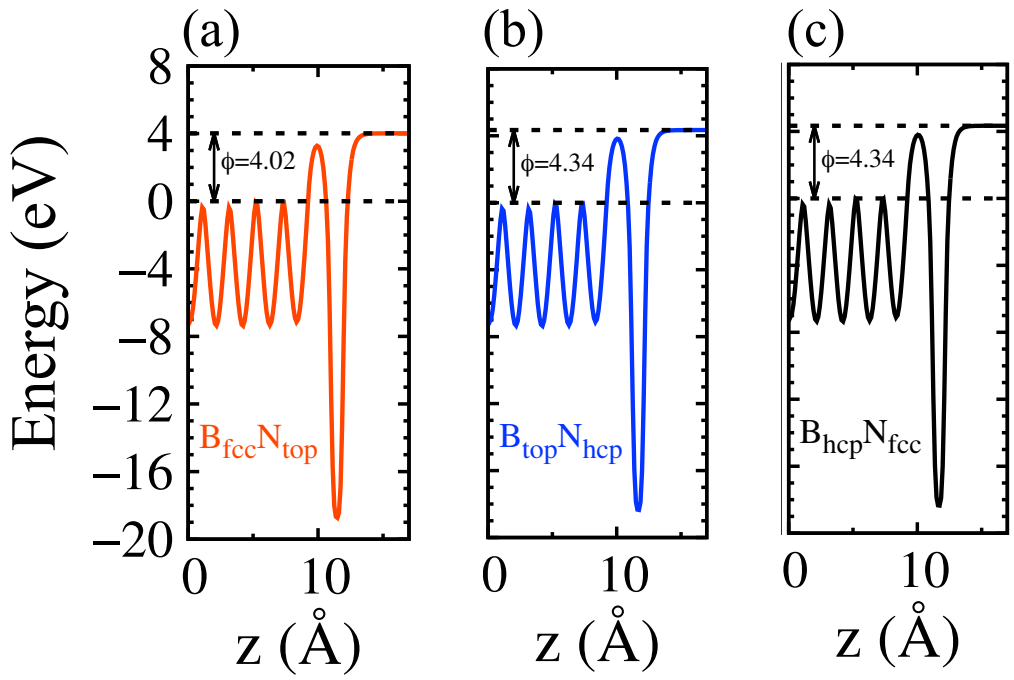

Figure 4.13: Calculated plane-averaged hartree potential along the direction perpendicular to the surface for (a) $B_{fcc}N_{top}$, (b) $B_{top}N_{hcp}$, and (c) $B_{hcp}N_{fcc}$. The energy differences between the dashed lines define the work function. The Fermi level was set at zero.

function of *h*-BN can be achieved by suitably adjusting the twist angle of moiré patterns. These results may be helpful in studying and optimizing the electronic properties of a wide variety of 2D materials exhibiting moiré patterns for future applications.

CHAPTER 5

ELECTRONIC PROPERTIES OF LEAD/SILVER STACKED METALLIC THIN FILMS

The fabrication of thin film structures with few-atom thickness has been widely adopted and studied over the last two decades because of the increasing need of high-performance and high-efficiency electronic devices. Compared with bulk materials, thin films have a restricted extent in one dimension, such that the electron motion is confined between two planes, which can be film–substrate or film–vacuum interfaces. The allowed crystal momentum with the direction perpendicular to these interfaces is discrete, resulting in the so-called QWSs, which have substantial effects on the electronic properties of nanostructures. The earliest theoretical study regarding the effect of QWSs on the work function was conducted in the 1970s [98]. Currently, QWS continues to gain attention, particularly with the availability of large, smooth, and high-quality thin films and the discovery of the modulated physical and chemical properties as a function of layer thickness, including the thermal stability [99, 100, 101, 102, 103, 104], critical superconductivity temperature [105, 106, 107], and work function [108, 109, 110]. A wealth of these oscillating phenomena can be explained through the modulation of the density of states near the Fermi level. Because of the short wavelength of electron waves, electron interference is very sensitive to film thickness and smoothness, which is a characteristic that can be used to monitor the growth of thin films. A recent study [111] presented the results of ARPES for Pb/Ag bimetallic thin films on the Si(111) substrate, in which the electronic states and their charge density distributions have not been completely understood. Here, we studied the electronic properties of these thin films, which can be directly compared with the ARPES data. In addition, we confirmed that the electronic coherence in the entire bimetallic film can be achieved by connecting QWSs in each metallic part with its own commensurate wavelength.

To investigate the electronic properties of Pb/Ag bimetallic thin films, we first constructed a slab in which 10 Pb(111) layers are stacked on 9 Ag(111) layers with both sides of the slab in contact with vacuum. The interlayer distance at the Pb–Ag interface was taken as the average of the Ag–Ag and Pb–Pb layer separations. The calculated lattice constants of Pb(111) and Ag(111) are $a_{\mathrm{Pb(111)}}$=3.56 Å and $a_{\mathrm{Ag(111)}}$=2.95 Å, respectively. For a rotationally aligned lattice, a 5×5 Pb(111) unit cell has a small lattice mismatch with 6×6 Ag(111). To construct a lattice-matched SC with a minimal strain level for Pb and Ag, we selected the average lattice constants, L $=(5\times a_{\mathrm{Pb(111)}}+6\times a_{\mathrm{Ag(111)}})/2$, such that the strain levels (ϵ) are -0.3% and 0.3% for Pb and Ag, respectively. The strain level is defined as

$$\epsilon = \frac{\mathrm{L} - \mathrm{m} \times a_{\mathrm{Pb/Ag(111)}}}{\mathrm{m} \times a_{\mathrm{Pb/Ag(111)}}} \times 100\%, \ \ \mathrm{m} = 5\,(6) \text{ for Pb (Ag).} \tag{5.1}$$

However, in the real situation, the Pb/Ag bimetallic thin film is laid on top of a Si(111) substrate. To examine how the Si substrate affects the electronic properties of a thin film, another smaller SC with a reasonable strain level should be searched for, such that the calculation of a slab containing Pb/Ag/Si is feasible. Therefore, a SC with 3×3 Pb(111) on $\sqrt{13} \times \sqrt{13}$ Ag(111)R13.9° was selected with a slightly changed strain levels of approximately -0.2% and 0.2% for Pb and Ag, respectively. Moreover, $\sqrt{13} \times \sqrt{13}$ Ag(111) is approximately commensurate with $\sqrt{7} \times \sqrt{7}$ Si(111)R19.1°. Therefore, using this model is convenient for studying the Si substrate effect on the electronic properties of Pb/Ag bimetallic thin films.

The calculations are based on DFT as implemented in the VASP [62, 63] computation code, which adopts the plane wave basis. We set the plane wave energy cutoff at 500 eV in this study. The PBE form was used for the exchange-correlation functional, and the PAW method for pseudopotentials was employed. We used the Monkhorst-Pack scheme for the $\boldsymbol{k}$-point mesh, which is 3×3×1 for the structures with 3×3 Pb(111) unit cells and 2×2×1 for the structures with 5×5 Pb(111) unit cells. The slab contains 10, 9, and 6 layers

of Pb, Ag, and Si, respectively, in which the vacuum regions are 26 and 15 Å for Pb/Ag and Pb/Ag/Si, respectively. The bottom layer of Si is passivated by H. The structure was constructed using the calculated bulk geometries. To handle the large-scale calculations, the ionic relaxation was ignored, and the electronic wavefunctions were completely optimized until the energy difference between the adjacent steps was $<10^{-4}$ eV. The energy band unfolding was performed using the BandUP code [112, 113]. In total, 100 $\boldsymbol{k}$ points were used to sample the unfolding path along $\bar{\mathrm{M}}$–$\bar{\Gamma}$–$\bar{\mathrm{K}}$. The energy resolution was sampled in a discrete value of 0.01 eV.

Although the SC model reduces the impact caused by the strain in two metals, the band structure becoming complex as the states fold into a very small SC BZ (sBZ) is a limitation (small black hexagons in Figure 5.1). To straightforwardly compare our results to the ARPES data and sort the relevant states near the $\bar{\Gamma}$ point, the states carrying components of $\exp(i\mathbf{G}\cdot\mathbf{r})$ in the SC band structure should be unfolded onto the primitive BZ (pBZ) according to $\mathbf{k} = \mathbf{K} + \mathbf{G}$, where $\mathbf{k}$ and $\mathbf{K}$ are the wave vectors of states in the primitive cell and SC, respectively, and $\mathbf{G}$ the reciprocal lattice vector of the SC. In our case, two inherent periodicities in the SC, each corresponding to Ag(111) and Pb(111) lattices, were noted. Therefore, the band unfolding results depend on which lattice the unfolding is with respect to. The details of the unfolding method have been introduced in Section 2.5.

The electronic band structures calculated for pure metallic thin films are presented in Figure 5.2. QWSs manifest themselves as the discrete energy levels around the $\bar{\Gamma}$ point near the Fermi level. Their partial charge densities at the $\bar{\Gamma}$ point, displayed in Figure 5.3, demonstrate the modulation of the charge density deep in the thin film. For the 9-layer Ag film, the dispersion is characterized by a large slope as it moves away from the $\bar{\Gamma}$ point, which is dominated by s orbitals, except for the surface states above the Fermi level, which mainly project on p_z orbitals. In addition, p_x and p_y orbitals are the predominant components of the states near the BZ boundary, and d orbitals mostly lie in the flat bands in the range of $-4\leq \mathrm{E}-\mathrm{E_F}\leq -3$ eV. For the 10-layer Pb film, the bands near the Fermi level are

relatively flat, particularly for the three bands within $0 \leq E - E_F \leq 2$ eV. These states, along with the states with parabolic dispersion in the lower energy, have major p_z characteristics. The states with quite large but negative dispersion away from the BZ center are dominated by p_x and p_y orbitals. Moreover, the constant-energy contours at $E_F - 1.0$ eV are relatively different for the two films (right panels of Figure 5.2). If these two films are stacked together to form a new thin film, the boundary condition will be changed at the interface between them. The QWS may experience a different phase shift at the boundary; this shift can change its eigenvalue. In the unfolded band structure of the bimetallic thin film of 3×3 Pb(111)/$\sqrt{13} \times \sqrt{13}$ Ag(111) (Figure 5.4), the number of states doubles in the energy range between -3 and 0 eV compared with that in the same energy range for pure Pb and Ag films. The energies of the states around the $\bar{\Gamma}$ point in the energy range between -3 and 0 eV, shown in Figure 5.4(a), are identical to those in Figure 5.4(b) but with different projection directions; this suggests that these states are relatively isotropic—an indication of free-electron like energy bands. Thus, if we were to plot the constant-energy contours, their shape would be circular. In addition, most of these states have the charge density distributed in both Pb and Ag parts of the film (Figure 5.5(a)). For these states, similarly, the charge densities are modulated by QWSs. The general characteristics of these QWSs are comparable to those of the states in both Ag and Pb pure thin films. However, as mentioned, different phase shifts occur when a film–vacuum interface is replaced with a film–film interface. Moreover, by connecting QWSs in each metallic film, the electronic coherence in the entire bimetallic film can be achieved.

In the experimental configuration, however, the bimetallic thin film is supported by the Si substrate. Therefore, we constructed a bimetallic structure with 3×3 Pb(111)/$\sqrt{13}\times\sqrt{13}$ Ag(111) laid on top of six $\sqrt{7} \times \sqrt{7}$ Si(111) layers. The unfolded band structure (Figure 5.6) demonstrates that the features mentioned previously, including the common states around the $\bar{\Gamma}$ point in the energy range of -3.0 to 0.0 eV and the isotropy of the dispersion, remain—irrespective of projection directions. Nevertheless, compared with the common

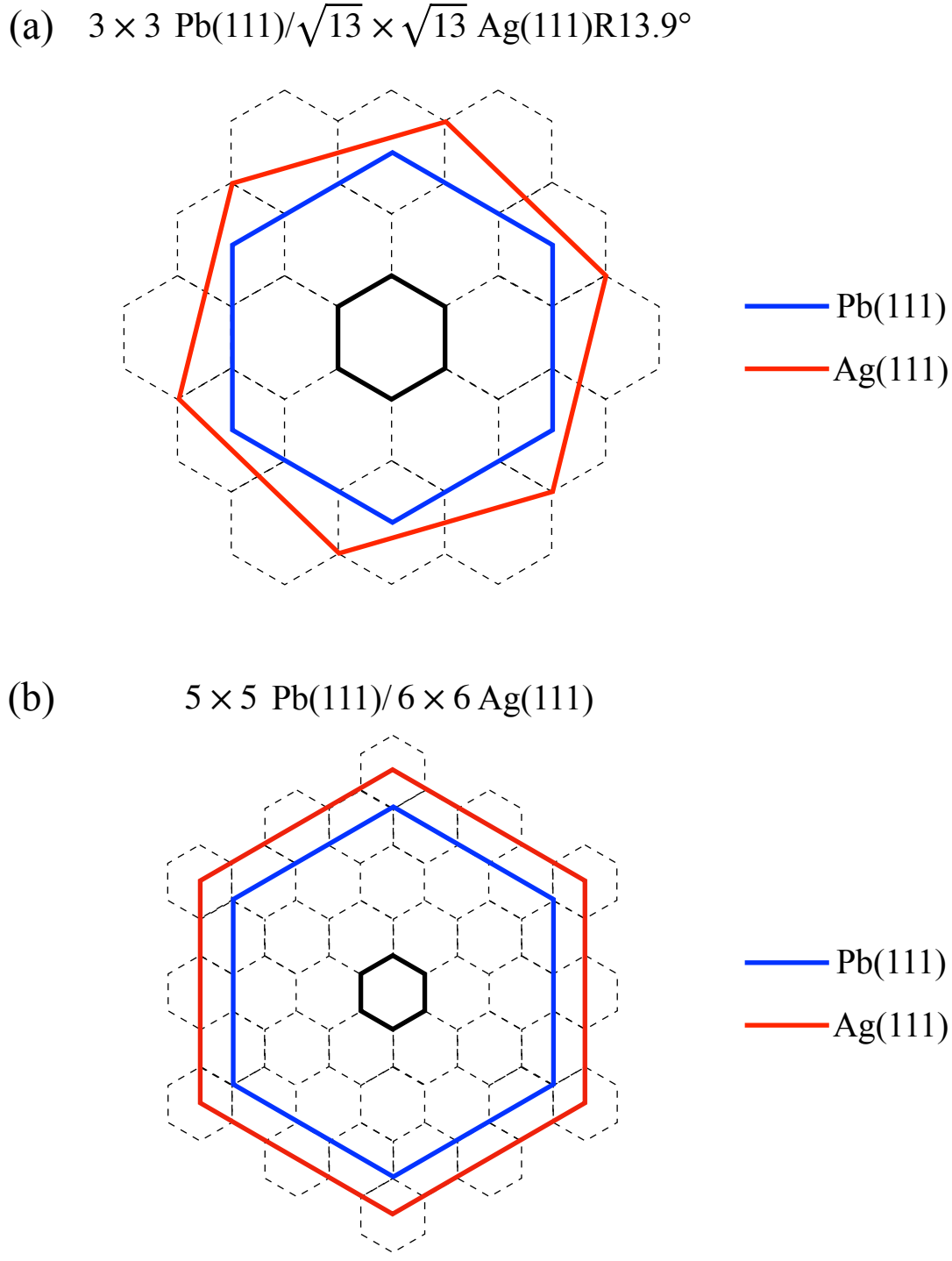

Figure 5.1: Relationship of BZs for (a) 3×3 Pb(111)/$\sqrt{13}\times\sqrt{13}$ Ag(111)R13.9° and (b) 5×5 Pb(111)/6×6 Ag(111). The BZs corresponding to the unit cells of 1×1 Pb(111) and 1×1 Ag(111) are represented by blue and red hexagons, respectively. The black hexagons are the BZ of the commensurate supercells.

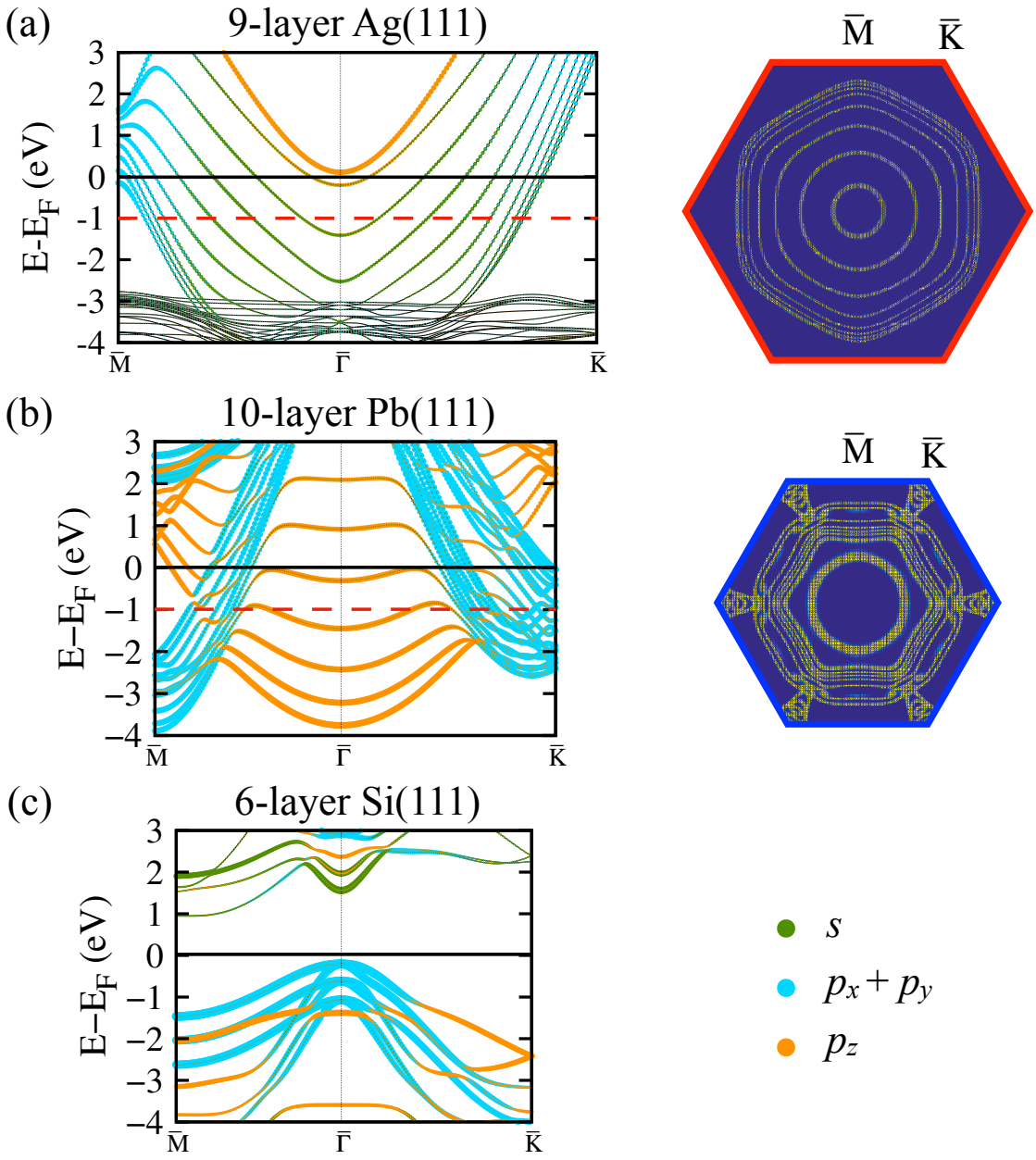

Figure 5.2: Calculated electronic band structures of the (a) 9-layer Ag(111), (b) 10-layer Pb(111), and (c) 6-layer Si(111) thin films where Si thin films are passivated by H on both sides. The wave vectors are in the BZ of their 1×1 unit cells. The contribution from s, $p_x + p_y$, and p_z states are labeled in green, light-blue, and orange circles, respectively, with the radii showing the projecting magnitude. The right panels show the constant-energy contours at 1.0 eV below the Fermi level, as indicated by the red dashed lines.

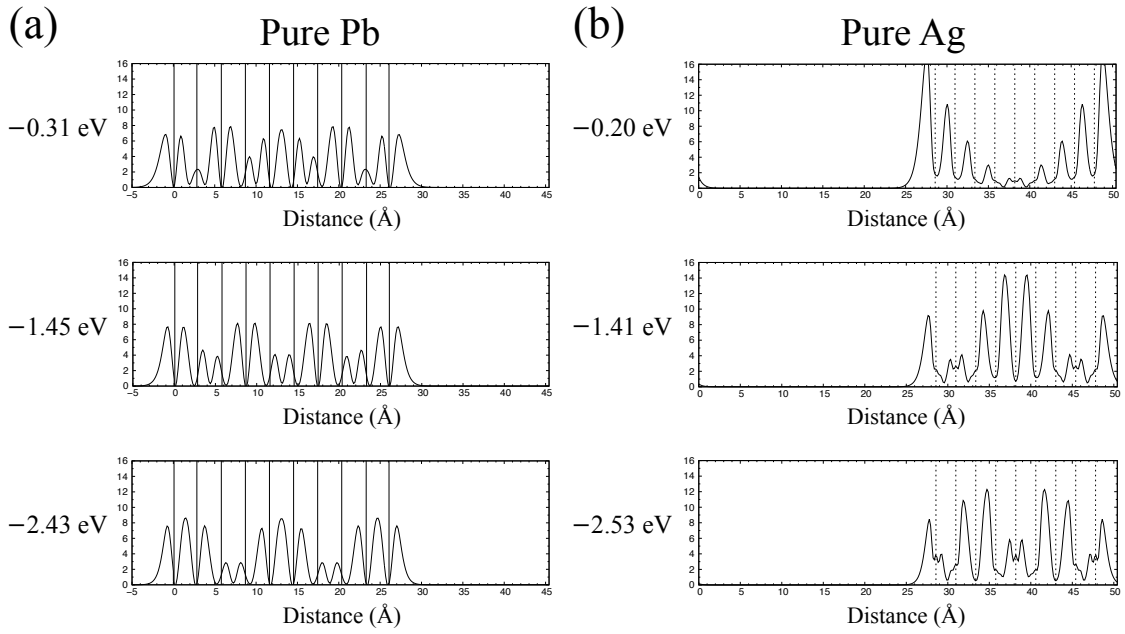

Figure 5.3: The partial charge densities of the three states below the Fermi level for (a) Pb and (b) Ag. The solid lines indicate the atomic Pb planes, while the dotted lines indicate those for Ag. The energies with respect to the Fermi level of these states are shown on the left of each panel.

states presented in Figure 5.4, those in Figure 5.6 have shifted to different energies. In particular, the fourth state counted from the top shifted by approximately 0.32 eV, which is the first state noted in the charge density plots of Figure 5.5. The energy difference is due to the change in the phase shift accumulated at the boundary of the vacuum and the Si substrate. However, Figure 5.5(b) indicates that the charge density distributions in the Pb/Ag part of 3×3 Pb(111)/$\sqrt{13} \times \sqrt{13}$ on Si(111) are quite similar to those presented in Figure 5.5(a). The only major difference is in the first state, which has shifted by 0.32 eV, in that a significant amount of charge has been transferred to the Si substrate. Figure 5.7 demonstrates the unfolded band structure with respect to the Si BZ, in which a series of Si states, obscure in Figure 5.6, are revealed. Because we used a finite Si slab in our calculations, discrete Si states were found and some coupling with the QWSs in the metallic film was noted. These discrete states are expected to become a continuum when the substrate is sufficiently thick.

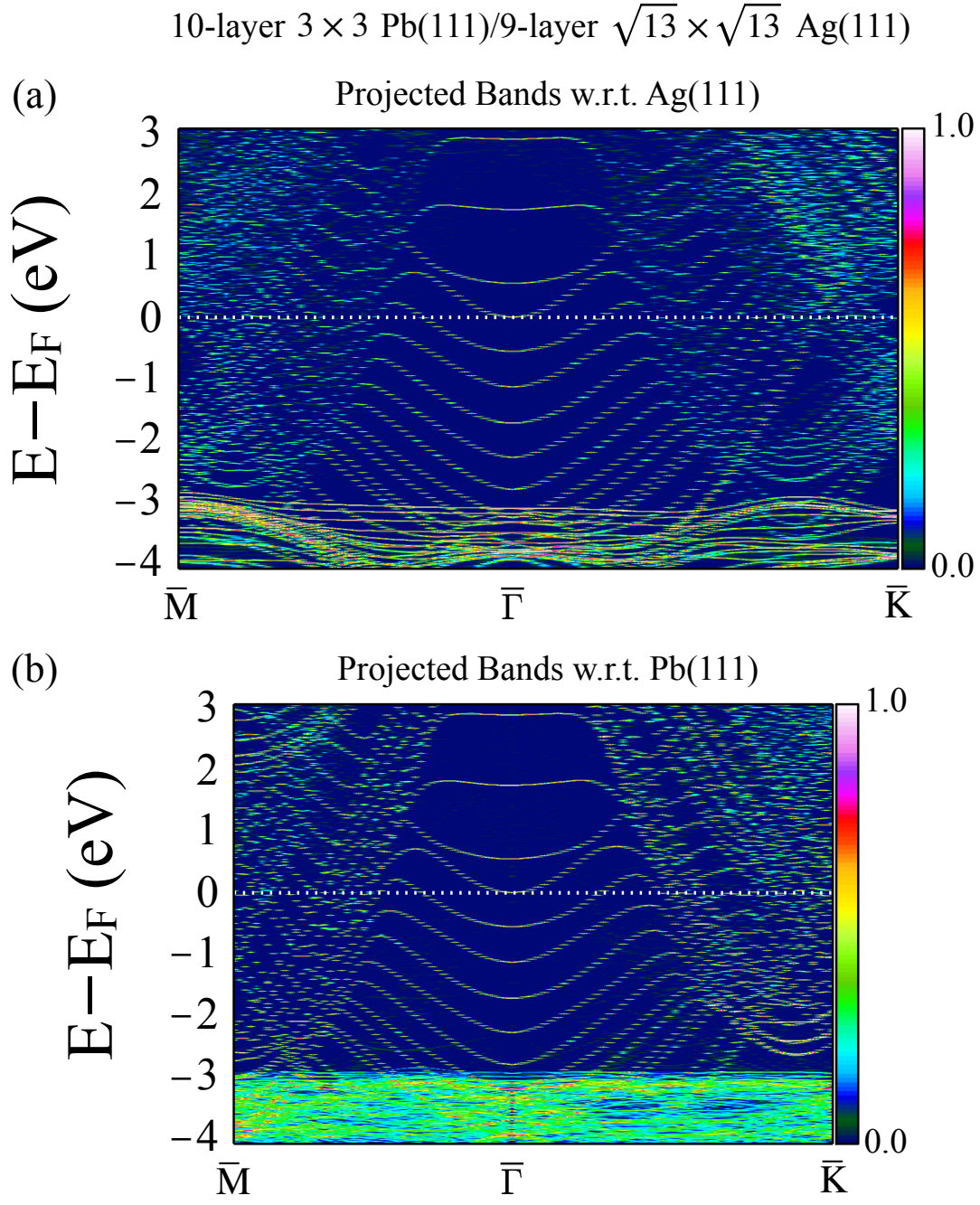

Figure 5.4: Calculated unfolded band structures of the 10-layer 3×3 Pb(111)/9-layer $\sqrt{13}\times\sqrt{13}$ Ag(111) bimetallic thin film with respect to the (a) Ag and (b) Pb lattices. $\bar{\text{M}}$ and $\bar{\text{K}}$ in (a) and (b) lie on the red and blue hexagons in Figure 5.1(a), respectively.

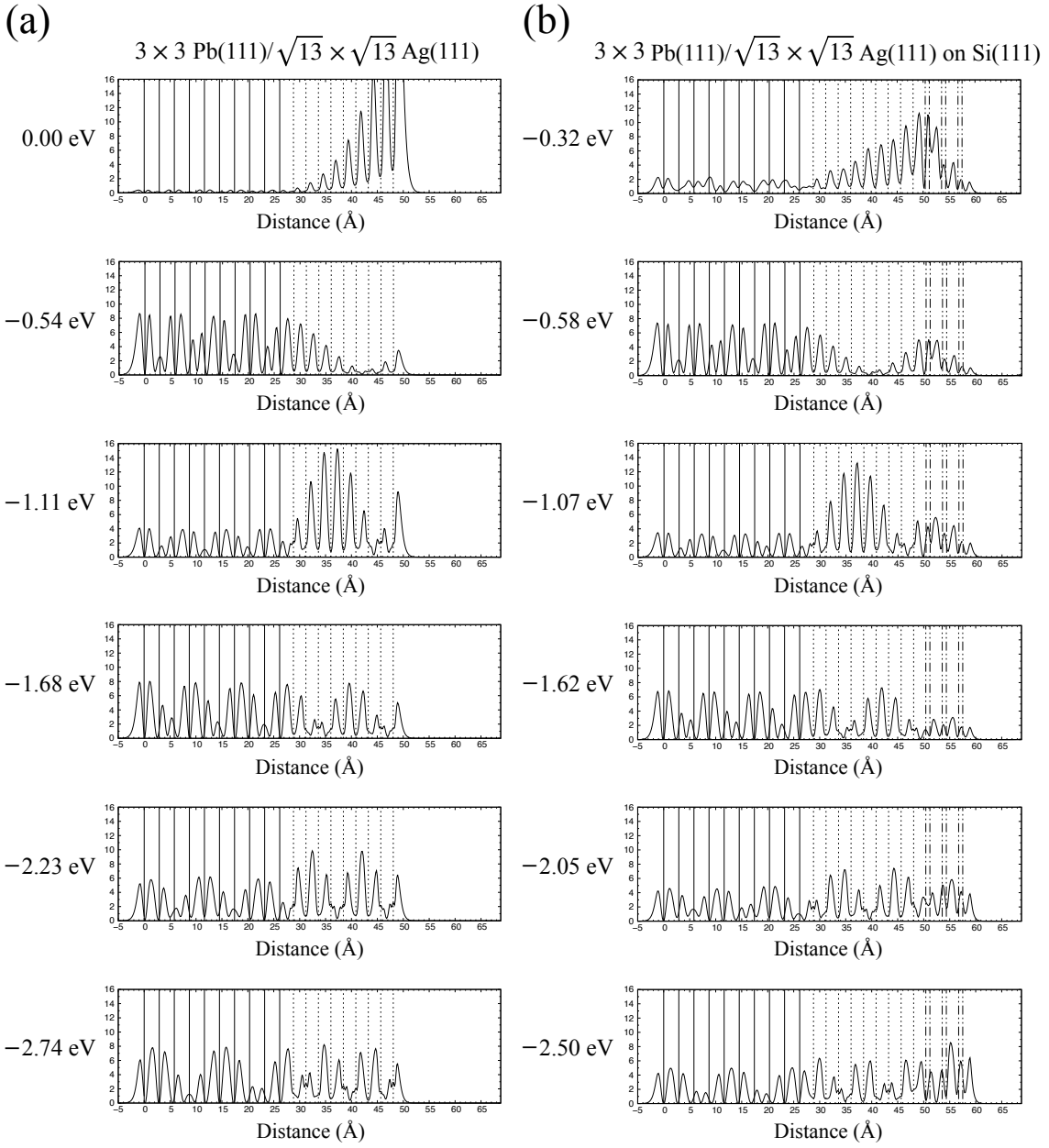

Figure 5.5: The xy-plane-averaged charge distributions along the normal direction of the thin film of the states at the $\bar{\Gamma}$ point for (a) 3×3 Pb(111)/$\sqrt{13}\times\sqrt{13}$ Ag(111) and (b) 3×3 Pb(111)/$\sqrt{13}\times\sqrt{13}$ Ag(111)/$\sqrt{7}\times\sqrt{7}$ Si(111). The energies with respect to the Fermi level of these states are shown on the left of each panel. The solid lines indicate the Pb planes, while the dotted lines label the Ag planes. The Si planes are shown by the dot-dashed lines in (b).

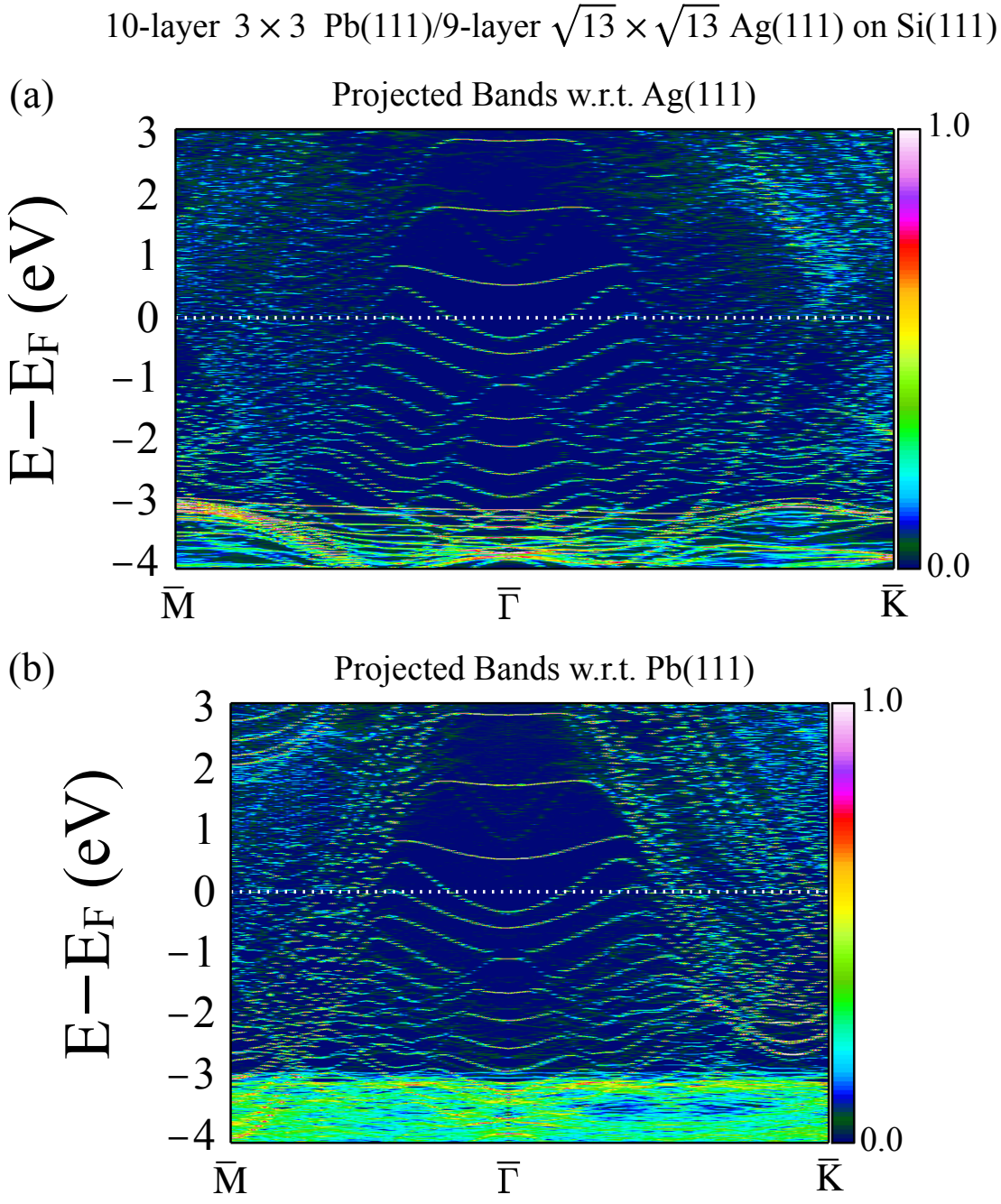

Figure 5.6: Calculated unfolded band structures of the 10-layer 3×3 Pb(111)/9-layer $\sqrt{13}\times\sqrt{13}$ Ag(111) bimetallic thin film on the 6-layer $\sqrt{7}\times\sqrt{7}$ Si(111) with respect to the (a) Ag and (b) Pb lattices. $\bar{\mathrm{M}}$ and $\bar{\mathrm{K}}$ in (a) and (b) lie on the red and blue hexagons in Figure 5.1(a), respectively.

Figure 5.8 compares the calculated energy bands near $\bar{\Gamma}$ in Figure 5.4 and Figure 5.7 with the ARPES results. It indicates that in the presence of the Si substrate, our calculated unfolded band structure agrees relatively well with the experimental results. Although their Fermi levels can be different, possibly because of the doping or fine details of the interface structure, the energy differences of the four QWSs nearest to the Fermi level are comparable to those in the ARPES data.

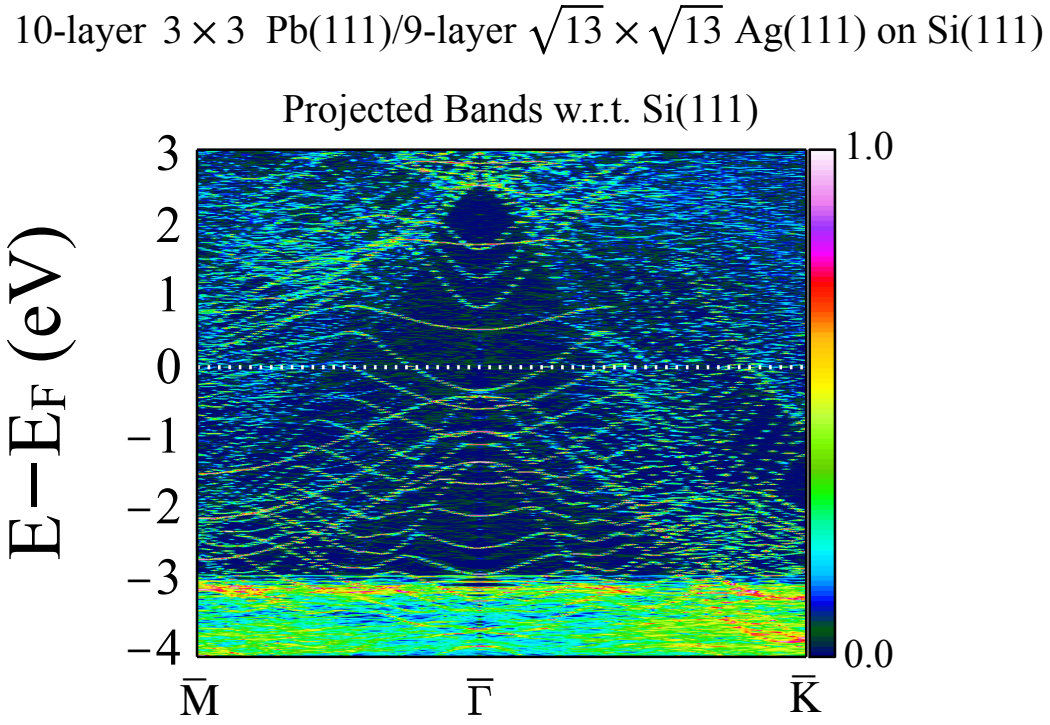

Figure 5.7: Calculated unfolded band structure of the 10-layer 3×3 Pb(111)/9-layer $\sqrt{13}\times\sqrt{13}$ Ag(111) bimetallic thin film on 6-layer $\sqrt{7}\times\sqrt{7}$ Si(111) with respect to the Si lattice.

Thus far, we have discussed results for a composite film, in which a relative rotation between Pb and Ag lattices was included for reducing the strain in both parts. Next, we investigate the effect of this rotation by performing a calculation on the bimetallic 5×5 Pb(111)/6×6 thin film. The unfolded band structure is presented in Figure 5.9, in which the states around $\bar{\Gamma}$ ranging from -3 to 0 eV have energies similar to those presented in Figure 5.4. This may be because they both have very small strain levels (0.3% vs 0.2%).

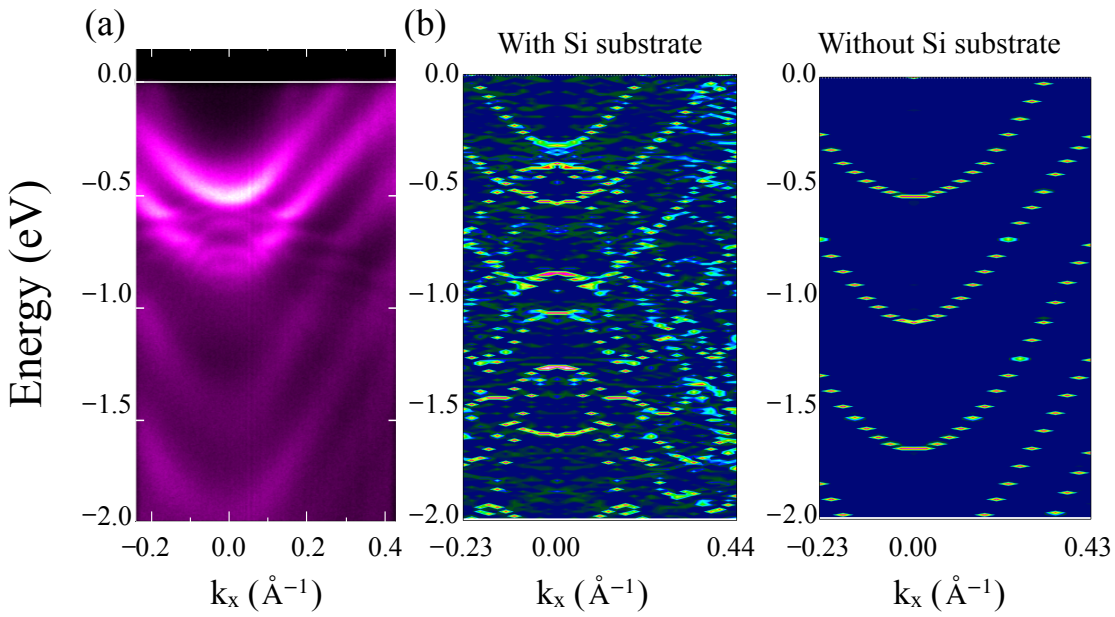

Figure 5.8: (a) The ARPES data of 10-layer Pb(111)/9-layer Ag(111) grown on Si(111). (b) The partial enlargement of Figure 5.7 (with Si substrate) and Figure 5.4(a) (without Si substrate) around the fermi level near $\bar{\Gamma}$ with k_x along the $\bar{\Gamma}\bar{K}$ direction.

Differences were noted only for wave vectors far from the $\bar{\Gamma}$ point but near the zone boundary. Furthermore, Figure 5.10 displays that the charge density is almost unchanged with respect to rotation. Thus, a slightly rotated structure with a reasonable strain is appropriate for studying QWSs of the bimetallic structure.

Finally, we examined the anisotropy of energy bands further from the $\bar{\Gamma}$ point. As indicated in Figure 5.9, starting from the $\bar{\Gamma}$ point, the constant-energy levels of $E_F-0.3$ and $E_F-0.7$ eV cut the band for the third time at the respective k points of 0.578 and 0.613 Å^{-1} along $\bar{\Gamma}\bar{K}$ and 0.494 and 0.515 Å^{-1} along $\bar{\Gamma}\bar{M}$—reflecting the features of the QWS dispersions in pure Pb thin films. However, the ratios of the intersecting k distances in the $\bar{\Gamma}\bar{K}$ direction to that in the $\bar{\Gamma}\bar{M}$ direction for $E_F-0.3$ and $E_F-0.7$ eV are 1.17 and 1.19, respectively—1.6% and 3.6% larger than that for a regular hexagon, respectively. Thus, the warping of energy contours in Figure 5.11 are confirmed: the first two contours close to the $\bar{\Gamma}$ point are circles and the third contour is a warped hexagon with edges inwardly concaved.

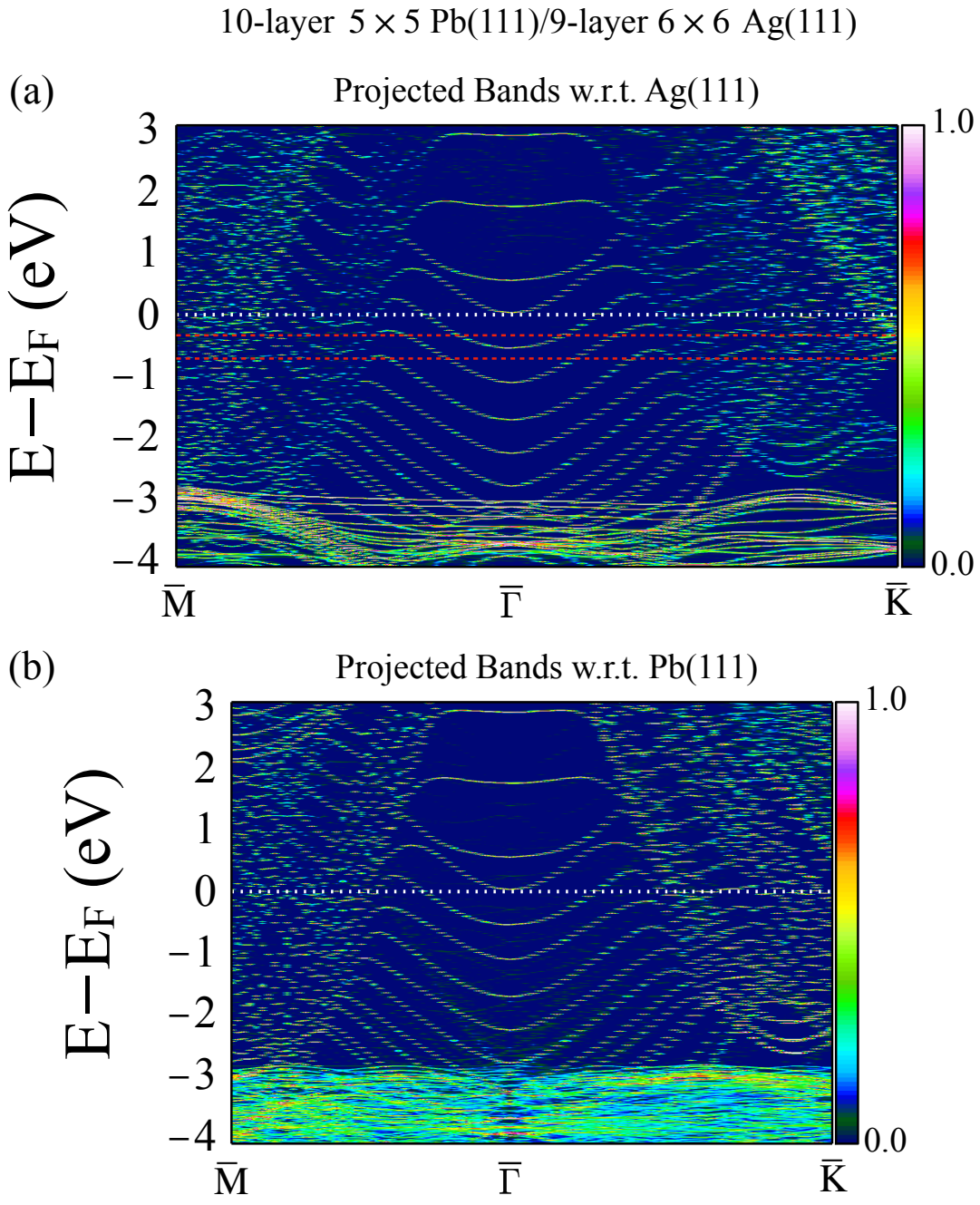

Figure 5.9: Calculated unfolded band structure of the 10-layer 5×5 Pb(111)/9-layer 6×6 Ag(111) bimetallic thin film with respect to (a) Ag and (b) Pb lattices along $\bar{M}$–$\bar{\Gamma}$–$\bar{K}$, where $\bar{M}$ and $\bar{K}$ in (a) and (b) lie on the red and blue hexagons in Figure 5.1(b), respectively. The red lines in (a) indicate the constant-energy levels at $E_F-0.3$ and $E_F-0.7$ eV.

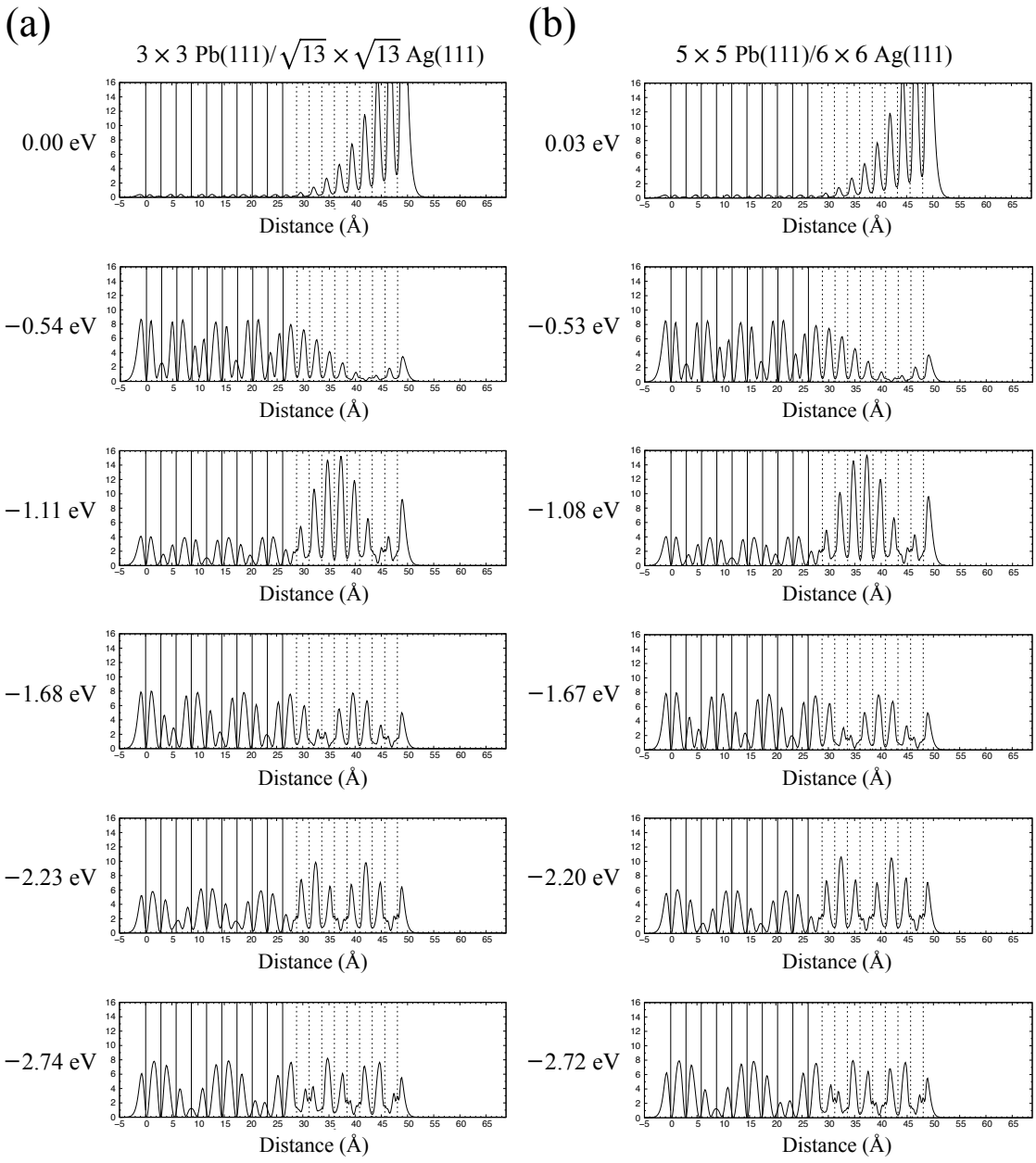

Figure 5.10: The xy-plane-averaged charge distributions along the normal direction of the thin film of the states at the $\bar{\Gamma}$ point for (a) 3×3 Pb(111)/$\sqrt{13} \times \sqrt{13}$ Ag(111) and (b) 5×5 Pb(111)/6×6 Ag(111) structures. The energies with respect to the Fermi level of these states are shown on the left of each panel. The solid lines indicate the Pb planes, while the dotted lines indicate the Ag planes.

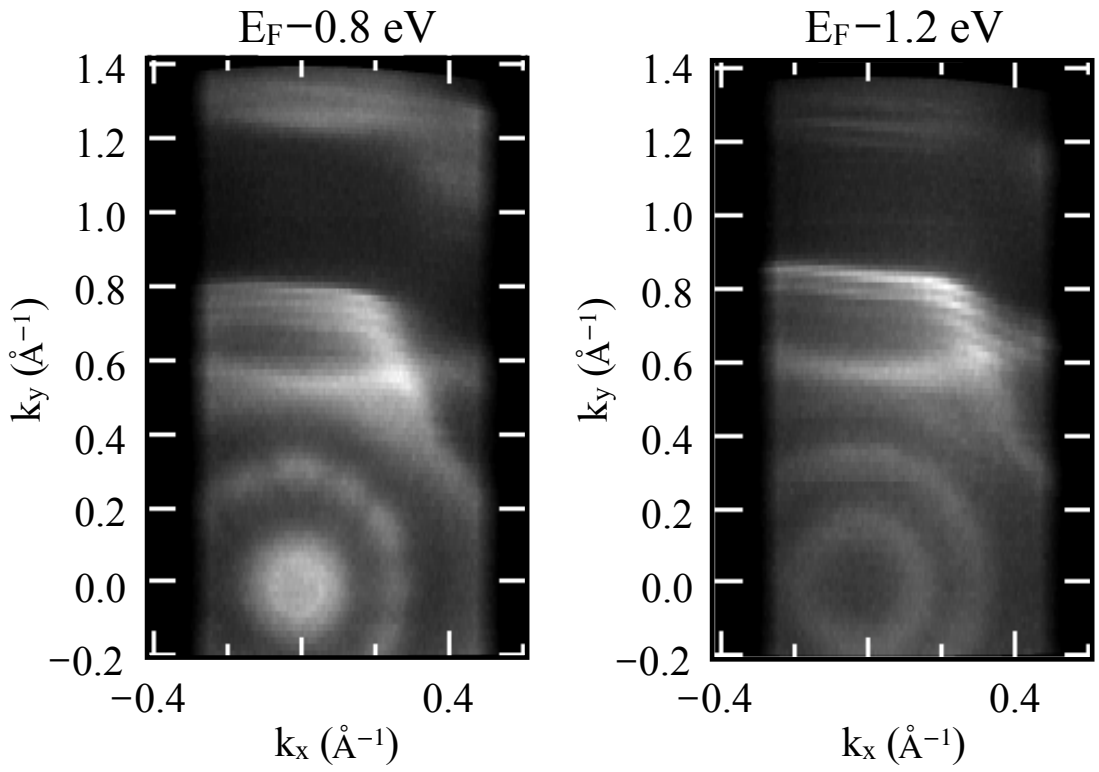

Figure 5.11: The ARPES constant-energy contours of 10-layer Pb(111)/9-layer Ag(111) grown on Si(111) at $E_F-0.8$ and $E_F-1.2$ eV, respectively.

In summary, we verified that rotation barely affected the energies of the states around the $\bar{\Gamma}$ point. Moreover, the presence of the substrate changes the boundary conditions at the interface and can modify the QWS around the $\bar{\Gamma}$ point. Along with the SC model with reasonable size and strain levels, we performed the band unfolding calculations and results were in agreement with the reported ARPES data [111]. Moreover, the electronic distribution along the direction perpendicular to the thin film is modulated by QWSs and the electronic coherence can be achieved through connecting QWSs in each metallic part with its own commensurate wavelength. Our findings can guide future theoretical work, in which a complete understanding of the experimental observation in multiple stacked thin films is crucial so as to achieve more complicated designs.

CHAPTER 6
CONCLUSIONS

We have investigated the properties of three classes of heterostructures formed by 2D materials grown on metal substrates, including Si thin films on a Ag substrate (Chapter 3), *h*-BN on Ru(0001) and Cu(111) substrates (Chapter 4), and a stacked combination of Pb and Ag thin films (Chapter 5). The main results are summarized below.

Our calculated results suggest that the $\sqrt{3} \times \sqrt{3}$ phase of Si grown on Ag(111) experimentally observed by STM is in fact a Si thin film with the honeycomb chain trimer (HCT) model of Ag adatoms on the surface. The presence of Ag on the surface in the $\sqrt{3} \times \sqrt{3}$ phase may be caused by floating Ag adatoms originated from the Ag substrate. From the HCT model, we show that a part of its parabolic surface band, shown in Figure 3.4(a), has a similar slope to that of the dispersion experimentally derived from the tunneling spectra. We also show that the calculated STM images for the HCT model yield similar patterns to that observed by the experiment. On the other hand, we have presented the structures of 1.5 ML and 2.5 ML of Si thin films on Ag(111) with the HCT model on the surface, as illustrated in Figures 3.1(b) and 3.1(c), respectively. The calculated results show that the features of the HCT model may emerge when the thickness of Si thin films is equal or above 2.5 ML. Based on these studies, we conclude that 2D silicene and its unique linear dispersion do not exist on the Ag(111) substrate. Instead, we suggest that the observed $\sqrt{3} \times \sqrt{3}$ phase is not silicene but a Si thin film with the presence of Ag on the surface.

Our calculations conclude that the *h*-BN monolayer can interact with the underlying Ru and Cu substrates through the hybridization between the p orbitals of N and d orbitals of metal substrates, which takes place in the regions where N is located on top of a metal atom. In *h*-BN/Ru(0001), the hybridization induces distinct states in the middle of the *h*-BN band gap (Figure 4.4), while in *h*-BN/Cu(111), the hybridization induces states just above the top

of the valence band, causing a narrowing of the band gap (Figure 4.9). The hybridization can also modulate the separation of the *h*-BN layer to the substrate. As a consequence, the regions in *h*-BN with N on top of a metal atom move closer to the substrate, leading to a corrugated *h*-BN layer. Moreover, the spatially-periodic corrugation of the *h*-BN layer can give rise to a modulation of the local work function with the calculated values in good agreement with experimental results.

For the composite Pb and Ag metal films, our results of the band unfolding illustrate that, while rotation between Pb and Ag lattices has no effects on the energies of the quantum well states at the $\bar{\Gamma}$ point, the presence of a Si substrate can shift the energies of those states because the interface condition has been modified, and thus the phase shifts of the quantum well states can be altered. Our calculated unfolded band structure with the Si substrate is consistent with the ARPES data, as presented in Figure 5.8.

To summarize, our supercell model approach has been successfully applied to the heterostructures formed by 2D materials grown on metallic substrates. Because the small strain level in our supercell model, the resulting electronic properties, including the local density of states, the band structure, the constant-energy contours, and the local work function, agree well with experimental observations. All the findings above suggest that the interaction between the 2D materials and the substrates plays an important role in determining their electronic properties.

REFERENCES

[1] P. Hohenberg and W. Kohn, "Inhomogeneous electron gas," *Phys. Rev.*, vol. 136, B864–B871, 3B 1964.

[2] W. Kohn and L. J. Sham, "Self-consistent equations including exchange and correlation effects," *Phys. Rev.*, vol. 140, A1133–A1138, 4A 1965.

[3] L. H. Thomas, "The calculation of atomic fields," *Mathematical Proceedings of the Cambridge Philosophical Society*, vol. 23, no. 5, 542–548, 1927.

[4] E. Fermi, "Eine statistische methode zur bestimmung einiger eigenschaften des atoms und ihre anwendung auf die theorie des periodischen systems der elemente," *Zeitschrift für Physik*, vol. 48, no. 1, pp. 73–79, 1928.

[5] D. C. Langreth and M. J. Mehl, "Beyond the local-density approximation in calculations of ground-state electronic properties," *Phys. Rev. B*, vol. 28, pp. 1809–1834, 4 1983.

[6] A. D. Becke, "Density-functional exchange-energy approximation with correct asymptotic behavior," *Phys. Rev. A*, vol. 38, pp. 3098–3100, 6 1988.

[7] J. P. Perdew, J. A. Chevary, S. H. Vosko, K. A. Jackson, M. R. Pederson, D. J. Singh, and C. Fiolhais, "Atoms, molecules, solids, and surfaces: Applications of the generalized gradient approximation for exchange and correlation," *Phys. Rev. B*, vol. 46, pp. 6671–6687, 11 1992.

[8] D. R. Hamann, M. Schlüter, and C. Chiang, "Norm-conserving pseudopotentials," *Phys. Rev. Lett.*, vol. 43, pp. 1494–1497, 20 1979.

[9] P. E. Blöchl, "Projector augmented-wave method," *Phys. Rev. B*, vol. 50, pp. 17 953–17 979, 24 1994.

[10] G. Kresse and D. Joubert, "From ultrasoft pseudopotentials to the projector augmented-wave method," *Phys. Rev. B*, vol. 59, pp. 1758–1775, 3 1999.

[11] N. A. W. Holzwarth, G. E. Matthews, R. B. Dunning, A. R. Tackett, and Y. Zeng, "Comparison of the projector augmented-wave, pseudopotential, and linearized augmented-plane-wave formalisms for density-functional calculations of solids," *Phys. Rev. B*, vol. 55, pp. 2005–2017, 4 1997.

[12] D. M. Ceperley and B. J. Alder, "Ground state of the electron gas by a stochastic method," *Phys. Rev. Lett.*, vol. 45, pp. 566–569, 7 1980.

[13] J. P. Perdew and A. Zunger, "Self-interaction correction to density-functional approximations for many-electron systems," *Phys. Rev. B*, vol. 23, pp. 5048–5079, 10 1981.

[14] S. H. Vosko, L. Wilk, and M. Nusair, "Accurate spin-dependent electron liquid correlation energies for local spin density calculations: A critical analysis," *Canadian Journal of Physics*, vol. 58, no. 8, pp. 1200–1211, 1980.

[15] J. P. Perdew, K. Burke, and M. Ernzerhof, "Generalized gradient approximation made simple," *Phys. Rev. Lett.*, vol. 77, pp. 3865–3868, 18 1996.

[16] G. Binnig, H. Rohrer, C. Gerber, and E. Weibel, "Tunneling through a controllable vacuum gap," *Applied Physics Letters*, vol. 40, no. 2, pp. 178–180, 1982.

[17] ——, "Surface studies by scanning tunneling microscopy," *Phys. Rev. Lett.*, vol. 49, pp. 57–61, 1 1982.

[18] J. Bardeen, "Tunnelling from a many-particle point of view," *Phys. Rev. Lett.*, vol. 6, pp. 57–59, 2 1961.

[19] J. Tersoff and D. R. Hamann, "Theory and application for the scanning tunneling microscope," *Phys. Rev. Lett.*, vol. 50, pp. 1998–2001, 25 1983.

[20] ——, "Theory of the scanning tunneling microscope," *Phys. Rev. B*, vol. 31, pp. 805–813, 2 1985.

[21] V. Popescu and A. Zunger, "Extracting $\mathbf{E}$ versus $\mathbf{k}$ effective band structure from supercell calculations on alloys and impurities," *Phys. Rev. B*, vol. 85, p. 085 201, 8 2012.

[22] A. Tkatchenko and M. Scheffler, "Accurate Molecular Van Der Waals Interactions from Ground-state Electron Density and Free-Atom Reference Data," *Phys. Rev. Lett.*, vol. 102, p. 073 005, 7 2009.

[23] A. D. Becke and E. R. Johnson, "Exchange-hole dipole moment and the dispersion interaction revisited," *The Journal of Chemical Physics*, vol. 127, no. 15, p. 154 108, 2007.

[24] M. Dion, H. Rydberg, E. Schröder, D. C. Langreth, and B. I. Lundqvist, "Van der Waals density functional for general geometries," *Phys. Rev. Lett.*, vol. 92, no. 24, p. 246 401, 2004.

[25] J. Klime, D. R. Bowler, and A. Michaelides, "Chemical accuracy for the van der waals density functional," *Journal of Physics: Condensed Matter*, vol. 22, no. 2, p. 022 201, 2010.

[26] G. Román-Pérez and J. M. Soler, "Efficient implementation of a van der Waals density functional: Application to double-wall carbon nanotubes," *Phys. Rev. Lett.*, vol. 103, no. 9, p. 096 102, 2009.

[27] K. S. Novoselov, A. K. Geim, S. V. Morozov, D. Jiang, Y. Zhang, S. V. Dubonos, I. V. Grigorieva, and A. A. Firsov, "Electric Field Effect in Atomically Thin Carbon Films," *Science*, vol. 306, no. 5696, pp. 666–669, 2004.

[28] K. Takeda and K. Shiraishi, "Theoretical possibility of stage corrugation in si and ge analogs of graphite," *Phys. Rev. B*, vol. 50, pp. 14 916–14 922, 20 1994.

[29] S. Cahangirov, M. Topsakal, E. Aktürk, H. Şahin, and S. Ciraci, "Two- and One-Dimensional Honeycomb Structures of Silicon and Germanium," *Phys. Rev. Lett.*, vol. 102, p. 236 804, 23 2009.

[30] G. G. Guzmán-Verri and L. C. Lew Yan Voon, "Electronic structure of silicon-based nanostructures," *Phys. Rev. B*, vol. 76, p. 075 131, 7 2007.

[31] C. L. Kane and E. J. Mele, "Quantum Spin Hall Effect in Graphene," *Phys. Rev. Lett.*, vol. 95, p. 226 801, 22 2005.

[32] C.-C. Liu, W. Feng, and Y. Yao, "Quantum spin hall effect in silicene and two-dimensional germanium," *Phys. Rev. Lett.*, vol. 107, p. 076 802, 7 2011.

[33] P. Vogt, P. De Padova, C. Quaresima, J. Avila, E. Frantzeskakis, M. C. Asensio, A. Resta, B. Ealet, and G. Le Lay, "Silicene: Compelling experimental evidence for graphenelike two-dimensional silicon," *Phys. Rev. Lett.*, vol. 108, p. 155 501, 15 2012.

[34] B. Lalmi, H. Oughaddou, H. Enriquez, A. Kara, S. Vizzini, B. Ealet, and B. Aufray, "Epitaxial growth of a silicene sheet," *Applied Physics Letters*, vol. 97, no. 22, p. 223 109, 2010.

[35] B. Feng, Z. Ding, S. Meng, Y. Yao, X. He, P. Cheng, L. Chen, and K. Wu, "Evidence of Silicene in Honeycomb Structures of Silicon on Ag(111)," *Nano Letters*, vol. 12, no. 7, pp. 3507–3511, 2012.

[36] A. Fleurence, R. Friedlein, T. Ozaki, H. Kawai, Y. Wang, and Y. Yamada-Takamura, "Experimental Evidence for Epitaxial Silicene on Diboride Thin Films," *Phys. Rev. Lett.*, vol. 108, p. 245 501, 24 2012.

[37] L. Meng, Y. Wang, L. Zhang, S. Du, R. Wu, L. Li, Y. Zhang, G. Li, H. Zhou, W. A. Hofer, and H.-J. Gao, "Buckled Silicene formation on Ir(111)," *Nano Letters*, vol. 13, no. 2, pp. 685–690, 2013.

[38] H Jamgotchian, Y Colignon, N Hamzaoui, B Ealet, J. Y. Hoarau, B Aufray, and J. P. Bibrian, "Growth of silicene layers on Ag(111): Unexpected effect of the substrate temperature," *Journal of Physics: Condensed Matter*, vol. 24, no. 17, p. 172 001, 2012.

[39] H. Enriquez, S. Vizzini, A. Kara, B. Lalmi, and H. Oughaddou, "Silicene structures on silver surfaces," *Journal of Physics: Condensed Matter*, vol. 24, no. 31, p. 314 211, 2012.

[40] R. Arafune, C.-L. Lin, K. Kawahara, N. Tsukahara, E. Minamitani, Y. Kim, N. Takagi, and M. Kawai, "Structural transition of silicene on Ag(111)," *Surface Science*, vol. 608, pp. 297 –300, 2013.

[41] C.-L. Lin, R. Arafune, K. Kawahara, M. Kanno, N. Tsukahara, E. Minamitani, Y. Kim, M. Kawai, and N. Takagi, "Substrate-induced symmetry breaking in silicene," *Phys. Rev. Lett.*, vol. 110, p. 076 801, 7 2013.

[42] S. K. Mahatha, P. Moras, V. Bellini, P. M. Sheverdyaeva, C. Struzzi, L. Petaccia, and C. Carbone, "Silicene on Ag(111): A honeycomb lattice without Dirac bands," *Phys. Rev. B*, vol. 89, no. 20, p. 201 416, 2014.

[43] P. Vogt, P. Capiod, M. Berthe, A. Resta, P. D. Padova, T. Bruhn, G. L. Lay, and B. Grandidier, "Synthesis and electrical conductivity of multilayer silicene," *Applied Physics Letters*, vol. 104, no. 2, p. 021 602, 2014.

[44] E Salomon, R. E. Ajjouri, G. L. Lay, and T Angot, "Growth and structural properties of silicene at multilayer coverage," *Journal of Physics: Condensed Matter*, vol. 26, no. 18, p. 185 003, 2014.

[45] P Moras, T. O. Mentes, P. M. Sheverdyaeva, A Locatelli, and C Carbone, "Coexistence of multiple silicene phases in silicon grown on ag(111)," *Journal of Physics: Condensed Matter*, vol. 26, no. 18, p. 185 001, 2014.

[46] B. Feng, Z. Ding, S. Meng, Y. Yao, X. He, P. Cheng, L. Chen, and K. Wu, "Evidence of silicene in honeycomb structures of silicon on ag(111)," *Nano Letters*, vol. 12, no. 7, pp. 3507–3511, 2012.

[47] L. Chen, H. Li, B. Feng, Z. Ding, J. Qiu, P. Cheng, K. Wu, and S. Meng, "Spontaneous Symmetry Breaking and Dynamic Phase Transition in Monolayer Silicene," *Phys. Rev. Lett.*, vol. 110, no. 8, p. 085 504, 2013.

[48] L. Chen, C.-C. Liu, B. Feng, X. He, P. Cheng, Z. Ding, S. Meng, Y. Yao, and K. Wu, "Evidence for Dirac Fermions in a Honeycomb Lattice Based on Silicon," *Phys. Rev. Lett.*, vol. 109, no. 5, 2012.

[49] R. Arafune, C.-L. Lin, R. Nagao, M. Kawai, and N. Takagi, "Comment on Evidence for Dirac Fermions in a Honeycomb Lattice Based on Siliconi," *Phys. Rev. Lett.*, vol. 110, no. 22, 2013.

[50] A. J. Mannix, B. Kiraly, B. L. Fisher, M. C. Hersam, and N. P. Guisinger, "Silicon Growth at the Two-Dimensional Limit on Ag(111)," *ACS Nano*, vol. 8, no. 7, pp. 7538–7547, 2014.

[51] Y. G. Ding, C. T. Chan, and K. M. Ho, "Structure of the $(\sqrt{3} \times \sqrt{3})$R30° Ag/Si(111) surface from first-principles calculations," *Phys. Rev. Lett.*, vol. 67, no. 11, p. 1454, 1991.

[52] E. J. van Loenen, J. E. Demuth, R. M. Tromp, and R. J. Hamers, "Local electron states and surface geometry of Si(111)-$(\sqrt{3} \times \sqrt{3})$Ag," *Phys. Rev. Lett.*, vol. 58, pp. 373–376, 4 1987.

[53] R. J. Wilson and S. Chiang, "Registration and nucleation of the Ag/Si(111)$(\sqrt{3} \times \sqrt{3})$R30° structure by scanning tunneling microscopy," *Phys. Rev. Lett.*, vol. 59, pp. 2329–2332, 20 1987.

[54] T. Takahashi, S. Nakatani, N. Okamoto, T. Ishikawa, and S. Kikuta, "Studies on Si(111) 7/8×7/8 -Bi and -Ag surfaces by x-ray diffraction under nearly normal incidence," *Review of Scientific Instruments*, vol. 60, no. 7, pp. 2365–2368, 1989.

[55] L. S. O. Johansson, E. Landemark, C. J. Karlsson, and R. I. G. Uhrberg, "Fermi-level pinning and surface-state band structure of the si(111)-$\sqrt{3} \times \sqrt{3}$R30°-Ag surface," *Phys. Rev. Lett.*, vol. 63, pp. 2092–2095, 19 1989.

[56] M. Katayama, R. S. Williams, M. Kato, E. Nomura, and M. Aono, "Structure analysis of the Si(111)$\sqrt{3} \times \sqrt{3}$R30°-Ag surface," *Phys. Rev. Lett.*, vol. 66, pp. 2762–2765, 21 1991.

[57] Y. G. Ding, C. T. Chan, and K. M. Ho, "Structure of the $(\sqrt{3} \times \sqrt{3})$R30° Ag/Si(111) surface from first-principles calculations," *Phys. Rev. Lett.*, vol. 67, pp. 1454–1457, 11 1991.

[58] S. Hasegawa, "Surface-state bands on silicon as electron systems in reduced dimensions at atomic scales," *Journal of Physics: Condensed Matter*, vol. 12, no. 35, R463, 2000.

[59] J. Feng, S. R. Wagner, and P. Zhang, "Interfacial coupling and electronic structure of two-dimensional silicon grown on the Ag(111) surface at high temperature," *Scientific reports*, vol. 5, p. 10 310, 2015.

[60] S. Cahangirov, V. O. Öz çelik, L. Xian, J. Avila, S. Cho, M. C. Asensio, S. Ciraci, and A. Rubio, "Atomic structure of the $\sqrt{3} \times \sqrt{3}$ phase of silicene on Ag(111)," *Phys. Rev. B*, vol. 90, p. 035 448, 3 2014.

[61] B. Peng, H. Zhang, H. Shao, Y. Xu, R. Zhang, H. Lu, D. W. Zhang, and H. Zhu, "First-principles prediction of ultralow lattice thermal conductivity of dumbbell silicene: A comparison with low-buckled silicene," *ACS Applied Materials & Interfaces*, vol. 8, no. 32, pp. 20 977–20 985, 2016.

[62] G. Kresse and J. Furthmller, "Efficiency of ab-initio total energy calculations for metals and semiconductors using a plane-wave basis set," *Computational Materials Science*, vol. 6, no. 1, pp. 15 –50, 1996.

[63] G. Kresse and J. Furthmüller, "Efficient iterative schemes for *ab initio* total-energy calculations using a plane-wave basis set," *Phys. Rev. B*, vol. 54, pp. 11 169–11 186, 16 1996.

[64] A. K. Geim and I. V. Grigorieva, "Van der Waals heterostructures," *Nature*, vol. 499, no. 7459, p. 419, 2013.

[65] Y. Gong, J. Lin, X. Wang, G. Shi, S. Lei, Z. Lin, X. Zou, G. Ye, R. Vajtai, B. I. Yakobson, *et al.*, "Vertical and in-plane heterostructures from WS_2/MoS_2 monolayers," *Nature materials*, vol. 13, no. 12, p. 1135, 2014.

[66] C.-H. Lee, G.-H. Lee, A. M. Van Der Zande, W. Chen, Y. Li, M. Han, X. Cui, G. Arefe, C. Nuckolls, T. F. Heinz, *et al.*, "Atomically thin p–n junctions with van der waals heterointerfaces," *Nature nanotechnology*, vol. 9, no. 9, p. 676, 2014.

[67] K. S. Novoselov, A. Mishchenko, A. Carvalho, and A. H. Castro Neto, "2D materials and van der waals heterostructures," *Science*, vol. 353, no. 6298, 2016.

[68] J. Xue, J. Sanchez-Yamagishi, D. Bulmash, P. Jacquod, A. Deshpande, K Watanabe, T Taniguchi, P. Jarillo-Herrero, and B. J. LeRoy, "Scanning tunnelling microscopy and spectroscopy of ultra-flat graphene on hexagonal boron nitride," *Nature materials*, vol. 10, no. 4, p. 282, 2011.

[69] R. Bistritzer and A. H. MacDonald, "Moiré butterflies in twisted bilayer graphene," *Phys. Rev. B*, vol. 84, p. 035 440, 3 2011.

[70] M. Yankowitz, J. Xue, D. Cormode, J. D. Sanchez-Yamagishi, K Watanabe, T Taniguchi, P. Jarillo-Herrero, P. Jacquod, and B. J. LeRoy, "Emergence of super-

lattice dirac points in graphene on hexagonal boron nitride," *Nature Physics*, vol. 8, no. 5, p. 382, 2012.

[71] Z. F. Wang, F. Liu, and M. Y. Chou, "Fractal landau-level spectra in twisted bilayer graphene," *Nano Letters*, vol. 12, no. 7, pp. 3833–3838, 2012.

[72] L. Ponomarenko, R. Gorbachev, G. Yu, D. Elias, R Jalil, A. Patel, A Mishchenko, A. Mayorov, C. Woods, J. Wallbank, *et al.*, "Cloning of Dirac fermions in graphene superlattices," *Nature*, vol. 497, no. 7451, p. 594, 2013.

[73] P. Moon and M. Koshino, "Electronic properties of graphene/hexagonal-boron-nitride moiré superlattice," *Phys. Rev. B*, vol. 90, p. 155 406, 15 2014.

[74] A. Rubio, J. L. Corkill, and M. L. Cohen, "Theory of graphitic boron nitride nanotubes," *Phys. Rev. B*, vol. 49, pp. 5081–5084, 7 1994.

[75] X Blase, A Rubio, S. G Louie, and M. L Cohen, "Stability and band gap constancy of boron nitride nanotubes," *Europhysics Letters (EPL)*, vol. 28, no. 5, pp. 335–340, 1994.

[76] W. Auwrter, T. Kreutz, T. Greber, and J. Osterwalder, "XPD and STM investigation of hexagonal boron nitride on Ni(111)," *Surface Science*, vol. 429, no. 1, pp. 229 –236, 1999.

[77] W. Auwrter, H. U. Suter, H. Sachdev, and T. Greber, "Synthesis of One Monolayer of Hexagonal Boron Nitride on Ni(111) from B-Trichloroborazine (ClBNH)3," *Chemistry of Materials*, vol. 16, no. 2, pp. 343–345, 2004.

[78] A. Preobrajenski, A. Vinogradov, and N. Mrtensson, "Monolayer of h-BN chemisorbed on Cu(111) and Ni(111): The role of the transition metal 3d states," Surface Science, vol. 582, no. 1-3, pp. 21–30, 2005.

[79] F. Müller, S. Hüfner, H. Sachdev, R. Laskowski, P. Blaha, and K. Schwarz, "Epitaxial growth of hexagonal boron nitride on Ag(111)," *Phys. Rev. B*, vol. 82, p. 113 406, 11 2010.

[80] Y. Zhang, M. Wei, Q. Fu, and X. Bao, "Oxygen intercalation under hexagonal boron nitride (h-bn) on pt(111)," *Science Bulletin*, vol. 60, no. 18, pp. 1572 –1579, 2015.

[81] C. R. Dean, A. F. Young, I. Meric, C. Lee, L. Wang, S. Sorgenfrei, K. Watanabe, T. Taniguchi, P. Kim, K. L. Shepard, *et al.*, "Boron nitride substrates for high-quality graphene electronics," *Nature nanotechnology*, vol. 5, no. 10, p. 722, 2010.

[82] M. Corso, W. Auwärter, M. Muntwiler, A. Tamai, T. Greber, and J. Osterwalder, "Boron Nitride Nanomesh," *Science*, vol. 303, no. 5655, pp. 217–220, 2004.

[83] A. Goriachko, Y. He, M. Knapp, H. Over, M. Corso, T. Brugger, S. Berner, J. Osterwalder, and T. Greber, "Self-assembly of a hexagonal boron nitride nanomesh on Ru(0001)," *Langmuir*, vol. 23, no. 6, pp. 2928–2931, 2007.

[84] T. Brugger, S. Günther, B. Wang, J. H. Dil, M.-L. Bocquet, J. Osterwalder, J. Wintterlin, and T. Greber, "Comparison of electronic structure and template function of single-layer graphene and a hexagonal boron nitride nanomesh on Ru(0001)," *Phys. Rev. B*, vol. 79, p. 045 407, 4 2009.

[85] Q. Zhang, Y. Chen, C. Zhang, C.-R. Pan, M.-Y. Chou, C. Zeng, and C.-K. Shih, "Bandgap renormalization and work function tuning in $MoSe_2$/hBN/Ru(0001) heterostructures," *Nature communications*, vol. 7, p. 13 843, 2016.

[86] R. Laskowski and P. Blaha, "Ab initio study of h-BN nanomeshes on Ru(001), Rh(111), and Pt(111)," *Phys. Rev. B*, vol. 81, p. 075 418, 7 2010.

[87] M. E. Straumanis and L. S. Yu, "Lattice parameters, densities, expansion coefficients and perfection of structure of Cu and of Cu–In α phase," *Acta Crystallographica Section A*, vol. 25, no. 6, pp. 676–682, 1969.

[88] R. W. Lynch and H. G. Drickamer, "Effect of high pressure on the lattice parameters of diamond, graphite, and hexagonal boron nitride," *The Journal of Chemical Physics*, vol. 44, no. 1, pp. 181–184, 1966.

[89] S. Joshi, D. Ecija, R. Koitz, M. Iannuzzi, A. P. Seitsonen, J. Hutter, H. Sachdev, S. Vijayaraghavan, F. Bischoff, K. Seufert, *et al.*, "Boron nitride on Cu(111): An electronically corrugated monolayer," *Nano letters*, vol. 12, no. 11, pp. 5821–5828, 2012.

[90] K. K. Kim, A. Hsu, X. Jia, S. M. Kim, Y. Shi, M. Hofmann, D. Nezich, J. F. Rodriguez-Nieva, M. Dresselhaus, T. Palacios, and J. Kong, "Synthesis of Monolayer Hexagonal Boron Nitride on Cu Foil Using Chemical Vapor Deposition," *Nano Letters*, vol. 12, no. 1, pp. 161–166, 2012.

[91] Q. Li, X. Zou, M. Liu, J. Sun, Y. Gao, Y. Qi, X. Zhou, B. I. Yakobson, Y. Zhang, and Z. Liu, "Grain boundary structures and electronic properties of hexagonal boron nitride on Cu(111)," *Nano Letters*, vol. 15, no. 9, pp. 5804–5810, 2015.

[92] M. Schwarz, A. Riss, M. Garnica, J. Ducke, P. S. Deimel, D. A. Duncan, P. K. Thakur, T.-L. Lee, A. P. Seitsonen, J. V. Barth, *et al.*, "Corrugation in the weakly interacting hexagonal-BN/Cu(111) system: Structure determination by combining noncontact atomic force microscopy and x-ray standing waves," *ACS nano*, vol. 11, no. 9, pp. 9151–9161, 2017.

[93] Q. Zhang, J. Yu, P. Ebert, C. Zhang, C.-R. Pan, M.-Y. Chou, C.-K. Shih, C. Zeng, and S. Yuan, "Tuning Band Gap and Work Function Modulations in Monolayer hBN/Cu(111) Heterostructures with Moiré Patterns," *ACS Nano*, vol. 12, no. 9, pp. 9355–9362, 2018.

[94] R. Koitz, A. P. Seitsonen, M. Iannuzzi, and J. Hutter, "Structural and electronic properties of a large-scale moiré pattern of hexagonal boron nitride on Cu(111) studied with density functional theory," *Nanoscale*, vol. 5, pp. 5589–5595, 12 2013.

[95] C. Brlke, T. Heepenstrick, N. Humberg, I. Krieger, M. Sokolowski, S. Wei, F. S. Tautz, and S. Soubatch, "Long Vertical Distance Bonding of the Hexagonal Boron Nitride Monolayer on the Cu(111) Surface," *The Journal of Physical Chemistry C*, vol. 121, no. 43, pp. 23 964–23 973, 2017.

[96] H. J. Monkhorst and J. D. Pack, "Special points for brillouin-zone integrations," *Phys. Rev. B*, vol. 13, pp. 5188–5192, 12 1976.

[97] R. Laskowski, P. Blaha, and K. Schwarz, "Bonding of hexagonal BN to transition metal surfaces: An ab initio density-functional theory study," *Phys. Rev. B*, vol. 78, p. 045 409, 4 2008.

[98] F. Schulte, "A theory of thin metal films: Electron density, potentials and work function," *Surface Science*, vol. 55, no. 2, pp. 427 –444, 1976.

[99] M. Hupalo and M. C. Tringides, "Correlation between height selection and electronic structure of the uniform height Pb/Si(111) islands," *Phys. Rev. B*, vol. 65, p. 115 406, 11 2002.

[100] R. Otero, A. L. Vázquez de Parga, and R. Miranda, "Observation of preferred heights in Pb nanoislands: A quantum size effect," *Phys. Rev. B*, vol. 66, p. 115 401, 11 2002.

[101] H. Hong, C.-M. Wei, M. Y. Chou, Z. Wu, L. Basile, H. Chen, M. Holt, and T.-C. Chiang, "Alternating Layer and Island Growth of Pb on Si by Spontaneous Quantum Phase Separation," *Phys. Rev. Lett.*, vol. 90, p. 076 104, 7 2003.

[102] M. H. Upton, C. M. Wei, M. Y. Chou, T. Miller, and T.-C. Chiang, "Thermal Stability and Electronic Structure of Atomically Uniform Pb Films on Si(111)," *Phys. Rev. Lett.*, vol. 93, p. 026 802, 2 2004.

[103] Y.-F. Zhang, J.-F. Jia, T.-Z. Han, Z. Tang, Q.-T. Shen, Y. Guo, Z. Q. Qiu, and Q.-K. Xue, "Band Structure and Oscillatory Electron-Phonon Coupling of Pb Thin Films Determined by Atomic-Layer-Resolved Quantum-Well States," *Phys. Rev. Lett.*, vol. 95, p. 096 802, 9 2005.

[104] M. M. Özer, Y. Jia, B. Wu, Z. Zhang, and H. H. Weitering, "Quantum stability and reentrant bilayer-by-bilayer growth of atomically smooth Pb films on semiconductor substrates," *Phys. Rev. B*, vol. 72, p. 113 409, 11 2005.

[105] Y. Guo, Y.-F. Zhang, X.-Y. Bao, T.-Z. Han, Z. Tang, L.-X. Zhang, W.-G. Zhu, E. G. Wang, Q. Niu, Z. Q. Qiu, J.-F. Jia, Z.-X. Zhao, and Q.-K. Xue, "Superconductivity Modulated by Quantum Size Effects," *Science*, vol. 306, no. 5703, pp. 1915–1917, 2004.

[106] D. Eom, S. Qin, M.-Y. Chou, and C. K. Shih, "Persistent Superconductivity in Ultrathin Pb Films: A Scanning Tunneling Spectroscopy Study," *Phys. Rev. Lett.*, vol. 96, p. 027 005, 2 2006.

[107] S. Qin, J. Kim, Q. Niu, and C.-K. Shih, "Superconductivity at the Two-dimensional Limit," *Science*, vol. 324, no. 5932, pp. 1314–1317, 2009.

[108] J. J. Paggel, C. M. Wei, M. Y. Chou, D.-A. Luh, T. Miller, and T.-C. Chiang, "Atomic-layer-resolved quantum oscillations in the work function: Theory and experiment for Ag/Fe(100)," *Phys. Rev. B*, vol. 66, p. 233 403, 23 2002.

[109] C. M. Wei and M. Y. Chou, "Effects of the substrate on quantum well states: A first-principles study for Ag/Fe(100)," *Phys. Rev. B*, vol. 68, p. 125 406, 12 2003.

[110] J. Kim, S. Qin, W. Yao, Q. Niu, M. Y. Chou, and C.-K. Shih, "Quantum size effects on the work function of metallic thin film nanostructures," *Proceedings of the National Academy of Sciences*, vol. 107, no. 29, pp. 12 761–12 765, 2010.

[111] M. K. Brinkley, Y. Liu, N. J. Speer, T. Miller, and T.-C. Chiang, "Using Electronic Coherence to Probe a Deeply Embedded Quantum Well in Bimetallic Pb/Ag Films on Si(111)," *Phys. Rev. Lett.*, vol. 103, p. 246 801, 24 2009.

[112] P. V. C. Medeiros, S. Stafström, and J. Björk, "Effects of extrinsic and intrinsic perturbations on the electronic structure of graphene: Retaining an effective primitive cell band structure by band unfolding," *Phys. Rev. B*, vol. 89, p. 041 407, 4 2014.

[113] P. V. C. Medeiros, S. S. Tsirkin, S. Stafström, and J. Björk, "Unfolding spinor wave functions and expectation values of general operators: Introducing the unfolding-density operator," *Phys. Rev. B*, vol. 91, p. 041 116, 4 2015.

VITA

Chi-Ruei Pan enrolled in National Taiwan University in the fall of 2010 and graduated in the summer of 2012 with a master degree in Physics with Computaional Physics. He joined Georgia Tech as a PhD student in the spring of 2014. During his PhD studies, he made four separate research visits to the Institute of Atomic and Molecular Sciences of Academia Sinica in Taiwan, spending a total of eight semesters living and working there. In March 2019, he successfully defended his PhD thesis. After graduating from Georgia Tech, he will be moving on to work at the Taiwan Semiconductor Manufacturing Company (TSMC) in Hsinchu, Taiwan.